University of Venda
Creating Future Leaders

University of Venda

Low Field Microwave Absorption in Nano-Magnetic Particle-incorporated $YBa_2Cu_3O_{7-x}$ Superconducting Materials

by

Fhulufhelo Nemangwele

(11502258)

A thesis submitted to fulfill the requirements for the Degree of Doctor of Philosophy in

PHYSICS

at the

School of Mathematical and Natural Sciences

University of Venda

Thohoyandou, Limpopo

South Africa

Promoter : Prof. Vijaya Srinivasu Vallabhapurapu (UNISA)

Co-Promoter : Dr. Nnditshedzeni Eric Maluta (UNIVEN)

Co-Promoter : Dr. Joseph Kiprono Kirui (UNIVEN)

February 2018

DECLARATION

I, Fhulufhelo Nemangwele, declare that this research thesis is my original work and has not been submitted for any degree at any other university or institution. The research thesis does not contain other persons' writing unless specifically acknowledged and referenced accordingly.

Signed (Student):.. Date:..

ACKNOWLEDGMENT

Every author is always indebted to his colleagues, and so it is a standard custom in the scientific literature to say thanks for many helpful discussions. That is not enough here, the long hours put in by many friends and professional colleagues (heavily, but certainly not exclusively) at University of South Africa are deserving of much greater recognition.

I would like to thank Prof V.V. Srinivasu for teaching me everything I know about experimental physics, for introducing me to the fascinating science of superconducting devices and for guiding me through my graduate studies. Prof V.V Srinivasu is an outstanding scientist, mentor, and a wonderful person. I continued to rely very heavily on the patience and generosity of my promoters Prof V.V. Srinivasu and the late Prof V. Sankaran.

At the outset I certainly did not know all the various required disciplines. I had to be tutored in the subject and for that, I would like to thank Prof Dillip and Dr Jayashree. After that, my written drafts had to be reviewed, corrected, and critiqued both for factual accuracy and for clarity of presentation.

A lot of very fine people especially from STEM group (Unisa) took time away from their own pursuits in order to help me succeed. A case in point is Mr Mahule who assisted me overnight when running EPR. Foremost among them Dr B.K. Roul is a STEM group collaborator at Bhubaneswar, Institute of Material Science, India for inviting and allowing me to use the IMS Laboratory to prepare my Ni-YBCO samples.

Many other Univen scientists contributed to my education in the HTSC field, and several reviewed individual chapters, which resulted in the elimination of a number of errors and mistaken concepts. In this regard I am particularly grateful to Dr J.K. Kirui and Dr N.E. Maluta.

My thanks are also extended to members of my family, my wife Aluwani and my son, Thendo and my two daughters, Shudufhadzani and Murendwa for their immeasurable support and encouragement.

Publications as First Author

CHAPTER FIVE

Non-resonant Microwave Absorption in Nano-nickel Added YBCO Powders: Observation of Multiple Phase Reversals. F. Nemangwele, V. Sankaran, B.K. Roal, J.Das, and V.V. Srinivasu, *J. Supercond. Nov Magn*, Vol 29, 11, 1557-1939 (2016).

Submitted and First Author

CHAPTER SIX

Non-resonant Microwave Absorption Signals in Nano Nickel-added YBCO Superconducting Powders: Distinctive observation. F. Nemangwele, B.K. Roul and V.V. Srinivasu, Submitted to *IEEE*, EUCAS17-3EP1-23.

CHAPTER SEVEN

Non-resonant microwave absorption in nano Nickel-added YBCO superconductor: Low Field Hysteresis. F. Nemangwele , T S Mahule and V.V. Srinivasu, submitted to *J. Supercond. Nov Magn*,ICSM 6-3590.

Dedicated to my family who have made many things possible.

DEFINITION OF TERMS

In order to clarify principles of superconductivity, a summary of the properties of superconductors and a glossary of terms used in this work is provided below:

HTSC: High temperature superconductor.

Critical current density (J_c): the maximum current a superconducting material can carry without any resistance.

First critical field (Hc_1): the field at which first time flux enters into the superconductor sample.

Second critical field (Hc_2): the field at which a superconductor material turns normal.

Coherence length (ξ): the length scale over which the superconducting order decays.

London penetration depth (λ): the depth of penetration of the magnetic flux from the surface of a superconductor or the screening length.

Fluxon (θ): the smallest unit of quantized magnetic flux.

Surface resistance R_s: the resistance for AC currents.

Alternating current (AC): occurs when charge carriers in a conductor or semiconductor periodically reverse their direction of movement.

Direct current (DC): is the unidirectional flow or movement of electric charge carriers (which are usually electrons).

YBCO: $YBa_2Cu_3O_{7-x}$.

H^*: Bean's critical field.

Ni: Nickel

NRMA: Non-Resonant Microwave Absorption.

PPMS: Physical Property Measurements System.

ESR: Electron Spin Resonance

EPR: Electron Paramagnetic Resonance.

AFM: Atomic Force Microscopy.

BCS: Bardeen-Cooper-Schrieffer.

RF: Radio frequency.

STEM: Superconductor Technology and Emeging Material.

IMS: Institute of Material Science.

Flux pinning: the phenomenon where a magnet's lines of force (called flux) become trapped or pinned inside a superconducting material.

Hysteresis (loop): hysteresis, as it applies to a superconductor, relates to the dynamic response of a superconductor to a strong magnetic field applied upon it.

Josephson junction: a thin layer of insulating material sandwiched between two superconducting layers.

Penetration depth (also London penetration depth): This term relates to how deeply a magnetic field will penetrate the surface of a superconductor.

Critical current density Jc: is the highest amount of electricity that can flow through a superconductor. Any greater current causes superconductivity to vanish, and the material returns to its normal state.

Critical magnetic field Hc: is the highest value of field (at any given temperature) for which superconductivity remains. Type II superconductors have lower and upper critical fields,Hc_1 and Hc_2.

Critical temperature Tc: is the highest temperature at which a material remains superconducting.

Energy gap: a key concept in the explanation of superconductivity, by which certain energy levels cannot be occupied; it prevents electrons from exhibiting normal behavior.

Flux lattice: a regular array of magnetic flux lines penetrating a superconductor.

Meissner effect: the property of a superconductor by which all magnetic flux lines are forced to stay outside of the superconducting material. This principle is used as the basis for levitation devices.

Normal state: the nonsuperconducting state of a material, in which current flows with electrical resistance, and so on. Materials revert to the normal state either at higher temperatures (above T_c), or in high magnetic fields, or when high current density (above Jc) is passed through them.

Persistent current loop: once started in a loop of superconducting wire, a current flows without running down for indefinitely long times (as long as the material is kept cold).

ABSTRACT

Understanding how and why superconductivity (SC) occurs in a given material has been very challenging for physicists for more than a hundred years, notwithstanding the major milestones, such as the London theory, the Landau-Ginzburg theory, and the BCS theory. The extreme challenge to predict the occurrence of SC is symbolized by the long string of unanticipated but breathtaking advances, i.e., the unexpected discoveries of cuprates and Fe-pnictides being the dramatic modern examples. Because of their incompatibility, the nucleation of SC near a ferromagnet is difficult and has never been realized except for the case that another superconductor provides proximity-boosted Cooper pairs.

This perceived necessity to start with another superconductor is engrained in the extensive study of the proximity effect in superconductor/ferromagnet (S/F) powder sample, where all the structures involve a superconductor with either stable or metastable structure.

Compounding the difficulty, it is also generally recognized that SC with substantial T$_c$ is favourable in low dimensionality because of strong quantum fluctuation. In this thesis, we report a serendipitous finding of SC that emerges under the most implausible circumstances in low field microwave absorption measurement. This new revelation may lead to unconventional avenues to explore novel SC for applications in superconducting spintronics.

By means of a varienty of techniques, including EPR, SEM, FTIR, PPMS/VSM and XRD, nanonickel incorporated YBCO in different weighting factors have been studied. With its complex chemical structure and magnetic properties, Ni-YBCO is far from well understood and the magentic behavior of the system under different conditions is investigated. From the dilute mixture of nanonickel particles, it is found that groups of normal Josephson junctions (JJs) and JJs due to YBCO-nickel-YBCO interparticle weaklinks form as nickel is ferromagnetic. We experimentally show, for the first time multiple phase reversals in the non-resonant microwave absorption (NRMA) spectra from Ni-YBCO possibly, due to the formation of JJs. We also show that these multiple phase reversals then

depend on microwave power and temperature. We argue that microwave power induced coherence among some groups of JJs and breaking of some of the weaker JJs can then lead to the disappearance of multiple phase reversals at higher microwave power levels. Further, we also report a role of pair breaking effects that shall give a linear field dependence of the derivative microwave absorption signal, which is essentially the NRMA signal. This pair-breaking effect dominates at temperatures closer to T_c as expected thermodynamically.

The presence of two peaks in the system, results in high permeability ferromagnet which acts as a magnetic short circuit for magnetic flux density and creates low reluctance path. A transition from normal to anomalous does not occur in this work, because of the possibility of π junction in the sample.

As predictable at the region around the origin where the weaklinks are supposed to be very strong for a very low doping or low nanonickel addition (~ 0.5 % wt), not much effect was observed. However, when the nanonickel addition is increased to 2 % and 3% we see a significant change in the magnetization and the associated hysteresis, indicating flux pinning.

Contents

DECLARATION **xiii**

DEFINITION OF TERMS **xiii**

ABSTRACT **xiii**

1 CHAPTER ONE **1**

1.1 General Introduction 1
1.2 Superconductivity 2
1.2.1 The Meissner Effect 3
1.2.2 Type I and Type II superconductors 3
1.3 Background of the Studies 4
1.4 Cuprates 5
1.5 YBCO 6
1.5.1 Crystal Structure 6
1.5.2 Technological Applications 7
1.6 $YBa_2Cu_3O_{7-x}$ Fundemental Properties 8
1.7 Electrical Transport Properties 8
1.7.1 Anisotropy of the Normal State 8
1.7.2 Granularity and Disorder 9
1.8 Magnetic Properties 11
1.8.1 Phase Diagram 11
1.8.2 Mixed State and Vortex Structure 12
1.9 Nano-Scale lengths in Superconductivity 15
1.10 Problem Statement 15
1.11 Aim and Objectives of the Study 16
1.11.1 Aim 16
1.11.2 Objectives of the Study 17

Reference **18**

2 CHAPTER TWO 21

2.1 Introduction . . . 21
2.2 EPR Spectrometer . . . 21
2.2.1 NRMA Studies . . . 22
2.3 Magnetic Properties of Superconductors . . . 24
2.3.1 Critical Fields . . . 24
2.3.2 Fluxon Quantization . . . 26
2.3.3 Josephson Junction and Josephson Effect . . . 28
2.4 Josephson Coupling Energy . . . 31
2.5 Short Coherence Length and Penetration Depth . . . 31
2.6 Flux Flow and Flux Creep . . . 32
2.7 Flux Pinning . . . 33
2.8 Penetration Depth of Josephson Junction . . . 35
2.9 Lower Critical Field of Josephson Junction . . . 36
2.10 Surface Impedance . . . 37
2.11 Non-resonant Radio/Microwave Absorption Features . . . 38
2.11.1 First, Second and Third Peak . . . 39
2.11.2 Absorption Spectral Lines . . . 39
2.11.3 Magnetic Shielding Effect . . . 40
2.11.4 Phase Reversal . . . 40
2.11.5 Magnetic Hysteresis . . . 41
2.11.6 Surface Barrier Effect . . . 42
2.11.7 Oxygen Deficiency . . . 42
2.11.8 Paramagnetic Meissner Effect . . . 42
2.11.9 AC Loss in Superconducting State . . . 43
2.12 RF and Microwave Loss Mechanisms . . . 43
2.12.1 Portis Model . . . 44
2.12.2 Dulcic Model . . . 45
2.12.3 Josephson Junction Decoupled Model . . . 46
2.13 Critical Current Density . . . 47

2.13.1 The Critical State 48
2.14 The Two-component Critical State Model 50
2.15 Non-resonant Microwave Absorption 50
2.16 Critical Current Density Measurement of YBCO Thin Films by Non-resonant RF Absorption Method 51
2.16.1 Bean Critical State Model 52
2.17 Distinction Between Weak Link and Bulk Responses 53
2.18 Modulated and Non-modulated Low-magnetic Field Microwave Absorption 54

Reference **54**

3 CHAPTER THREE **61**

3.1 High-Tc Superconductors 61
3.2 Processing of High-T_c Superconductor 62
3.3 Processing of Bulk Superconductors 63
3.4 Problem of Preparing Nanoparticles 64
3.5 Structural Ordering of Ferrites 65
3.6 Ferromagnetic Materials 66
3.7 Sample Preparation and Material Synthesis 66
3.8 Processing YBCO Bulk Superconductor 67
3.8.1 Conventional Solid State Reaction Method 67
3.8.2 Texturing of YBCO 123 Superconductors 68
3.8.3 Sol-gel Method 69
3.8.4 Microwave Processing Method 70
3.8.5 Physical and Chemical Deposition Methods 72
3.9 Influence of Dopants 72
3.10 Effect of Nickel Dopant 73
3.10.1 Experimental Preparion of YBCO Powders by Solid State Route . . 73
3.10.2 Nano-nickel Powders 74
3.10.3 Material Incorporation 74

Reference **75**

4 CHAPTER FOUR **77**

4.1 Measurements and Data Collection 77

4.2 Scanning Electron Microscopy (SEM) 77

4.3 Non-Resonant Microwave Absorption Technique (NRMA) 79

4.4 X-Ray Diffraction (XRD) Measurements 83

4.4.1 Important Parameters from XRD Data 85

4.5 Fourier Transform Infrared Spectroscopy (FTIR) 87

4.5.1 Sample Analysis Process 88

4.5.2 Sample Preparation 89

4.5.3 Working of an FTIR Spectrometer 89

4.6 Vibrating Sample Magnetometer (VSM) 91

4.6.1 Measurement Principle 91

4.6.2 Hysteresis 92

Reference **94**

5 CHAPTER FIVE **97**

5.1 Non-resonant Microwave Absorption in Nanonickel added YBCO Powders: Observation of Multiple Phase Reversals. 97

5.1.1 Introduction 97

5.1.2 Experimental 98

5.1.3 Results and Discussion 99

Reference **103**

6 CHAPTER SIX **105**

6.1 Non-resonant Microwave Absorption Signals in Nanonickel added YBCO Superconducting powders: Distinctive Observation 105

6.1.1 Introduction 105

6.1.2 Experiment 106

6.1.3 Results and Discusion 107

Reference **111**

7 CHAPTER SEVEN **114**

7.1 Magnetic Proximity Effect in Ni-YBCO Superconductor 114

7.1.1 Introduction 114

7.1.2 Experimental 115

7.1.3 Results and Discussion 116

Reference **121**

8 CHAPTER EIGHT **124**

8.1 Conclusion 124

List of Figures

1 Electrical resistivity disappearance below Tc of mercury[4]. 2

2 The crystal structure of $YBa_2Cu_3O_{7-x}$ superconductor[4]. 7

3 Electrical resistivity behaviour along the three crystallographic axes for an untwinned $YBa_2Cu_3O_{7-x}$ single crystal [12]. 9

4 Resistive transition in a granular superconductor [12]. 10

5 Mean-field type phase diagram for a type-II superconductor [12]. 12

6 The mixed state structure in a type-II superconductor. The Figure 6(a) shows a lattice of normal cores and the respective vortices, while the Figure 6 (b), shows the variation with position of superparticles density and the Figure 6 (c), shows the variation of flux density with position [12]. 13

7 Representative scheme showing intragranular and intergranular vortices in a type-II superconductor [12]. 14

8 Disconnected loops circulating in the grains [18]. 16

9 Example of the coated conductor architecture [20] 17

10 (a) H-T phase diagram of type I superconductor and (b) Magnetization of long solid cylinder I superconductor[21]. 25

11 (a) HT sketch for type II superconductor and (b) Magnetization of a long solid cylinder type II superconductor. Figure 11 (b) was reprinted from [21]. 26

12 Schematic Josephson junction showing two superconductors separated by an insulating layer [29]. 30

13 Signal depicting hysteresis measured on ZFC $YBa_2Cu_3O_7$ bulk samples at 78 K [47]. 35

14 T-H phase diagram for different superconducting materials[79]. 49

15 A schematic block diagram of SEM [4] 78

16 A picture of SEM used in this work, JEOL JSM-7500F. 79

17 Line shape of YBCO superconductor sample [23]. 80

18 A schematic block diagram of EPR spectrometer [26]. 82

19 A picture of EPR used in this work, Bruker EXM spectrometer. 83

20 Schematic of the X-ray diffraction by a crystal [27]. 84

21 A schematic representation of X-ray diffraction [28]. 84

22 A picture of typical XRD instrument. 85

23 Michelson interferometer [30]. 88

24 (a) Schematic diagram of FTIR and (b) FTIR instrument [31]. 90

25 Schematic representation of a VSM [32]. 91

26 VSM Virgin curve [35]. 93

27 Hysteresis loop of a ferromagnetic material [35]. 94

28 NRMA in the Ni-YBCO powder measured at various temperatures with 100 mW and 5 G modulation amplitude. One can notice multiple phase reversal at 20 K, 60 K, and 70 K. Inset shows the ESR signal in the normal state which enables to compare the phases of resonant signal with that of the NRMA signals. 100

29 NRMA in the Ni-YBCO powder measured at various temperatures with 158.5 mW and 5G modulation amplitude. Shift of phase reversal temperature from 20 K to 30 K and disappearance of multiple phase reversals to be noted. 101

30 NRMA signals from YBCO powder without nano nickel addition, and absence of phase reversal to be noted. Also one can see that the T_c to be around 90 K as the NRMA signal becomes very weak. 101

31 Optical micrograph of 2% Ni-YBCO powder. One can notice clusters of YBCO-Ni-YBCO-YBCO inter particle connected loops as shown by arrow in the picture. Inset shows typical YBCO particle size of the order of microns and the nickel particle agglomerates of submicron size. 102

32 Zoomed NRMA in the Ni-YBCO powder measured at 70 K with 100 mW and 5 G modulation amplitude. 103

33 Powder X-ray diffraction of YBCO and Ni-YBCO sample. 107

34 SEM image of Ni-YBCO at high magnification. 108

35 Non-resonant microwave absorption derivetive of Ni-YBCO recorded at different temperatures with microwave power of 158.5 mW. 108

36 NMRA hysteresis Ni-YBCO recorded at different temperatures with microwave power of 158.5 mW. 109

37 The X-ray diffraction powdered patterns for Ni-YBCO (0.5, 1.2, 2, and 3 %wt). 117

38 FTIR spectra in the range 4000-200 cm^{-1} to facilitate the investigation of the nature of the chemical bonds. 118

39 EDX spectra and elemental maps of Ni-YBCO. 118

40 The SEM micrographs of Ni-YBCO. 119

41 Magnetic hysteresis loops of the Ni-YBCO at 50 K. 119

42 Magnetic hysteresis loops of the Ni-YBCO at 50 K enlarged region around the origin. 120

1 CHAPTER ONE

1.1 General Introduction

Shortly after the discovery of high-T_c superconductors there was an influx of publications where the EPR technique was used to investigate their properties [1]. As no new substantial information was obtained through this technique, it was soon almost abandoned. The fact that EPR technique provided a large number of experimental data in the superconducting regime, without significantly contributing to the deeper understanding of high-T_c superconductors was also puzzling.

Meanwhile, the continuous effort of this workto further investigate superconductivity using the EPR technique yielded important experimental and theoretical results related to properties of high-T_c superconductors. Furthermore, some of these results are unique as they were not obtained with conventional experimental techniques. The work shows that an EPR spectrometer is a powerful tool to investigate properties of superconductors. As superconducting systems are not conventional paramagnetic substances, the EPR signals do not originate from the usual resonant absorption, namely magnetic dipolar transitions between spin levels [1]. Thus, it is essential in analyzing the experimental results, to explore the mechanism that induces the EPR signals. Indeed, by detailed experimental and theoretical studies of the EPR spectra of different high-T_c superconductors, it has been possible to comprehend the mechanism that induces the observed microwave absorption. Based on these results, new unknown properties of superconductors were obtained.

As the EPR spectrometer is the central experimental tool in the present work, a description of the EPR spectrometer detail will be given in Chapter Two for better understanding of its various functions. Among experts in superconductivity many are not familiar with the elements of the EPR spectrometer, including how and what it measures and hence this discription is crucial.

We then continue by presenting experimental results obtained in high-T_c superconductors subjected to various factors such as DC and AC magnetic fields, temperature, sample orientation and to different sample treatments such as zero-field-cooling or field-cooling. This overview will allow a systematic classification of the measurements and will provide the theoretical background [2] necessary to analyze these experiments and to understand the inherent physics. The presentation is based on publications by the authors over a period from just after the discovery of high-T$_c$ superconductors to date [1]. Before coming to the actual problem it is tradition to start defining the supercondutivity.

1.2 Superconductivity

One of the most interesting property of metals and alloys at low temperatures is that their electrical resistivity vanishes entirely below a certain temperature. This temperature depends on the substance and the zero resistivity or infinite conductivity of the material is known as 'superconductivity'. Superconductivity can be explained as a state of matter whereby the correlation of conduction electrons allows a static current to pass through without a resistance as static magnetic flux is excluded from the bulk of the material [3]. Superconductivity was discovered in 1911 by H. Kamerlingh Onnes in Leiden just three years after he first liquified helium, which made sufficiently low temperatures possible. He found that below 4.15 K the DC resistance of mercury dropped to zero as seen in Figure 1.

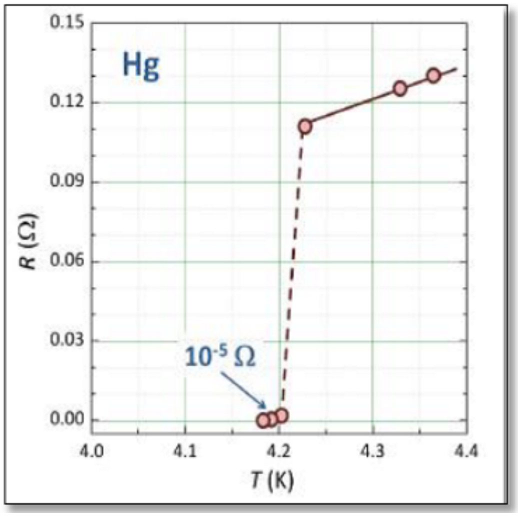

Figure 1: Electrical resistivity disappearance below Tc of mercury[4].

In other words, above this temperature, the resistivity is small, but finite, while the resistivity below this temperature is so small that it is essentially zero. The temperature at which the transition takes place is called the 'critical temperature'. It is one of the most important characteristic property of the superconductors.

1.2.1 The Meissner Effect

One of the most spectacular properties of a superconductor is the Meissner effect, which is the phenomenon of total expulsion of magnetic flux from the superconductor. This implies that in the Meissner state (B$\equiv$ 0) a superconductor is a perfect diamagnet with a susceptibility $\chi = 1$. This will hold with increasing applied field until a certain values, where it is no longer energetically favorable to uphold the Meissner state [4].

1.2.2 Type I and Type II superconductors

Two types of superconductors exist, type I and type II. Type I usually has quite low T$_c$, and will uphold the Meissner state, up to a critical field H$_c$ at which the superconducting state breaks down completely. Type II will as type I expel the magnetic field up to a certain field H$_{c1}$, where it is energetically favorable to allow flux penetration in the form of flux lines. The density of flux lines will increase with the applied field to a field H$_{c2}$ where there is no more room for the superconductivity, as the distance between the flux lines is less than the Cooper pair coherence length. The distinction between the two types may given by the following:

Type I: $\kappa = (\lambda/\xi) < 1/\sqrt{2}$

Type II: $\kappa = (\lambda/\xi) > 1/\sqrt{2}$

where λ, is the London penetration depth and ξ is the coherence length of the Cooper pairs [5]. Coherence length, ξ characterizes the distance which a weak magnetic field penetrates a superconductor, or in other words, how the penetration of an external field into the superconductor will be damped with distance r as e$^{-r}/\lambda$.

ξ characterizes the minimum length over which the quantum mechanical phase can be changed by π without destroying the superconductivity, or equivalently the length scale over which the superconducting order parameter ϕ is unchanged. Metallic elements which are superconducting are typical type I superconductors, with large coherence lengths and small penetration depths. Type II superconductors have large penetration depths and small coherence lengths.

The cuprate high-T$_c$ superconductors are extreme type II superconductors, typically with $\lambda \sim 2000$ Å , and $\xi \sim 25$ Å [5]. Another distinction in superconductivity is whether the superconductor can be described by the Bardeen, Cooper and Schrieffer (BCS) theory [12]. According to BCS theory, superconductivity is phonon-mediated, which means that the phonons encourage an electron-electron coupling this allowing the electrons to form a Cooper-pair [12]. The Cooper-pairs are bosons and Bose-condensate below a certain temperature. BCS theory can explain superconductivity in most type I and several type II materials, but is, however, not applicable to the cuprate superconductors, which are still far from being understood. The mechanism behind superconductivity in these materials is something different, and several explanations such as charge stripes have been proposed [12].

1.3 Background of the Studies

The HTSCs discovered by Bednorz and Muller [6] are known to show many interesting physical properties which are qualitatively different when compared with the conventional superconductors. Unavoidable defects present in these materials (HTSC) can act as weak-links because of the very short coherence length (10 Å), which is a major feature of these materials. This leads to granularity in these superconductors, on different length scales, namely inter-grain, intra-grain, inter domain (twin boundaries) etc. Weak links properties and percolation then influence the transport, the magnetic and the electrodynamics (e.g. microwave response) properties [6]. One striking example of this is the 'non-resonant microwave and RF absorption' first observed in the cuprite superconductor by Bhat et al., [7]. Other names for the phenomenon in the literature are 'magnetically modulated microwave absorption' and 'low field microwave absorption'. Intense microwave or RF absorption which is highly sensitive to magnetic field and temperature at and below T_c (i.e. in the superconducting state of the material) is measured as a function of the DC magnetic field (typically swept between -100 Oe and 100 Oe) with superposed low-field frequency AC fields (0.01-10 Oe) using continuous wave (CW) NMR or EPR spectrometers. Since most of the special features associated with the HTSC materials have a direct influence on the non-resonant microwave and RF absorption, we shall discuss these in chapter two and other relevant properties of superconductors.

1.4 Cuprates

There are three main families of hole-doped cuprate HTSC studied today. However, much of the confusion in the study of HTSC results from the fact that each material is accessible to different experimental techniques.

Hence, it is easy to measure the electronic density of states of $Bi_2Sr_2CaCu_2O_{8+x}$ (BSCCO), but harder to measure its magnetic properties. In the quest to find a unifying theory for all HTSC, it is tempting to treat these three as one material, and combine the experimental results from all families. Because of this common practice, the field of high-Tc research is rife with conflict and apparent contradictions. A good summary of many of the known hole-doped HTSC materials along with an explanation of the variation in their Tc's is given by Eisaki et al., [8].

The lanthanum family , $La_{2-x}Sr_xCuO_2$ (LSCO) of high-Tc's was the first family of materials to be discovered by Bednorz and Muller in 1986. LSCO is physically the hardest of the three materials, and with stronger bonds. It is easier to grow large (> 1 cm) single crystals. Neutron scattering experiments, which probe the magnetic structure of the material, are typically limited to studying LSCO because of their requirement for large single crystals [8].

The discovery of YBCO followed that of LSCO within a year. YBCO was the first material to break the 77 K (liquid nitrogen) temperature boundary. The optimal T_c is now $> 90K$. YBCO has perhaps been the most highly studied because it is the cleanest and most ordered crystal. But studies of YBCO can also be quite confusing because there are two CuO planes: the square plane and the chain plane. By analogy with the other HTSC families, it is thought that the superconductivity originates in the square plane, but it is hard to isolate the behaviors of the planes [7].

Finally BSCCO was discovered in 1988. BSCCO itself can have 1, 2, or 3 CuO planes, with T_c increasing with the number of planes. Bismuth can also be replaced with thallium or mercury, which results in the highest T_c material known ($\sim$ 135 K). BSCCO competes with YBCO as the most technologically useful material. YBCO has been used in magnetic field applications because it is easier to pin flux. YBCO is used to grow high-T_c SQUIDS with grain-boundary Josephson junctions [8].

1.5 YBCO

This section will be used to give a brief introduction to crystal structure and the electronic, magnetic and superconducting properties of YBCO.

1.5.1 Crystal Structure

Unlike conventional metallic superconductors, the crystal structure of the HTSC is complex. One of the most important characteristic in high-T_c superconductors is the planar anisotropy and Figure 2 shows the crystal structure of $YBa_2Cu_3O_{7-x}$ superconductor [4].

The typical lattice parameters are a = 3.82 Å, b = 3.89 Å and c = 11.68 Å. As shown in Figure 2, the $YBa_2Cu_3O_{7-x}$ superconductor is a perovskite-type cuprate with orthorhombic symmetry and the main structural characteristic is the presence of Cu-O_2 double planes separated by a yttrium atomic layer. The Cooper pairs, responsible to superconducting properties, are placed in the CuO_2 double planes [8]. The atomic structures between the conducting planes are denominated charge reservoir. The oxygen content can vary between 6 and 7 atoms per unit cell. Deoxygenated systems (x= 1

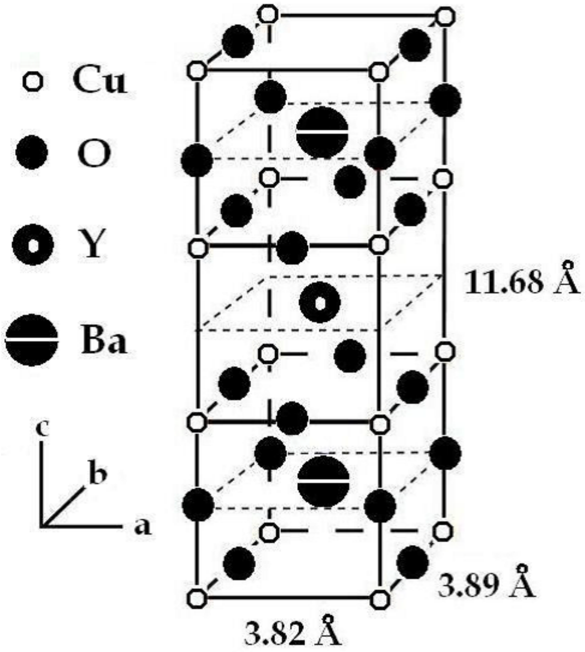

Figure 2: The crystal structure of $YBa_2Cu_3O_{7-x}$ superconductor[4].

or simply 6 oxygen atoms per unit cell) has tetragonal structure and insulating antiferromagnet behaviour. For the optimum oxygen content of $x \approx 0.07$ the $YBa_2Cu_3O_{7-x}$ system has the biggest superconducting temperature at around 93 K.

1.5.2 Technological Applications

The $YBa_2Cu_3O_{7-x}$ superconductor is propably most popular the high-T_c system for technological applications due to its high critical current density and high-performance in applications involving high-magnetic fields. The relative facility in the growth of samples with specific shape permits their use in large scale. Due to the high performance in magnetic and electrical properties the materials prepared by melt-textured and thin films techniques have contributed decisively in this direction. Several applications involving $YBa_2Cu_3O_{7-x}$ superconductor have been made since its discovery in 1987. Masato Murakami [9] proposed two definitions for classify the applications of bulk high-temperature superconductors, named passive applications and magnet applications. In passive applications the high-temperature superconductors can be used in superconducting bearing systems, flywheels, cryogenic pumps, hysteresis motors (as rotor), etc. Examples for magnet applications include quasi-permanent magnets, maglev trains, magnetic clamps, motors (as stator), magnetic bumpers, in high-field physics, and magnetization devices.

The importance of high-performance in current transport associated with a low-cost process to the fabrication of single grain bulk superconductors is also pointed out as one of main factors to effective applications in engineering devices by Hari Babu et al., [10].

An important review by Pissas et al., [11] on power applications of high-T_c superconductors points out the need for low-cost fabrication coupled with high-performance in electric current transport. This would allow producing large-scale superconducting electric devices for power industry, such as power cables, magnetic energy-storage devices, transformers, fault current limiters, etc. $YBa_2Cu_3O_{7-x}$ superconductor is poised to become one of the best candidates for these applications.

1.6 $YBa_2Cu_3O_{7-x}$ Fundemental Properties

This section is dedicated to a review about electrical and magnetic properties of the hightemperature superconductors, with special attention to the $YBa_2Cu_3O_{7-x}$ system.

1.7 Electrical Transport Properties

In this sub-section some fundamental aspects of the electric properties of the high temperature superconductors will be discussed, with emphasis in the anisotropy of the normal state and in the granularity and disorder effects.

1.7.1 Anisotropy of the Normal State

The transport properties of the high-temperature superconductors are highly anisotropic due to their crystalline structure. The CuO_2 atomic planes (ab planes) are good conductors but separated by highly resistive sheets, resulting in a strong planar anisotropy, with a low conductivity along the c-axis. The electrical current transport in $YBa_2Cu_3O_{7-x}$

superconductor is metallic-type along the ab plane. The same transport behaviour along the c-axis is also achieved in good quality samples. Figure 3 shows the electrical resistivity behaviour along the three crystallographic axes for an untwinned $YBa_2Cu_3O_{7-x}$ single crystal [8]. The strong anisotropic character can be observed with a ratio at room temperatures of $\rho_a/\rho_b > 2.5$. and $\rho_b/\rho_c > 30$.

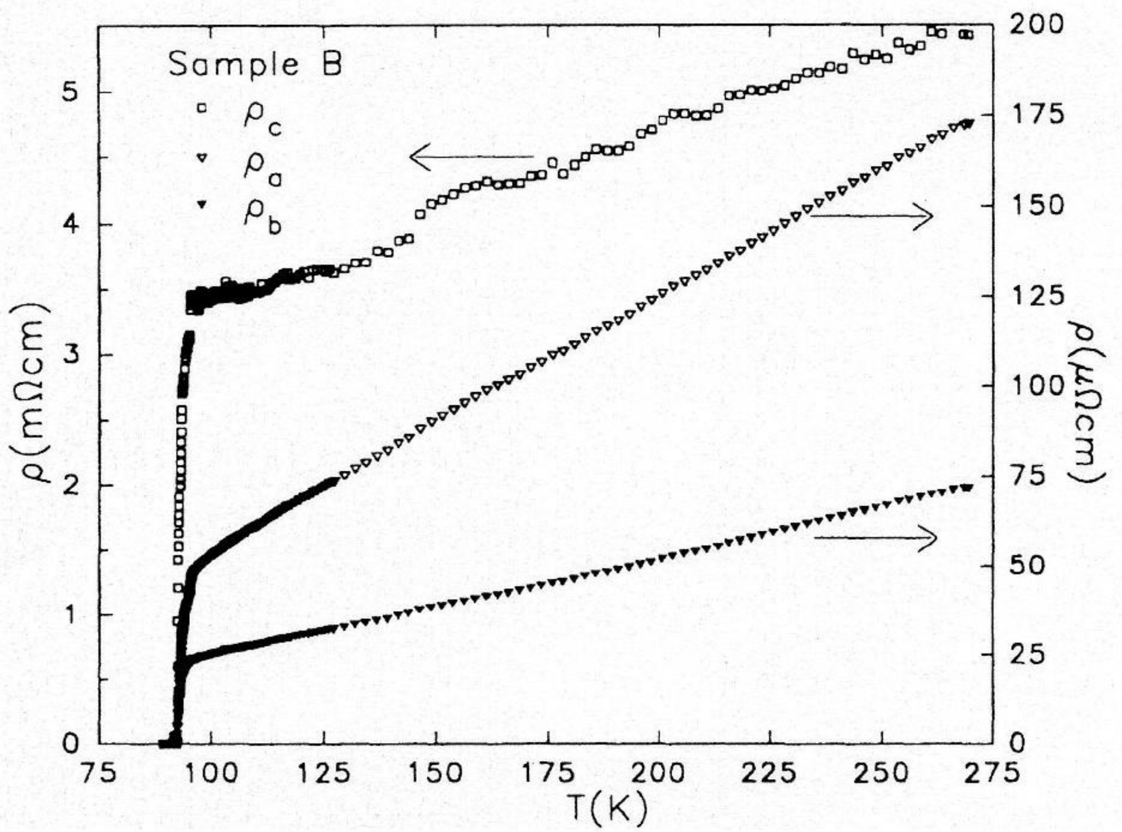

Figure 3: Electrical resistivity behaviour along the three crystallographic axes for an untwinned $YBa_2Cu_3O_{7-x}$ single crystal [12].

1.7.2 Granularity and Disorder

The coherence length (T = 0 K) of an $YBa_2Cu_3O_{7-x}$ superconductor is approximately 12-20 Å along the ab plane and 1-3 Å along the c-axis, while the penetration length is about 1000 Å.

As a consequence the $YBa_2Cu_3O_{7-x}$ system is classified as an extreme type-II superconductor. Therefore defects of the same (or higher) order of magnitude are very important in these materials. The high-temperature superconductors present several intrinsic defects in different size scales: macroscopic (grain-boundaries, porosity, non-superconducting phases, such as the $Y_2Ba_1Cu_1O_5$ phase in some melt-textured $YBa_2Cu_3O_{7-x}$ samples), mesoscopic (twin-planes, dislocations, stacking-faults, columnar defects) and microscopic (oxygen vacancy, substituting atoms). The existence of these defect levels is responsible for the complex topology of the order parameter. Samples with higher disorder degree present an intrinsic and complex granularity, and this inhomogeneous character reflects in the magnetic and transport properties. Disorder is relevant since the discovery of the HTSC's, when its presence was associated the superconducting-glass state [13]. The resistive transition to the superconducting state in granular systems occurs in two steps like transition, defining two important temperatures, namely T_c and Tc_0, as presented in Figure 4.

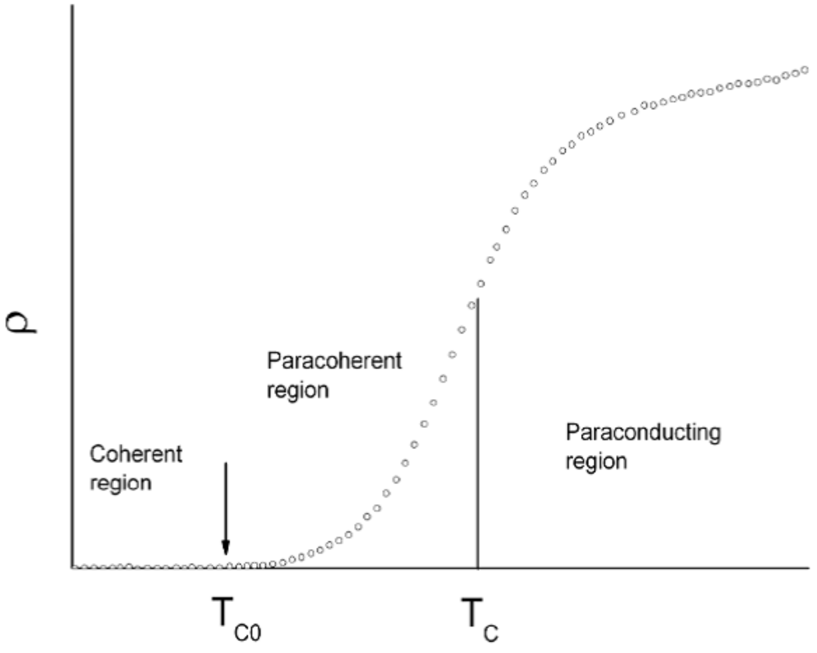

Figure 4: Resistive transition in a granular superconductor [12].

The region above T_c is called "paraconducting" region and the excess of conductivity is attributed to thermal fluctuations of the amplitude of the order parameter. T_c is practically coincident with the bulk critical temperature, and the superconductivity stabilizes in homogeneous and mesoscopic regions of the sample (grains). Between Tc and Tc_0 the superconducting grains are weakly coupled to each other by Josephson effect and thermal fluctuations occur in the phase of the order parameter of the grains. This region is called ”paracoherent” region and the electrical resistivity is not zero. The long-range superconducting state is achieved at T_{c0} through a percolation process at the grains. This process controls the activation of weak links between the superconducting grains and is called coherence transition. A detailed investigation of this process is given by Rosenblatt et al., [14]. At the critical temperature (T_{c0}) where the coherence transition sets in, the fluctuating phases of the order parameter in each grain couple to each other into a long-range ordered state and a zero resistivity state is established.

1.8 Magnetic Properties

In this section we will be discuss some fundamental aspects of the magnetic properties of the high-temperature superconductors.

1.8.1 Phase Diagram

The zero resistivity and the perfect diamagnetism (Meissner effect) are the main characteristics to any material be considered a superconductor [12]. Figure 5, shows a mean field type phase diagram for a type-II superconductor, such as $YBa_2Cu_3O_{7-x}$. Type-II superconductors present a perfect diamagnetism (Meissner effect) just when the applied magnetic field is lower than H_{C1}(T), called as lower critical field. Consequently this region is known as Meissner state. For applied magnetic fields in the region between H_{C1}(T) and H_{C2}(T), the magnetic flux can penetrate inside the superconductor in form of filamentary structures known as vortices [12]. This state is known as mixed state and the H_{C1}(T) value marks the penetration of the first magnetic flux-line inside the superconductor. When the external magnetic field is higher than H_{C2}(T)) (also known as upper critical field), the superconductivity is suppressed and the material passes to the normal state.

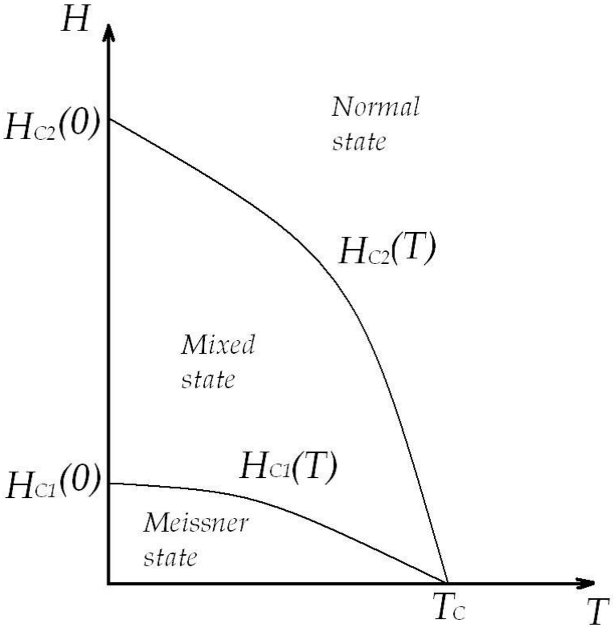

Figure 5: Mean-field type phase diagram for a type-II superconductor [12].

1.8.2 Mixed State and Vortex Structure

Figure 6, shows the mixed state structure in a superconducting sample where Ha is the applied magnetic field ($H_a > H_{C1}$). Figure 6 (a), shows a lattice of normal cores and the respective associated vortices, while Figure 6 (b), shows the variation with position of superparticles density (superel ectrons density or Cooper pairs density). Figure 6 (c), shows the variation of flux density with position. The superparticles density, designed by nS, falls to zero at the centre of each isolated vortex, and the dip in the nS is about two coherence lengths wide. The flux density in not cancelled inside the normal cores, but decreases into a small value in a distance about λ (London penetration length) away from the normal cores, as shown in Figure 5 (c). Each individual vortex is surrounding by the shielding currents and the total flux generated is just one fluxon Φ_0, given by 2.067 $\times 10^{-15}$ Weber.

The interaction between vortices is repulsive and mediated by the Lorentz force. In a homogeneous superconductor the cores are arranged in a hexagonal (triangular) periodic array due to lower energy state. This array is known as Abrikosov lattice and can be

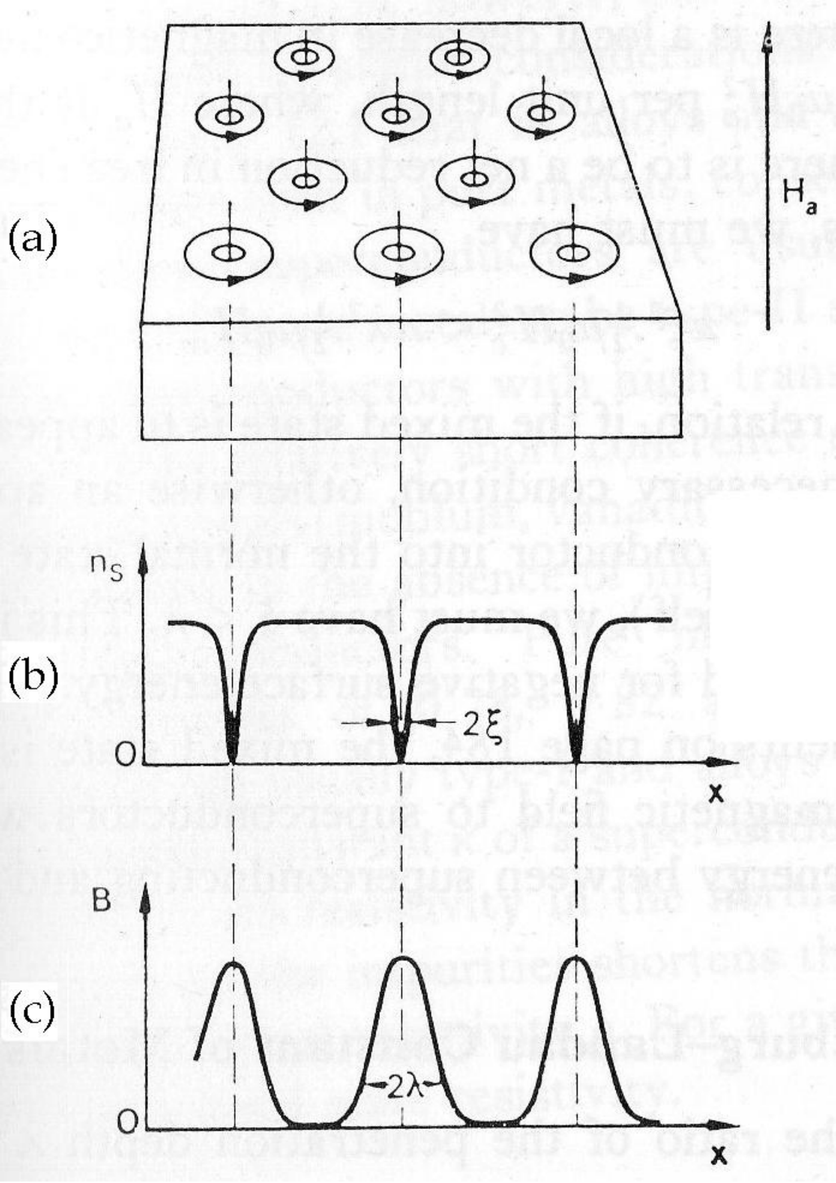

Figure 6: The mixed state structure in a type-II superconductor. The Figure 6(a) shows a lattice of normal cores and the respective vortices, while the Figure 6 (b), shows the variation with position of superparticles density and the Figure 6 (c), shows the variation of flux density with position [12].

observed in Figure 6 (a). In granular superconductors the vortices placed inside the superconducting grains are denominated intragranular vortices and are arranged in this lattice type. The vortices can be pinned by defects of the crystal lattice. This effect is known as flux pinning and the mechanism can be improved by introducing microstructural or compositional changes like irradiation, chemical doping or precipitates. In an isotropic and perfect superconductor (without the presence of defects) the vortices can be arranged in an Abrikosov lattice (hexagonal lattice). In a granular material, the superconducting grains can be coupled by Josephson effect. John R. Clem proposed a theoretical model to describe a granular superconductor using the Josephson effect as starting point [15]. In this model a granular superconductor can be represented as anisotropic grains coupled by Josephson junctions (junctions based on Josephson effect). The magnetic field can penetrate into a granular superconductor in the region between the grains, in the form of intergranular vortices, known as Josephson vortices. An intergranular Josephson vortex transports just one fluxon, it is similar to intragranular Abrikosov vortex and the magnetic structures. The main difference is the region where both vortices are located. Figure 7, shows a scheme of both vortices in a superconducting granular sample.

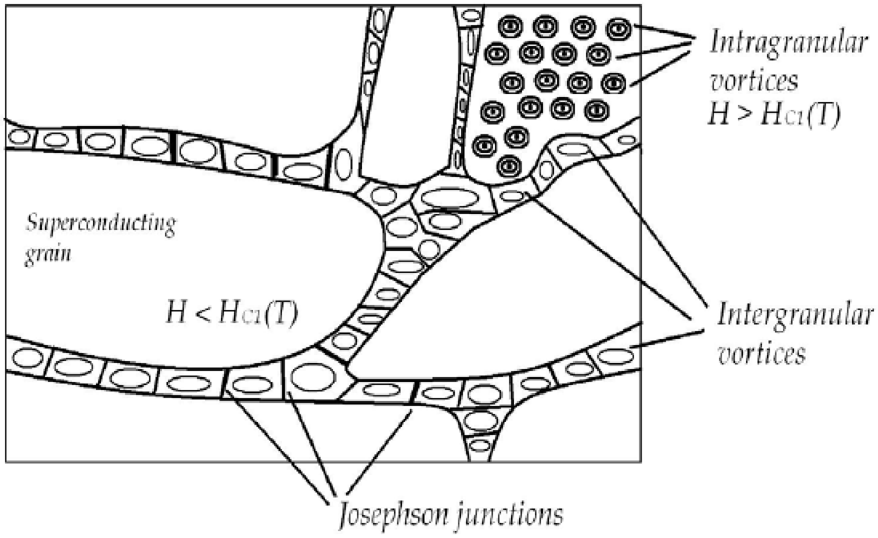

Figure 7: Representative scheme showing intragranular and intergranular vortices in a type-II superconductor [12].

1.9 Nano-Scale lengths in Superconductivity

Considering the nano-scale lengths in superconductivity, the coherence length, $\lambda >> 0$ and the London penetration depth L, the idea that approaching these length, would lead to changes in the superconductivity, is close. Similarly the magnetic correlation length Å, is a length scale which can be approached to investigate finite size effects. Raittila et al., [16], used a citrate-gel method to manufacture the nanosized YBCO powder. They studied the morphology of the powder using atomic force microscopy (AFM), as well they studied the physical properties using X-Ray diffraction and SQUID magnetometry, funding the particles to be disc-shaped with a significant diameter-distribution, crystalline with a slightly reduced c-axis and exhibiting a gradual Meissner effect. Other studies of small particle YBCO systems, focusing on structure and oxygen ordering, such as Hilgenkamp et al., [16] have been performed. However, incoporating Nickel nano magentic particle into superconduting YBCO nanosized systems has to our knowledge not been explored.

1.10 Problem Statement

The main issue for the cuprates is that grain boundaries between mis-oriented crystallites obstruct current flow because the critical current density through a grain boundary

$$\mathrm{J}_{\mathsf{gb}}(\theta) = \mathrm{J}_{\theta} \exp\left(\frac{-\theta}{\theta_0}\right) \tag{1}$$

drops exponentially as the mis-orientation angle θ increases [17]. Here $\theta_0 \approx 3$ to 5^o so the spread of mis-orientation angles $\Delta\theta \sim 4\theta_0$ in polycrystals can reduce J_{gb} by 2 to 3 orders of magnitude. Recent experiments revealed similar weak-linked grain boundaries in $Ba(Fe_{1-x}CO_x)_2As_2$ bicrystals and polycrystalline $LaFeAsO_{1-x}F_x$. The current-limiting grain boundaries in cuprates [17] were immediately recognized as a serious obstacle for applications because, instead of flowing along the wire, current breaks into disconnected loops circulating in the grains as shown in Figure 8.

This problem has been revealed by the coated conductor technology in which the

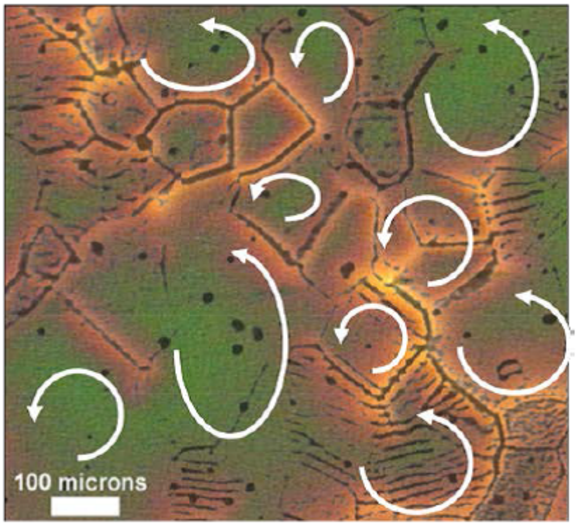

Figure 8: Disconnected loops circulating in the grains [18].

fraction of high-angle grain boundaries with $\theta > 5-7^o$ is reduced by growing YBCO films on textured metallic substrates [19]. Figure 9, shows an example of the coated conductor architecture, which makes the idea of YBCO single crystal by the mile a reality.

Currently long (hundreds of meters) coated conductor tapes are withdrawn on commercially for power and magnet applications [13] by tour de force of materials science and engineering.

1.11 Aim and Objectives of the Study

1.11.1 Aim

The aim of this research is to incorporate nanomagnetic particles Ni nanomagnetic material into grain boundaries of YBCO superconducting material. The main reason for incorporating nanomagnetic particles in YBCO superconductor is to use it for enhancing flux pinning in superconductors. The key research question that needs to be answered is the percentage improvement on the effect of nanomagnetic pinning on low field microwave/RF absorption as a function of percentage by wt%.

We also observe another by-product that comes out of these experiments, namely the

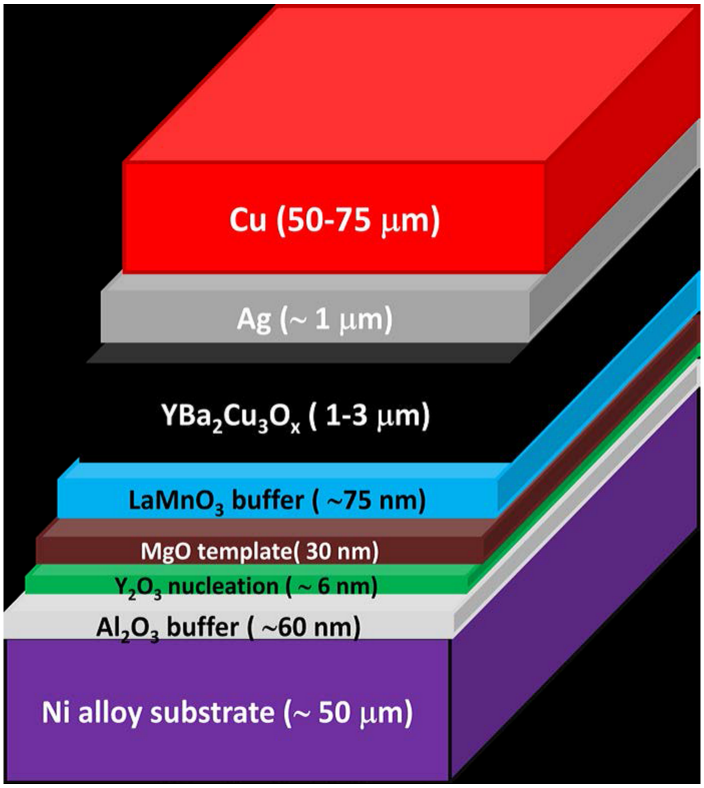

Figure 9: Example of the coated conductor architecture [20]

RF absorption properties. This is because we measure J_c using a low field modulated RF absorption technique.

1.11.2 Objectives of the Study

High temperature superconductors are known to have very short coherence lengths [21] of the order of unit cell because of less coupling between layers [22] which as a consequence, results to the formation of weak links. Depending on the material separating the superconducting grains, the weak links can be either superconductor-insulator-superconductor or superconductor-normal superconductor.

The presence of these unavoidable defects influences transport, magnetic and electrodynamic (radio frequency and microwave) properties of a material. For instance, the application of a very small external magnetic field to a sample at temperatures below T_c, results in an intense low field microwave/radio frequency absorption signal.

The electromagnetic response signal obtained can be either zero field minimum where the signal increases monotically with increase in applied external magnetic field [23] or it can be a zero field maximum and it decreases with increase in magnetic field [24]. Furthermore, the signal shows complex characteristics and features when temperature, frequency, microwave power and field modulation are varied.

The first objective was to study the line shape evaluation by adding different wt% / volume fraction of nano magnetic impurities into YBCO grain boundaries. The study will enable understanding of the electromagnetic response on a sample of Ni-YBCO powders by means of NRMA technique and more especially the low field scan microwave absorption. This will be achieved by studying of the effect of temperature variation, microwave power variation and field modulation amplitude variation on NRMA line shapes which have been noted to have complex but fascinating features in cuprate forms.

The second objective was to study magnetic properties in the Ni incoporated YBCO using PPMS/VSM technique. This study will look at the superconducting properties and magnetic hysteresis of Ni-YBCO sample. Hence, the study provides the possibility to induce spin-triplet superconductivity in oxide-based superconductor/ferromagnet heterostructures.

Finally the formation of possible junction with ferromagnetic nano particle incorporated into the YBCO grain boundaries was studied.

References

[1] V.V. Srinivasu ,*J. Supercond. Nov. Magn.* 23, 305308 (2010).

[2] D. Shaltiel, H.A. Krug von Nidda, B.Y. Shapiro, B. Rosenstein,A. Loidl, B. Bogoslavsky, I. Shapiro, T. Fujii, T. Watanabe, T. Tamegai,*J. Supercond. Nov. Magn.* 22, 387399 (2009).

[3] J. Khachan and B. Stephen , Superconductivity http://www.physics.usyd.edu.au/ khachan/PTF/Superconductivity.pdf online last taken 16 March (2017).

[4] T. P. Sheahen, Introduction to high-temperature superconductivity Kluwer Academic Publishers New york, Boston, Dordrecht, London, Moscow High- Temperature Superconductivity eBook ISBN: 0-306-47061-6 Print ISBN: 0-306-44793-2

[5] Y. Grigorashvili,Superconductor properties technology and applications Published by InTech Janeza Trdine 9, 51000 Rijeka, Croatia Copyright 2012 InTech ISBN 978-953-51-0545-9 First published April, (2012).

[6] K.W. Blazey, K.A. Muller, J.G. Bednorz, W. Berlinger, G. Amoretti, E. A. Buluggiu, and F.C. Matacotta,*Phys. Rev.* B 36 7241 (1987).

[7] S.V. Bhat, P. Ganguly and C.N.R. Rao, *Pramana J. Phys.* 28 L425 (1987).

[8] H. Eisaki, N. Kaneko,D. L. Feng, A. Damascelli, P. K. Mang, K. M. Shen, Z.X. Shen, and M. Greven, *Physical Review.* B 69, 064512 (2004)

[9] M. Miryala, M. R. Koblischka, K. Iida and M. Murakami, *Physica.* 7, 491-493 (2004).

[10] N.H. Babu, Y.H. Shi, S.K. Pathak, A.R. Dennis and D.A. Cardwell, *Physica.* C 471 (5-6), 169 - 178 (2011).

[11] M. Pissas, E. Moraitakis, D. Stamopoulos,G. Papavassiliou,V. Psycharis and S. Koutandos , *Incorpor. Nov. Magn.* Vol 14, No. 5, 10 (2001).

[12] T.D. Fabio, Interpretations and Possible Correlations DOI 10.5772/38401, April (2012).

[13] C. Ebner and D. Stroud, *Phys. Rev.* B 31, 165 (1985).

[14] J. Rosenblatt, A. Raboutou, P. Peyral and C. Lebeau, *Phys. Appl.* 25 73-78 (1990).

[15] J.R. Clem and Z. Hao,*Phys. Review* . B, vol 48, no 18,11 (1993)

[16] J. Raittila, H. Huhtinen, P. Paturi, Yu.P. Stepanov, *Physica* . C 371 9096 (2002).

[17] H. Hilgenkamp, and J. Mannhart, *Rev. Mod. Phys.* 74, 485-549 (2002).

[18] D. Larbalestier, A. Gurevich, D.M. Feldmann, and A. Polyanskii,*Nature* 414, 368-377 (2001).

[19] B. Maiorov, S.A. Baily, H. Zhou, O. Ugurlu, J.A. Kennison, P.C. Dowden, T.G. Holesinger, S.R. Foltynm and L. Civale, *Nature Materials* 8, 398-404 (2009).

[20] A. Gurevich, *Nature Materials* 10, 255259 (2011).

[21] G. Deutscher and K.A. Muller, *Phys.Rev.* Lett 59, 1745 (1987).

[22] P.J.W. Moll, X. Zhu,P. Cheng,H.H. Wen and B. Batlogg ,*Nat. Phys.* 10, 1038 (2014).

[23] V.V. Srinivasu, B. Thomas, M.S. Hegde and S.V. Bhat, *J. Appl. Phys.* 75, 4131 (1994) .

[24] S.V. Bhat, V.V. Srinivasu, and N. Kumar, *Phys. Rev.* B 44, 10121 (1991) .

2 CHAPTER TWO

2.1 Introduction

HTSC has captivating features which are closely related to or have direct influence on non-resonat microwave absorption and radio frequecy. This chapter is dedicated to elaborating on some of the relevant magnetic parameters and properties in relation to electromagnetic dynamics of supercondutors. The discussion on the critical state and related models such as the Bean , Dulcil and Porties, etc are also included.

2.2 EPR Spectrometer

High-T_c superconductors due to their higher operating temperatures, 2-dimensional (2D) layered structure and very short coherence length are known to show some interesting properties especially magnetic field dependent microwave (MW) absorption effects at very low magnetic fields of the order of zero gauss [1,2] as encountered in energy /absorption studies at MW frequencies. One prominent example of this is the appearance of very strong non-resonant microwave absorption (NRMA) signal centered around zero magnetic field in the superconducting state at sligtly below T_c in cuprate-based HTSC: YBCO, reported by Bhat et al., 1987 [3] using conventional electron spin resonance (ESR) spectrometer. This was followed by reports on other cuprate based HTSC [4-10] and also on a different variety of superconductors like borocarbides [11], oxyflorides [12] alkali fullerides, granular conventional low-Tc type I [Pb, Al, Sn, In etc.]/type II [Nb, Nb_3Sn, $Nb_3Ge/PbMoS_6O_8$.] [13-15, 17] MgB_2 [16] including newly discovered iron pniticide [18,19]. Before coming to the actual problem, what follows is a brief introduction of the NRMA studies done before the arrival of HTSC.

2.2.1 NRMA Studies

It is interesting to note that the NRMA response using ESR technique was reported for the first time in 1970s by Indovina et al., [4,6] in the case of granular thin films of conventional type I superconductor: Pb. Similar results were then reported in other type I superconductors: Sn [4] and Al [6] at magnetic fields varying from few hundred gauss to many thousand gauss. These reports strongly pointed out that the NRMA signal appears only if Josephson junctions (JJs) are present and their thicknesses (t) are $\geq \xi$ and it does not appear in JJs free superconductors and/or superconductors having very thin JJs. These JJs are the non-superconducting regions separating (i) microscopic metal superconducting grains and/or (ii) superconducting regions within the grain. The main mechanism of MW power absorption was assigned to resistance of JJs [2,6] and/or viscous motion of fluxons penetrated at JJs. It is to be pointed out that in both these models, JJs of intergranular type (here after called as JJ-inter) are considered. Despite these reports on the observation of NRMA revealing an important and direct information related to manifestation of JJs-inter in granular conventional superconductors which cannot be rendered by resistivity and specific heat measurements, not much literature on NRMA studies was available at that time.

It was not until the advent of HTSC which are intrinsically granular in nature and showed a very strong NRMA signal at nearly zero magnetic field, that NRMA became a valuable, informative and indispensable tool for examining all kinds of granular superconductors existing till today from conventional (both type I and type II) to recently discovered iron pniticide etc. particularly for the detection of variety and behavior of JJs and to know the mechanism of MW absorption.

Further, to explain the origin of NRMA signal in HTSC, Portis et al., [4] extended the previous models for conventional granular superconductors in which JJ-inter play the dominant role. This was done by including the contribution from intragranular JJs (JJ-intra) also. Unlike in the granular conventional superconductors where the effect of JJ-intra will be suppressed due to large ξ, in HTSC due to very short ξ, the effect of JJ-intra can be easily observed. Although these models considered contribution from both the JJs (JJ-inter and JJ-intra), however, they associated to different mechanism of absorption. That is, Portis et al.,[4] associated NRMA to damped fluxon (intergranular fluxons at JJ-inter / intragranular fluxons at JJs-intra) motion, whereas Dulcic et al., [4,5] associated to JJ-inter and JJ-intra resistance to the induced boundary currents (Josephson currents). Further, it was pointed out by Portis et al.,[4] that "although we associate the microwave absorption with damped fluxon motion, it may be equivalent to associate the absorption with Josephson currents as others have done".

The continuous growth in this field of NRMA studies, along with the extreme sensitivity and expedition of the NRMA technique apart from its ability to detect the phase transition to the superconducting state has opened a new window: (i) to unambiguously discover/detect new superconducting phases present even in quantities as low as of the order of sub micrograms, (ii) to distinguish multiple superconducting phases in a single matrix, (iii) to tell something about the quality of the superconductor, (iv) to study a new type of device for example: a single chip comprising of a combination of insulating, semiconducting, and superconducting layers, (v) to study the phase diagram of vortex matter through temperature dependent NRMA signal amplitude and to (vi) reveal important information on the anomalous nature of magnetic hysteresis.

NRMA studies provide new insights to both the fundamental and technological aspects of HTSC. There are two very important observed features which need further elucidation as their origins are still not very clear, though there is a consensus on the origin of NRMA. Firstly, how could the amplitude of the NRMA signal which is a manifestation of the JJ-inter / JJ-intra with markedly different temperature dependences originate in such JJs? Secondly, how could the anomalous nature of NRMA hysteresis in contrast to the normal nature of DC magnetic hysteresis under similar conditions of temperature and magnetic field be generally observed? A critical analysis of the existing understanding to explain these observed features reveals that the full explanation of these anomalies are still far from clear understanding and thus needs modifications.

Recently these two aspects have been taken seriously and analysed in a different perspective, i.e. (i) by including the role of electromagnetic interactions (EMI) for explaining the reason for undulatory temperature dependence of the NRMA signal amplitude, and (ii) by giving a special reference to energy stabilized Josephson fluxons (ESJ) for explaining the anomalous magnetic hysteresis observed using NRMA. Hence some sentiment of this thesis is to further explicate these two problems and the importance of NRMA technique in understanding their origin in a broader and deeper perspective with inclusion of studies made on recently discovered YBCO [4,5]. The first problem has been analyzed in a more generalized way by including some more data (i.e. temperature dependence under magnetic field) so that the confusion related to the different explanations for the origin of the temperature dependence of the NRMA signal can be minimized. Similarly, the second problem based on the existing status of NRMA hysteresis and their comparison with DC magnetization hysteresis, this YBCO discovered is a superconductor material and is for our interest to look at superconductor origin.

It ia a fact that high-T_c superconducting cuprates are extremely complicated and so awkward to deal with from the theoretical point of view [18]. In order to build more realistic model, having more experimental data would be helpful.

2.3 Magnetic Properties of Superconductors

This section is dedicated in elaborating some of the relevant magnetic parameters and properties in relation to electromagnetic dynamics of superconductors.

2.3.1 Critical Fields

Fluxon dynamics in a supercondutor is a crucial phenomenon which needs to be adequately elucidated for better understanding of its magnetization and magnetic field temperature phase. The behavior of both conventional and unconventional superconductors in an applied magnetic field is well presented in three segments namely; Meisser phase, mixed/vortex state and the normal state. Using these distinct segments, superconducting materials can be characterized as either Type I or type II supercondutor [20].

Figure 10(a) and Figure 10 (b), show an H-T phase diagram and magnetization curve

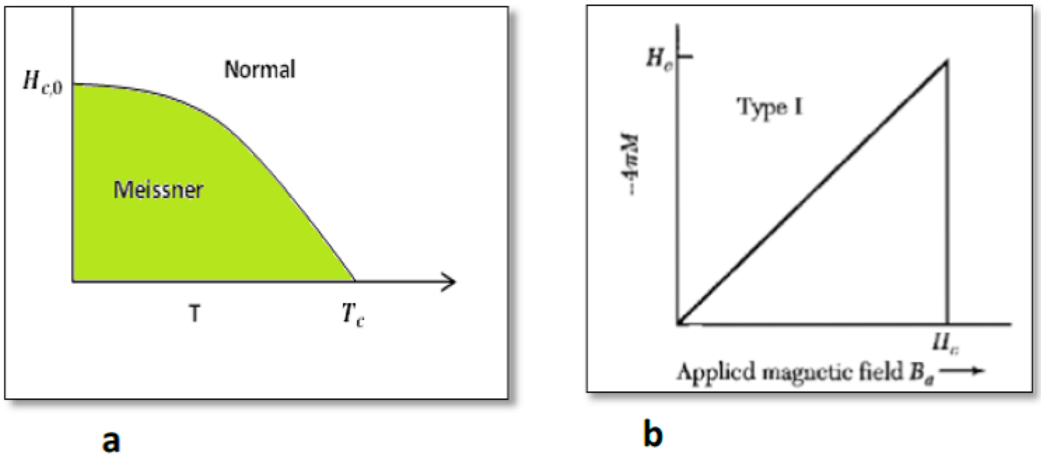

Figure 10: (a) H-T phase diagram of type I superconductor and (b) Magnetization of long solid cylinder I superconductor[21].

of a type I superconductor. When the magnetic field H is turned on, definite amount of energy is used to create the magnetic field of the screening currents that cancels the field in the interior of the superconductor [19 , 20]. This process is called Meissner effect. Once the applied field exceeds a thermodynamic critical field, $H_{c(T)}$, the superconductivity state is damaged and the material regresses to the normal state where the field penetrates without restrictions.

The thermodynamic critical field is related to the free energy difference between the normal and superconducting state in zero field. As shown in equation (2.2),H_c is determined by equating the energy $H^2/8\pi$ per unit volume associated with holding the field out against magnetic pressure with the difference in Helmoltz free energy [22]

$$\mu_0 H_c^2(T)/2 = f_n(T) - f_s(T) \tag{2.2}$$

where f_n and f_s are normal state and superconducting state free energy.

Meissner state provides enormous information in trying to understand the fundamental principles and nature of superconductivity in materials. For instance, lower critical field can be measured [23] and also the extraction of fundamental parameters such as coherence length and penetration depth.

Type II superconductors have got two critical fields namely lower critical field $\mathrm{H}_1(T)$ and upper critical field $\mathrm{H}_{c2}(T)$ as shown in Figure 11 (a). Figure 11 (b), shows magnetization curve of a long solid cylinder of type II superconductor. When magnetic field applied to a superconductor is less than $\mathrm{H}_1(T)$, there is no flux penetration and the sample behaves as type I superconductor. However, when magnetic field exceeds $\mathrm{H}_{c2}(T)$, the sample turns to normal state.

There is a distinctive state called the mixed or vortex state which occurs when the applied field is between $\mathrm{H}_1(T)$ and $\mathrm{H}_{c2}(T)$ which allows partial penetration of flux and the material remains in a superconducting state [24]. At this state, $\mathrm{B} \neq 0$ as the material is being threaded by flux lines. It is an exciting state because it provides crucial information such as irreversibility line and upper magnetic field which determines whether the material has the possibility of a potential application.

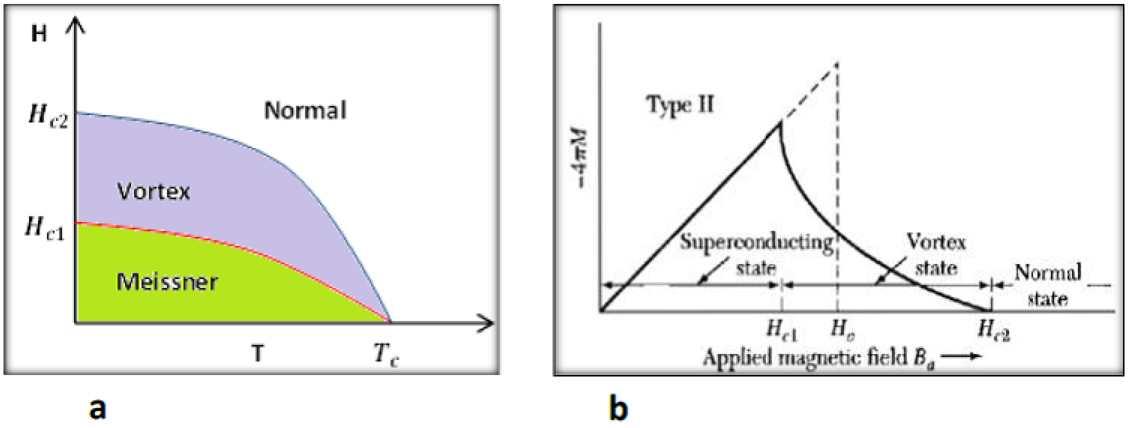

Figure 11: (a) HT sketch for type II superconductor and (b) Magnetization of a long solid cylinder type II superconductor. Figure 11 (b) was reprinted from [21].

2.3.2 Fluxon Quantization

A brief discusion of flux quantization in a superconductor is given by Fossheim and Sudbo [26]. In a ceramic HTSC, magnetic field enters in form of fluxons [25]. It then follows that some region of the superconductor is in the normal state. Given the order parameter of a superconductor is

$$\Psi = |\Psi|\mathtt{e}^{\mathtt{i}\varphi} \tag{2.3}$$

the line intergral of gradient $\nabla\varphi$ around a closed contour encircling the normal domain has to be given by $2\pi N$, where N∈Z.

it is assumed that the order parameter must be single valued at any given point and

$$\int_{1}^{2} \mathtt{dl}\varphi = \varphi_1 - \varphi_2 \tag{2.4}$$

is independent of the path connecting the start and end point, we have [25].

$$\oint \mathtt{dl}.\nabla\varphi = 2\pi\mathtt{N} \tag{2.5}$$

The gauge invariant phase of the order parameter now has the gradient

$$\nabla\varphi\mathtt{GI}(\mathtt{r}) = \nabla\varphi(\mathtt{r}) - \frac{\mathtt{2e}}{\hbar}\mathtt{A} \tag{2.6}$$

where A is a vector potential coupling the magnetic field to the superconducting order parameter and e is the charge of a Cooper pair. Using the modification

$2e/\hbar = 2\pi/(h/2e) = 2\pi\pi/\phi_0$ and subjecting the gauge-invariant order parameter to the constraint as shown

$$\oint \mathtt{dl}\nabla\varphi\mathtt{GI} = 2\pi\mathtt{N} \tag{2.7}$$

as the single-valuedness must still hold. Hence, we obtain [6]

$$2\pi/\varPhi_0 \oint \mathtt{dl} \times \mathtt{A} = 2\pi\mathtt{N} \tag{2.8}$$

Applying stokes theorem we obtain

$$\int_{\mathtt{S}} \mathtt{dl} \times \varphi = \int\int_{\mathtt{c}} \mathtt{ds}\nabla \times \mathtt{A} = \int\int_{\mathtt{S}} \mathtt{dSB} \equiv \mathtt{N}\Phi_0 \tag{2.9}$$

where $\vec{B} = \vec{\nabla} \times \vec{A}$ and Φ is the magnetic flux through the surface S enclosed by the contour C [22]. This flux is thus seen to be quantized in units of $\Phi_0 \approx 2.07 \times 10^{-15}$Wb.

2.3.3 Josephson Junction and Josephson Effect

A Josephson junction is composed of two superconducting layers coupled by a weaklink. The weaklink can consist of a thin insulating barrier (S-I-S), a short section of nonsuperconducting metal (S-N-S), or a physical constriction that weakens the superconductivity at the point of contact (S-C-S). The Josephson effect is the phenomenon that the current can tunnel through the junction (or weak link) without any voltage applied [27].

When a superconductor is cooled below its transition temperature, the electrons condense forming a macroscopic quantum state. In this case, all the electrons in the superconducting condensate are defined by a single complex wavefunction given as

$$\psi = |\varphi|\mathtt{e}^{\mathtt{i}\varphi} \tag{2.10}$$

where $|\psi|$ is the magnitude of superconducting order parameter which is a measure of the density of superconducting electrons, whereas φ is the phase connected to the flow of supercurrents [26]. As soon as two superconductors are weakly coupled together as shown in Figure 12, their superconducting order parameters overlap and consequently electrons flow. The junction formed is called Josephson junction and the nature of coupling determines the amount of current through the junction. With no applied potential in this junction, a DC phase-dependent current flows between the two superconductors

$$\mathtt{I} = \mathtt{I}_{\mathtt{c}}\mathtt{sin}\varphi \tag{2.11}$$

where I_c is the critical current (the maximum current that a junction can accommodate before dissipation occurs).

In the event that a voltage is applied across the junction, the phase varies according to equation 2.10. It results to an AC Josephson effect

$$\mathtt{d}\varphi/\mathtt{dt} = \mathtt{eV}/\hbar \tag{2.12}$$

The amplitude of the DC Josephson current in equation 2.11 depends on temperature. Ambegaokar and Baratoff derived an equation of the critical current for a tunnelling junction with conventional superconductors as from Ref. [27].

$$\mathtt{I_c(T)} = \frac{\pi\Delta(\mathtt{T})}{\mathtt{2eR_n}}\mathtt{tanh}\frac{\Delta(\mathtt{T})}{\mathtt{2K_B T}} \tag{2.13}$$

Here R$_n$ is the junction resistance in the normal state and $\Delta(T)$is the energy gap. The Josephson current is maximal at T=0

$$\mathtt{I_c} = \frac{\pi\Delta(0)}{\mathtt{2eR_n}} \tag{2.14}$$

Once I>I$_c$, a current of normal electrons will flow through the junction in addition to the supercurrent. This results to the formation of resistively shunted Josephson junction (RSJ). The RSJ is considered as a circuit made of a normal resistance and a capacitor connected parallel to each other. The total current of this circuit will be a sum of the normal current, V/R, current through capacitor, CdV/dt, and supercurrent $\mathrm{I}_s = I_c \sin\varphi$ [27] and given by

$$\mathtt{I} = \mathtt{I_c sin}\varphi + \mathtt{V/R} + \mathtt{CdV/dt} \tag{2.15}$$

with some mathematical manipulation, equation 2.15 gives

$$\mathtt{I/I_c} = \mathtt{sin}\varphi + \mathtt{d}\phi/\mathtt{d}\tau + \beta_\mathtt{c}\mathtt{d}^2\phi/\mathtt{d}\tau^2 \tag{2.16}$$

Here β_c= $2\pi I_c$ R$^2C/\Phi_0$ is Stewart-McCumber parameter.

The current-voltage, I-V characteristics can be described is Stewart-McCumber parameter.

If $\beta_c << 1$, the I-V dependence is non-hysteretic (nondissipative) and is given by V(I)=R($I_s^2 - I_c^2)^{1/2}$ while when $\beta_c >> 1$ the junction becomes hysteretic (dissipative) [28].

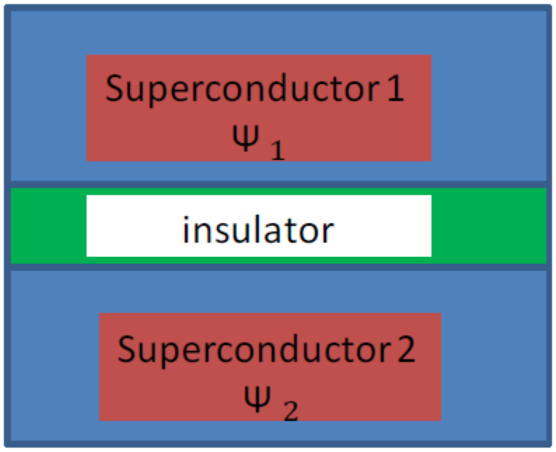

Figure 12: Schematic Josephson junction showing two superconductors separated by an insulating layer [29].

Any form of weaklink in a superconductor where the critical current is significantly supressed results to Josephson junction. They include SIS tunnelling, SNS sandwich, microbridge formed by constriction, point contact junction and a small drop on a superconducting wire [27]. In ceramic superconductors, inter-granular and intra-granular weak links form Josephson junctions. In fact in a layered superconductor, Josephson junction may be formed within a unit cell as a result of sufficiently low inter-layer coupling [30].

Josephson effect has been employed in Josephson junction-related applications such as SQUIDs and QUBITs. Its milestone application is the intrinsic Josephson junction (iJJ). It employs the Josephson effect in which direct current voltage is naturally converted into a high frequency electric current. The ijj shows potential in acting as a source of subterahertz and terahertz frequencies hence closing the famous Terahertz gap [25].

2.4 Josephson Coupling Energy

The idea of high-T$_c$ ceramics superconductors being anisotropic in nature implies that Josephson junctions parameters have different values. One of these parameters is Josephson coupling energy E$_j$. This energy is associated with a macroscopic varriable φ i.e. the phase difference between two superconductors, which permits the transport of Cooper pairs between superconducting electrodes [31]. By considering two superconducting electrodes (grains) below T$_c$, the Josephson coupling energy is expressed [32].

$$\mathtt{E_J(T)} = \frac{\mathtt{hI_c}}{\mathtt{2e}} = \frac{\mathtt{h}}{\mathtt{8e^2R_n}}\mathtt{\Delta(T)tanh}\frac{\mathtt{\Delta(T)}}{\mathtt{2K_BT)}} \tag{2.17}$$

where I$_c$ is the Josephson critical current between grains, R$_n$ is the normal state resistance and $\triangle(T)$ is the BCS energy gap of the grains. Phase coherence exists at very low temperature and magnetic field which results to maximum Josephson junction current. In this state the coupling is enhanced and consequently E$_J$ is high and the junction acts as bulk.

2.5 Short Coherence Length and Penetration Depth

Coherence length and London penetration depth are the two most fundamental length scales of superconductivity. Coherence length, ξ , is the minimum length scale over which the superconducting order parameter can vary significantly. It is responsible for the weakening of the pair potential at the surface and interface and the appearance of the inter-grain Josephson junctions in ceramics or the twin boundary junctions in single crystals [33]. This results in glassy behaviour observed in ceramic samples as well as single crystals. London penetration depth can be evaluated from the exponential decay of magnetic field as

$$\mathtt{B(x)} = \mathtt{B_0e^{-x/\lambda_L}} \tag{2.18}$$

Here $\lambda_L^2 = m/\mu_0 n_s e^2$ is the London penetration depth. It shows the distance over which boundary currents (shielding currents) circulate to nullify the applied external field. It is controlled by the superfluid density n. The london penetration depth has both fundamental and technological relevance. For instance, the d-wave pairing symmetry in cuprates [34] and the two gap nature in MgB_2 [35] was revealed from temperature dependence of the penetration depth. Again, it affects the inductance of a superconducting microstrip in technological field [36]

From the two lengths, Ginzburg Landau parameter k which is the ratio of London penetration depth and coherence length (λ/ξ) is obtained. This k is significant since it is a criterion that describes the two types of superconductors. When $k < 1\sqrt{2}$, the material is referred to as type I superconductor and total magnetic flux is realised. Whereas if $k > 1\sqrt{2}$, it defines a type II superconductor which allows partial penetration of magnetic flux when the applied field is greater than H_{c1}. The two lengths can as well be extracted from the lower critical field equaction 2.18 and upper critical field equaction 2.19 [37]:

$$\mathtt{H_{c1}} = \frac{\Phi_0}{(4\pi\lambda^2)}\mathtt{ln}\frac{\lambda}{\xi}, \tag{2.19}$$

and

$$\mathtt{H_{c2}} = \frac{\Phi_0}{2\pi\xi^2} \tag{2.20}$$

Here Φ_0= h/ 2e is the quantum of flux. Typical magnetic penetration depth $\lambda(0)$=170 nm and coherence lenght ξ_{ab}=5.7 nm in MgB_2 have been obtained.

2.6 Flux Flow and Flux Creep

Magnetic fields enter the HTSC ceramic material in form of fluxons at fields greater than the lower critical field of a Josephson junction. As a result, flux gets pinned at pinning sites in a superconductor. The interaction between pinned magnetic field lines and the current which is induced by electric field gives Lorentz force [38].

At a critical point defined as $F_p = F_L = J \times B$ (that is, the pinning potential is equal to Lorentz force), where J and B are current density and magnetic field respectively, the field lines are fully pinned. When the current gets large enough, Lorentz force is strong and exceeds pinning potential, the fluxon velocity v is limited by the viscous drag exerted by the surrounding medium, through the force balance $\Phi_0 J = nv$ giving [26]:

$$\nu = \frac{\Phi_0 \mathtt{J}}{\eta}. \tag{2.21}$$

Multiplying ν by B, electric field E can be expressed as

$$\mathtt{E} = \mathtt{B}\nu = \frac{\mathtt{B}\eta}{\Phi_0 \mathtt{J}} = \rho_{\mathtt{ff}} \mathtt{J}, \tag{2.22}$$

$\rho_{ff} = \frac{B\Phi_0}{\eta}$ is the flux flow resistivity. This can also be written as [39].

$$\rho_{\mathtt{ff}} = \rho_{\mathtt{n}} \mathtt{B}/\mathtt{B}_{\mathtt{c2}} = \mathtt{n}\Phi_0/\mathtt{C}^{\mathtt{n}}\eta, \tag{2.23}$$

where n=B/Φ_0, η, ρ_n and B$_{c2}$ are the fluxon number density, coefficient of the viscous drag, normal-state resistivity and the upper critical field respectively.

Apart from Lorentz force, thermal energy (kT) may induce hopping of pinned fluxons from their pinned positions. The depinned fluxons will move or creep in order to relax the critical state field gradient [26]. The hopping rate from pin site is determined by Boltzmann factor

$$\mathtt{R} = \nu_0 \mathtt{e}^{-\mathtt{U}/\mathtt{kT}}, \tag{2.24}$$

where u is the height of the activation barrier and ν_0 is some microscopic frequency with which fluxons try to escape the pinning site.

2.7 Flux Pinning

Flux flow and flux creep that can be experienced in a superconductor has been discussed in the previous section. This results in flux flow resistivity hence the J$_c$ is suppressed. This sounds an anathema to HTSC-related applications. One way of increasing J$_c$ is by enhancing pinning ability of a superconductor [40]. Although ceramic samples can pin vortices naturally through imperfections such as grain boundaries, twin boundaries, impurities (superconducting and non- superconducting), defects and voids [41, 42], artificially engineered defects are needed to add more pinning sites to a sample.

There are a variety of ways to artificially increase pinning centers and they include; addition of second phase [32], compositionally modulated superlattice [33], magnetic particles [34] columnar defects and ion irradiation [35]. At the pinning centers, superconductivity is suppressed and the normal core finds it energetically favourable to reside there [36]. The maximum pinning energy per unit length in this case is the superconducting condensation energy in the volume of the vortex, given by equation 2.25 [37].

$$\mathtt{U_{cp}} \sim (\mathtt{H_c^2}/8\pi)\pi\xi^2 = [\Phi_0/8\pi\lambda(\mathtt{T})]^2 \tag{2.25}$$

Here $\mathrm{H}_c, \xi, \Phi_0$, and $\lambda(T)$ are the thermodynamic critical field, the coherence length, the flux quantum, and the temperature dependent London penetration depth respectively. The pinning energy drops as $T - T_c$ due to increase of λ as $\lambda^2(0)/\lambda^2(T) \sim (1 - T/T_c)$ [27]. The extent of pinning in a superconductor material defines the kind of surface resistance as shown by Coffey and Clem as [38]. They established that at strong pinning regime where penetration depth is greater than the flow penetration, the surface resistance is given by

$$\mathtt{R_s} = (\eta^2\omega^2/\mathtt{k}^{3/2})\sqrt{\Phi_0\mathtt{B}/\mu}. \tag{2.26}$$

However, when there is a weak pinning coming as a result of creep penetration depth being greater than the flow depth the surface resistance is given by

$$\mathtt{R_s} = \sqrt{\mathtt{B}\Phi_0/2\eta\mu\mathtt{k}} \tag{2.27}$$

where μ is the permeability, ω the microwave frequency, k the pinning constant, η the viscosity and Φ_0 the quantum of flux.

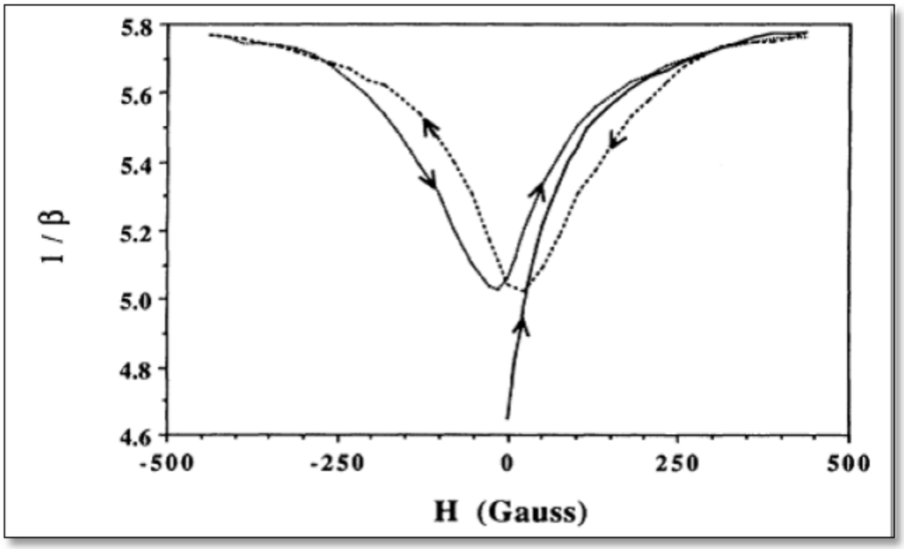

Figure 13: Signal depicting hysteresis measured on ZFC $YBa_2Cu_3O_7$ bulk samples at 78 K [47].

In low magnetic field radio/microwave absorption of HTSC, the manifestation of pinning is depicted by the hysteresis (see Figure 13). The hysteresis phenomenon can be explained pertinently by a two-level critical state model [39] which is covered in non-resonant radio/magnetic features section.

2.8 Penetration Depth of Josephson Junction

In a superconductor without any weak link, magnetic field penetrates into the bulk of the superconductor to a depth equal to the London penetration depth, λ_L. However, in a superconductor such as high-T_c oxides ceramic pellet, the magnetic field penetrates first into the Josephson junctions whose penetration depth is much larger than London penetration depth [37].

In response to a weak magnetic field, $H_0 << \Phi_0/(2\pi\lambda_j d)$, the junction will set up screening currents given by equation 2.25 which corresponds to that in a bulk sample to stop field penetration.

$$\mathtt{H}(\mathtt{x}) = \mathtt{H}_0\mathtt{e}^{-\mathtt{x}/\lambda_\mathtt{j}} \tag{2.28}$$

The quantity λ_j is referred to as the Josephson penetration depth and it epitomises the depth of magnetic field penetration into the Josephson junction. It has dimensions of length and can be expressed as equation 2.29 [40]. It offers essential information in regards to solotons dynamics in long Josephson junctions (long Josephson junctions are junctions with one dimension larger that Josephson penetration depth [41]

$$\lambda_\mathtt{j} = \left[\frac{\Phi_0}{\pi\mu_0\mathtt{j}_\mathtt{c}\mathtt{d}}\right]^{\frac{1}{2}} \tag{2.29}$$

where $\mu = 4\pi \times 10^{-7} Hm^{-1}, \Phi_0 = 2.07 \times 10^{-15}\mathtt{Wb}$, j_c is the critical current density through the junction given in Am^{-2} and d is expressed in m. For instance, niobium material has a value of $\sim 21\mu$ m.

2.9 Lower Critical Field of Josephson Junction

The expression of free energy of an individual Josephson vortex in an infinite junction is given as

$$W_0 = 4\Phi_0 j_c \lambda_j / \pi C \tag{2.30}$$

And when this junction is subjected to an external magnetic field H_0, the Gibbs free energy of a Josephson vortex can be represented as

$$G_0 = W_0 - \Phi_0 H_0 / 4\pi \tag{2.31}$$

When the applied external magnetic field is adequately weak, the Gibbs energy $\mathrm{G}_0 > 0$ and the Josephson vortex will not enter the junction as it is energetically unfavourable. However, when the external field is equal to H_{cj1} Gibbs energy equals to zero and the vortex penetrates the junction. The H_{cj1} is the lower critical field of Josephson junction given as [48]

$$H_{cj1} = 2\Phi_0/\pi^2\lambda_j d. \tag{2.32}$$

2.10 Surface Impedance

Surface impedance measurement is one of the most indispensable ways of characterising a superconductor material. Having the information of the complex surface impedance of a superconductor $Z_s(\omega)$, its interation with electromagnetic wave at frequency wave at freqeucy ω can be determine [51]. For a superconductor occupying the half space, Z$\geq$ 0 the microwave surface impedance is a ratio of electric field and magnetic field on the surface of a superconductor which is defined as

$$Z_s = R_s + iX_s = \frac{E_t(z=0)}{\int_0^\infty J_s(z)dz} \tag{2.33}$$

where $E_t(z=0)$ is the tangential electric field at the plane boundary of z=0, and J_s is the surface current density flowing parallel to the plane boundary [43,44]. The surface impedance has a relationship with a complex wave number (β) of a plane wave penetrating into the metal given as [45]

$$\beta = \frac{\omega\mu_0}{Z_s} \tag{2.34}$$

In Equation (2.33), the real part, R_s, and the imaginary part, X_s, are called the surface resistance and surface reactance, respectively

$$R_s = \frac{1}{2\omega^2\mu_0^2\sigma_n\chi_n\lambda_L^3} \tag{2.35}$$

$$X_s = \omega\mu_0\lambda_L \tag{2.36}$$

where μ_0 is the free-space permeability, ω is the angular frequency of the microwave radiation, χ_n is the fraction of the normal fluid, σ_n is normal-state conductivity, and λ_L is the temperature-dependent London penetration depth [44].

According to the two-fluid model the expression for σ_n and λ_n are given as [45]

$$\sigma_{\mathtt{n}}(\mathtt{T}) = 1 - (\lambda_0^2/\lambda_{\mathtt{L}}^2) \tag{2.37}$$

$$\lambda_{\mathtt{L}}(\mathtt{T}) = \frac{\lambda_0}{\sqrt{1-(\mathtt{T}/\mathtt{T_c})^4}} \tag{2.38}$$

From equation 2.37, important information on surface resistance can be obtained which is crucial in applications of superconductors in passive microwave devices. Also, fundamental parameters such as London penetration depth can be extracted from equation 2.38. Furthermore, by knowing the surface resistance of a superconductor, microwave power dissipated can be expressed as

$$\mathtt{P} = \frac{\mathtt{RH}^2}{2} \tag{2.39}$$

This expression is invoked when dealing with low field microwave absorption measurement. Since the microwave power absorption obtained is in derivative form, the derivative of equation 2.39 is used [54].

$$\mathtt{dp/dH} = \mathtt{d/dH(RH^2/2)} \tag{2.40}$$

2.11 Non-resonant Radio/Microwave Absorption Features

Non-resonant microwave absorption has shown numerous features worthy to mention. This section briefly highlights some of these features.

2.11.1 First, Second and Third Peak

Non-resonant microwave absorption sharp line in HTSC superconductors have shown many complicated but most appealing features. Among these features is the appearance of 2^{nd} and 3^{rd} in Bi2212 superconductor. Before we discuss the second and third peak , it is paramount to mention of the first peak (central narrow signal) that occurs near zero magnetic fields [47,48]. This signal occurs as a result of microwave loss emanating from Josephson junction in the inter granular region [50,51]. The peak can be explained by Dulic model [5,6] where the critical current of Josephson junction is reduced, as the magnetic field easily enters the sample via inter granular weak links.

The 2^{nd} peak has been explored by [46, 52-54]. Rastogi et al., [57] attributed this 2^{nd} peak to the from intrinsic Josephson coupling between Cu_2O layers. While Masiakowski et al., [58] suggested that it originates from second phase in the sample. Methodical studies by Srinivasu et al., [59] show that this peak not only depends on mutual orientations of the crystal ab plane, the DC field and the magnetic field but also it depends on microwave power. Hence the two peaks (2^{nd} and 3^{rd}) attribute to microwave loss resulting from decoherence and detruction of the otherwise microwave power induced phase locking of junctions [60].

2.11.2 Absorption Spectral Lines

Equally spaced, narrow anisotropic absorption lines which depend on temparature, field modulation and microwave power were observed in single crystals of YBCO superconductors [61-64]. Blazey et al., [61,62] show that the lines can be fitted by an expression

$$\mathtt{Hcos}\theta = \pm(\mathtt{p}+1/2)\Delta\mathtt{H} \tag{2.41}$$

with p being an integer. They further alluded that the lines were associated with the motion of fluxons into the regular arrays of twin planes. There spectral lines are elucidated by Owens to be emanating from phase jumps in a superconducting loop [54, 56]. It is argued that because flux is quantized in a superconducting loop, as the applied field increases, phase jumps are experienced. The phase jumps occur when the field enclosed becomes an intergral multiple of the unit quantum of flux. These flux jumps occur in a very short time and therefore produce voltage pulses given by

$$V(t) = -(h/2e)d\theta/dt. \tag{2.42}$$

When this occurs the critical current of the superconductor is exceeded and the normal current flows which can absorb microwave energy.

2.11.3 Magnetic Shielding Effect

Magnetic shielding effect is one of the most exploited characteristic when identifying a material sample in the fabrication of low field microwave-related devices. This effect was explored in detail on pure YBCO thin film superconductor and silver doped YBCO thin film superconductor at both small and high field modulation fields by Srinivasu et al., [64]. They found that Ag-doped YBCO thin films showed better shielding properties compared to undoped YBCO resulting from good grain alignment and grain enlargement.

2.11.4 Phase Reversal

Phase reversal is the change over from a maximum at zero magnetic field and the decrease with the increasing field to aminimum at zero field and the increase field [65]. This anomalous feature has been observed in different forms of samples [66]. In powder sample of YBCO superconductor, the signal evolves with RF power whereby at lower RF power, the RF absorption has a minimum at zero DC-field, H$_{DC}$, and increases monotonicaly with increaseing H$_{DC}$. At higher RF power level the phase of the DC field is reversed and at higher H$_w$, this anomaly has been interpreted to be from a non linier response of weakly connected superconducting rings disrtibuted in the power sample [66]. On the other hand, temperature dependent anomalous absorption has been revealed and a model of an effective medium theory which treats a sample as a percolating network consisting of superconducting regions separated by normal metallic regions is invoked to explain this feature [66].

2.11.5 Magnetic Hysteresis

Anomalous hysteresis where the forward curve lies above the return curve when magnetic field is swept forward and backward has been observed in HTSC [59,60]. Kim et al., [37] studied BSCCO superconductor and attributed it to absorption response in different types of weak links forming Josephson junctions. They used a combination of Portis and Dulcic models to systematically calculate the observed signal [37].

Magnetization measurement on the same superconductor material has been done and the anomaly interpreted as occuring as a result of fluctuation coming from layered structure and high anisotrophy [59]. Padam et al., [68] have also argued that the generation and detection of energy stabilized Josephson junction fluxons may be the cause of the anomaly. Ji et al., [38] proposed a two level critical state model to elucidate the anomalous hysteresis observed. They pointed out that in granular materials; intergrain and intragrain are distinct with different critical current density values. A large critical current density, J_{cg} inside the grains and a much weaker one ,J_{cj} reflecting the intergranular Josephson coupling.

The model further assumes that on a microscopic level, the flux density average over a scale of many grains should have a gradient determined by the macroscopically flowing intergranular critical current density J_{cj}. On the local level within single grains, a critical state established with flux density gradient determined by intergranular critical current density J_{cg}. Hence , the flux density in the grain boundaries influence this local critical state by supplying the effective external field.

Again, they argued that there are two types of fluxons namely grain-pinned which are pinned by pinning centers within grains and grain boundary free-fluxons which pass through weakly superconducting regions. It is these free fluxons which are responsible for electromagnetic loss.

2.11.6 Surface Barrier Effect

Surface barrier effect arises as a results of the interaction of a vortex with its mirror image and shielding currents on the surface. It is characterized by zero magnecteriezation in the reverse sweepof the external magnetic field and penetration H_p field higher than H_{c1} as reported by Rastogi et al., [69]. This effect was observed in superconducting thin films of YBCO.

A vertical hysteresis on the NRMA signal which had unusual temperature dependence i.e it increased with increase in temperature up to Tc while the signal intensity decreased was observed. It was attributed result from the difference in magnetization in forward and reverse field sweeps which agrees with one of surface barrier characteristics [61].

2.11.7 Oxygen Deficiency

Modulated microwave absorption studies on YBCO superconductor by Puri et al., [70] showed periodic oscillations with two different frequencies which they designate as signal type A and type B in their work. They interpreted the oscillations to come from at least two different kinds of microwave sensitive Josephson junctions. Further they observed that both signals have different dependencies on microwave power, temperature and field modulation. They suggested that oxygen deficiency in the YBCO single crystals acts like Josephson junctions which brings about the low field microwave absorption observed.

2.11.8 Paramagnetic Meissner Effect

Paramagnetic Meissner effect (PME) often known as Wohlleben effect is an abnormal paramagentic response of a given superconducting sample of HTSC to an application of weak magnetic fields [62, 63]. Samples with this effects have shown an anomolous microwave absorption that has a local maximum absorption at zero applied magnetic field instead of a minimum absorption [67,68].

Bhat et al.,[65] studies indicate that this effect comes as a result of the presence of π

junctions. Srinivasu et.al., [66] points that the effect is extrinsic and is associated with certain mesoscopic defect structures that favour formation of spontaneous currents and must be of order $10^5 - 10^6$ A/cm^2. Consequently, they concluded that this large current is from the π junction in intragrain rather than intergrain. Also, they observed that this effect is anistropic in nature. In the case of aligned powder, it is strongest for magnetic fields parallel to the c-axes.

2.11.9 AC Loss in Superconducting State

Chockalingam et al., [74] observed a unique behaviour on radio frequency loss measurement of BSCCO material. They noted a larger AC loss in the superconducting state than in the normal state. They also observed two distinct peaks namely peak A and peak B as indicated in their work. They noted a decrease in amplitude of peak A with increasing magnetic field. However, the amplitude increased as the orientation of sample changed from 0^o to 90^o. They explained this unusual AC loss in superconducting state in terms of repetitive coupling and decoupling of Josephson junction (see model of coupled and decoupled Josephson junction). Peak A is explained in terms of critical current density corresponding to the coupling energy and peak B occurs as a result of Lorentz-force-driven motion of vortices [67, 68].

2.12 RF and Microwave Loss Mechanisms

In a superconductor , an application of DC current of a constant value implies no power is lost (zero resistance). However, when AC current is applied, a resisitance

$$(R = \frac{V_{rms}^2}{R}) \tag{2.43}$$

A lot of experimentalist and theorists have put forth possible explanations for the origin of this AC loss and they include:

- flux damped motion [69],
- loss due to shaking of vortices [70],

- loss in the intergranular Josephson junction [71],
- vortex normal state [2, 71],
- and flux flow [71].

There is no single model which explains all the observations in low microwave absorption and as a result we have picked the most appropriate that fit our data.

2.12.1 Portis Model

In HTSC superconductor, the misalignment of superconductor grains, the availability of the second phase, voids and cracks to suppression of the order parameter as mentioned in the previous chapter. This leads to weak links behavior in a material which property acts as Josephson junction. When an external magnetic field exceeding the lower critical field of Josephson junction is applied to a sample, fluxons (vortices) start to penetrate. Fluxon velocities within weak Josephson junction are orders of magnitude smaller than in bulk due to lower viscosity in Josephson junction [39]. The spatial variation of microwave field in the Josephson junction induces microwave current which forces fluxons to oscillate according to the equaction of motion [4].

$$\mu d^2x/dt^2 + \eta dx/dt + kx = (1/c)j_i\Phi_0 \tag{2.44}$$

where μ is the mass per unit length, k is a restoring force and $\eta = \Phi_0^2/\ \rho^2$s is the viscosity. ρ the moving fluxon induces a dissipative current that flow through a normal region[13] the sesultant resistance and reactance are given by equactions 2.45 and 2.46, respectively

$$R = X_0[(-1 + (1 + 4f^2B^2/B_0^2)^2)/2]^{1/2} \tag{2.45}$$

$$X = X_0[(1 + (1 + 4f^2B^2/B_0^2)^2)/2]^{1/2} \tag{2.46}$$

with $B_0 = 8\pi\omega\mu\lambda^2\eta/\Phi_0$ which is treated as a measure of the effective field above which flux flow dissipation dominates the loss process and $X_0 = 4\pi\omega\lambda\mu^{2/3}$ is the impedance at zero magnetic field. The symbolls λ, ω, η, and $\varPhi_0$ denote London penetration depth, the microwavefrequecy, the coefficient of viscosity experieced by moving fluxons, the magnetic permeability and the flux respetively. Here B is the field inside the sample and f stands for the fraction of free or weakly pinned fluxons.

2.12.2 Dulcic Model

Dulcic et al., [56] proposed electromagnetic power loss in a superconductor to occur in the intergranular Josephson junction. It is well known that at lower magnetic field the weak links between the superconducting grains provide superconducting paths for the Meissner shielding across the whole sample [72]. Increasing magnetic field reduces the critical current of the junction by a reduction factor,

$$\mathtt{F(H)} = [\mathtt{sin}(\pi\mathtt{H}/\mathtt{H}_0)/(\pi\mathtt{H}/\mathtt{H}_0)] \tag{2.47}$$

Consequently, more magnetic fields penetrate the superconductor and loss occurs. Here H_0 is the magnetic field value for which the junction contains only one quantum of flux, $\varPhi_0$ and is given as [56].

$$\mathtt{H}_0 = \varPhi_0/\mathtt{L}(2\lambda + \mathtt{t}) \tag{2.48}$$

where $\varPhi_0$ =hc/2e is the flux quantum, L is the junction length, λ is the London penetration depth and t, is the junction thickness. By considering Josephson junction as resistively shunted Josephson junction, they argued that transport current of this junction comprises of a boundary current I_0 resulting from magnetic field sweep and which is superimposed on microwave induced current $\mathrm{I}_{mw}\cos\omega_{mw}$ t. Hence, the junction can be represented by a differential equation;

$$\frac{\mathtt{C}\hbar\mathtt{d}^2\Phi}{\mathtt{2edt}^2} + \frac{\hbar\mathtt{d}\Phi}{\mathtt{2Redt}} + \mathtt{I_c sin}\Phi = \mathtt{I}_0 + \mathtt{I}_{\mathtt{m}\omega}\mathtt{cos}(\omega_{\mathtt{m}\omega}\mathtt{t}) \tag{2.49}$$

in the absence of microwave field, the phase would adjust to an equlibrium value ϕ_0 that is $\phi(t) = \phi_0 + \phi_{mw}(t)$. Neglecting the capacitive term, the power absorbed in the junctions takes a simple form

$$P = \frac{1}{2} I^2_{mw} \frac{R}{1+\eta} \tag{2.50}$$

where η is a junction parameter defined by equation

$$\eta = \frac{I_c^2 (cos\phi)^2}{(\hbar\omega_{m\omega}/4\pi e)^2} \tag{2.51}$$

for low field microwave absorption signal shape is given by an expression

$$S_m = \frac{(I^2_{m\omega}R)^2/2}{\hbar\omega_{m\omega}/2eR)^2} \frac{I_c}{(1+\eta)^{3/2}} \times (-\frac{dI_c}{dH} + I_m sin\phi cos\omega_m t) \tag{2.52}$$

where R, ω_{mw}, ω_m,η, and ϕ_0 are junction resistance, the microwave frequency, the magnetic field modulation frequency, the junction coupling parameter and the equilibrium phase difference of the wave function of the superconducting electrons across the junctions. The first term of the equation 2.52, gives the reversible phenomena which is independent of the field sweep direction. The second term is hysteretic (irreversible) and it accounts for the hysteresis since it changes sign when field is reversed ($\phi_0 \longrightarrow -\phi_0$).

2.12.3 Josephson Junction Decoupled Model

Josephson junction decoupling is simply the breaking of a Josephson junction such that it transforms to the normal state by the application of current, magnetic field, or heat energy. In the process, energy is absorbed or released [68]. It is known that the Josephson coupling energy between two superconducting grains is given by

$$E_j(T,H) = \frac{\hbar}{2e} F(T) \left\langle \frac{I_0 sin(\pi\Phi/\Phi_0)}{\pi\Psi\Phi/\Phi_0} \right\rangle \tag{2.53}$$

where Φ and $\Phi_0 = \hbar$ c/2e , are the flux produced by the magnetic field and the flux quantum respectively. F(T) is a factor dependent on temperature which is given by AB theory as

$$\mathtt{F(T)} = \left(\frac{\Delta(\mathtt{T})}{\Delta(\mathtt{0})}\mathtt{tanh}\frac{\Delta(\mathtt{T})}{\mathtt{2K_BT}}\right) \tag{2.54}$$

where $\Delta(T)$ is the temperature dependent gap parameter and $\Delta(0)$ is the gap at $T = 0$. I_0 is the maximum Josephson current given by

$$I_0 = \frac{\pi\Delta(0)}{eR_n}h \tag{2.55}$$

where R_n is the normal state resistance of the junction. when an RF current or an RF field is applied, current is induced. If the induced current is less than the critical current I_c, phase locking is established and the system is governed by, I_0=$\mathrm{I}_c\sin\phi$ and there is no loss under this condition. However, when $I_0 > \mathrm{I}_c$, the junction absorbs energy and the junction is decoupled resulting to losses. So, the total energy loss can be given as $P = 2fNE_j$ where f,N, and E_j are the frequecy of the AC, the total number of Josephson junctions that keep on breaking and forming due to the flow of AC, and the Josephson junction decoupling energy respectively [67].

2.13 Critical Current Density

For many years researchers tried to increase, Jc by incorporating arrays of oxide (for example, Y_2O_3 or $BaZrO_3$) nanoparticles into YBCO films [73]. Such pinning nanostructures can be tuned by varying the shape, size and spatial correlations of oblate or prolate nano-precipitates, self-assembled chains of nanoparticles or nanorods, typically spaced by 4-10 nm and being 2-4 nm in diameter [74, 75]. These artificial pinning centers do enhance Jc, particularly at low field where Jc (77 K, 0 T) $\sim (3 - 5) \times 10^{10} Am^{-2}$ in thin YBCO films can approach 10-20 % of the despairing current density. The maximum super-current density in the absence of vortices above which the Cooper pairs break. Such designer pinning nanostructures also increase Jc at intermediate fields most relevant to magnets. For instance, the high values Jc (0 ,77K) = 2.7 $\times 10^{10} Am^{-2}$ and Jc (5 T,77 K) = $10^9 Am^{-2}$ were observed on YBCO films with Y_2O_3 nano-precipitates [4]. Meanwhile, the first reports about high values of Jc= 4 $\times 10^{10} Am^{-2}$ at 4.2 K [77] and Jc enhanced by incorporating oxide nano-pillars in $BaFe_2As_2$ films [81] indicate that strong pinning in Fe-based superconductors (FBS) can also be achieved.

Unfortunately, strong pinning and high H_{c2} do not automatically make cuprates and FBS good for high-field magnets because their materials features enhance thermal fluctuations of vortices and result in current-blocking grain boundaries. Thermal fluctuations weaken pinning and cause melting of solid vortex structures, giving rise to dissipation well below H_{c2}. As a result, a superconductor can carry currents without dissipation only in a smaller part of its T-H phase diagram (see Figure 14) limited by the so-called irreversibility field $H^*(T)$ at which $Jc(H)$ vanishes. At higher fields $H^* <$ H $<$ H_{c2} both cuprates and FBS behave as poor metals and the high values of H_{c2} become irrelevant. The dissipative field domain $H^* <$ H $<$ H_{c2} widens significantly in anisotropic materials with low carrier density, as illustrated in Figure 14, which shows that, for highly anisotropic cuprates,$H*(T)$ can be much lower than H_{c2}(T).

One may think that pinning nanostructures, which enhance Jc so effectively, could also increase $H*$ by preventing thermal wandering of vortices in the layered cuprates. However, this seems not to be the case, even for $YBa_2Cu_3O_7$ films with highest Jc values, H^* is not increased significantly [74, 75], indicating that $H*$ may be mostly limited by intrinsic materials parameters. It is the reduced irreversibility fields of the cuprates, which are behind one of the fundamental obstacles for high-field applications at 77 K.

2.13.1 The Critical State

We now move to the other extreme in which pinning is strong enough to prevent any substantial vortex motion. In rigorous terms, for a stable configuration of flux, the Lorentz force must not exceed the available local pinning strength $\alpha_p(B)$ everywhere. Mathematically, this situation can be expressed as

$$F(T) = \left\langle \frac{\Delta(T)}{\Delta(0)} tanh \frac{\Delta(T)}{2K_B T} \right\rangle \tag{2.56}$$

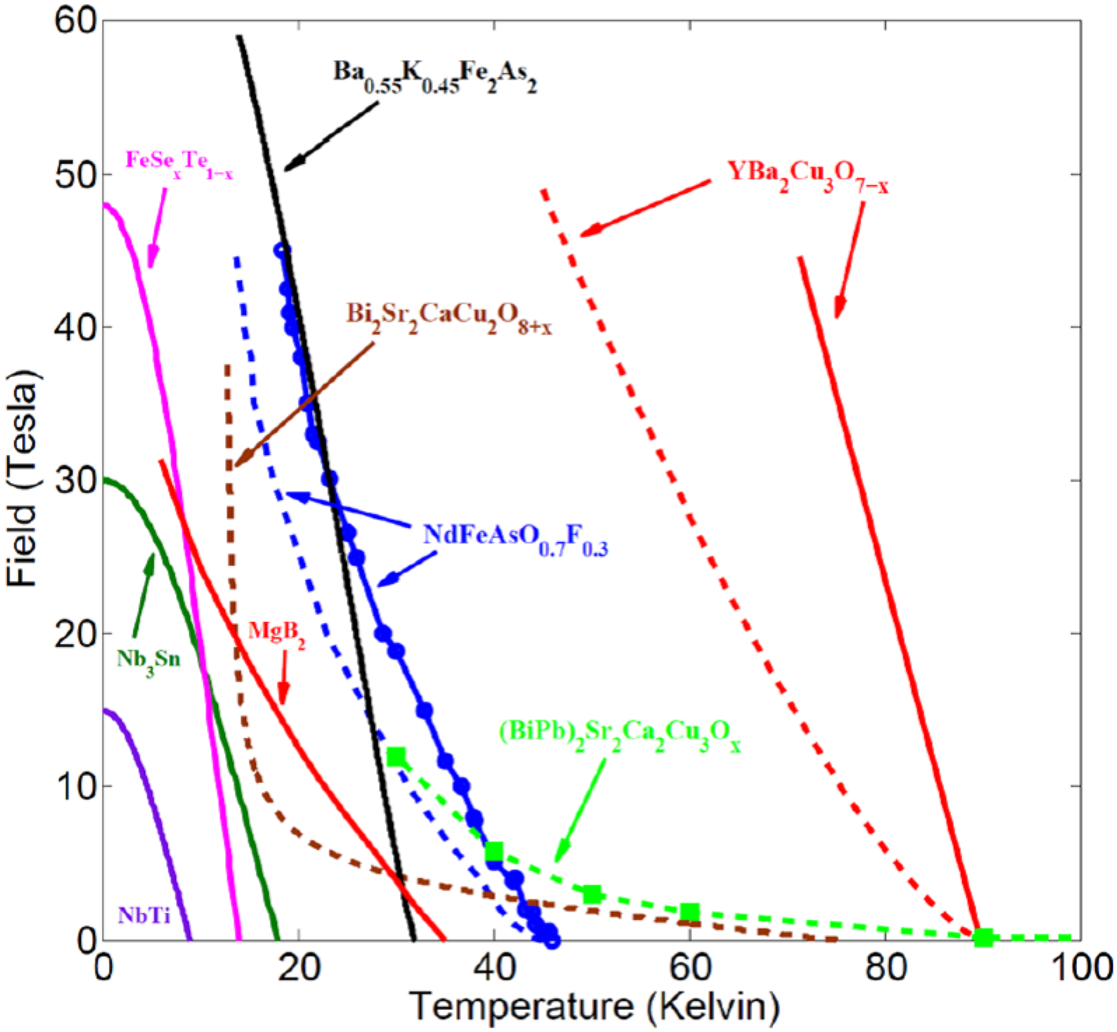

Figure 14: T-H phase diagram for different superconducting materials[79].

$$\frac{1}{c}|J \times B| < \alpha_p(B) \tag{2.57}$$

However as proposed [87,88] once there is a current flowing in any macroscopic region. The current must take up the maximum value (critical current in (2.13). So, only three states of current flow are possible, zero current for those regions that have never felt the magnetic field and full current (say positive or negetive) flows elsewhere, the sense of this current depends on the sense of the electromotive force that accompanied the last local change of the thermodynamic field. If the critical current is flowing everywhere in a specimen, then the specimen is in a critical state which is defined by the equality in equation 2.57 everywhere. In principle, it should be possible to determine the spatial profiles of B and J from the equality in above equation and

$$J = c(\delta \times Y)/4\pi \tag{2.58}$$

together with the explicit relation Y(B), which is usually taken as $y = B$ in high superconductors in the field range H > H_{c1} [89].

.

2.14 The Two-component Critical State Model

The two fluid model was proposed by Gorter and Casimir as a tool to describe some of the properties of superconductors. In the two fluid model, it is considered that there are two types of electrons in the superconductor, the normal electrons (the normal fluid), and the superconducting electrons (the super fluid) [85]. In a given field, the normal electrons are assumed to behave like electons in the normal state and therefore dissipate energy by scattering. Their motion is described by the usual transport equation:

$$m\frac{dj_n}{dt} + m\frac{j_n}{\tau} = N_n e^2 E \tag{2.59}$$

where j_n=N_ne v_n, with j_n being the normal current density, N_n the density, v_n the drift velocity of the normal electrons, and τ the relaxation time [86]. The superconducting electrons do not dissipate energy as they move; however, they do show inertial effects due to their mass.

2.15 Non-resonant Microwave Absorption

The first observation of non-resonant microwave absorption in the high-Tc superconductor was published by Bhat et al., [3] soon after the discovery of HTSC by Bednorz and Muller. This was followed by large number of reports [65]. In ceramic samples, it was shown by Portis et al., [4] that the absorption has a minimum at zero field and then increases smoothly with increase in applied magnetic field. This is attributed to fluxon motion driven by microwave currents. In single crystals, instead of smooth absorption as a function of applied field, line spectra are observed [6]. This kind of line spectra are not a peculiarity of the high-T_c superconductors but has also been found in conventional super conductor eg Nb [6]. Their origin is thought to be microwave current induced nucleation and annihilation of fluxons within sections of a Josephson junction in a superconducting loop intersecting an applied magnetic field [6]. Dulcic et al., [7] have also observed such discrete microwave absorption line in YBCO single crystal for H ab-plane. Owen [79] explains this in the following way. Since flux is quantized in the superconducting loop, there are phase jumps as the applied field increases. These phase jump occur when the field enclosed becomes an integral multiple of the unit quantum of flux. These flux jumps occur in a very short time and therefore produce large voltage pulses given by V(t)= - $\frac{h}{2e}\frac{d\theta}{dt}$. When this occurs the critical current of the superconductor is exceeded and normal current flows which can absorb microwave energy. Thus the microwave absorption spectrum of this loop as a function of increasing DC magnetic field will be a series of equally spaced sharp absorption which are separated from each other by $\frac{\phi_0}{A}$, where A is the area of the loop. In the case of pellets, the signal is thought to be an envelope of these superposed line absorptions because of a distribution in the weak links and the different possible loop orientations with respect to the DC magnetic field.

2.16 Critical Current Density Measurement of YBCO Thin Films by Non-resonant RF Absorption Method

As mention earlier by Bhat et al., [3] it is normal practice in the CW EPR and NMR spectrometer to use low frequency magnetic field modulation and phase sensitive detection which results in the field derivative of the absorption being recorded. This fact can also be used, to determine the critical current density Jc of superconducting material [79]. Hence the study of thin film sample of the YBCO compound and measure the intensity dependence of the signals on the amplitude of the modulating field and interpret it in terms of the Bean critical state model.

2.16.1 Bean Critical State Model

The flux density inside the sample can be written as

$$\mathtt{B} = \mathtt{B}(\mathtt{H}_0) + \sum_{\mathtt{n}=1}^{\propto} \alpha_{\mathtt{n}} \mathtt{sin}(\mathtt{n}\omega\mathtt{t}) \tag{2.60}$$

with α_1 (the amplitude of the first harmonic) $\dfrac{H_{ac}^2}{H^*}$ for H$_{ac}$ $\leq$H* where H$_{ac}$ is the amplitude of the AC field and H* the field value for which the flux penetrates the entire sample. The origin of the rf loss in the case of single crystals and crystalline thin films are essentially in the damped motion of fluxons [78]. Therefore, the loss S=fn , where a fraction of f of the fluxon density $n = \dfrac{B}{\phi_0}$ with ϕ_0 the elemental flux quantum, is considered to be free. Therefore,

$$\mathtt{S} = f[\mathtt{B}(\mathtt{H}_0 + \frac{\mathtt{H}_{\mathtt{ac}}^2}{\mathtt{H}^*\mathtt{sin}(\omega\mathtt{t})}) + \mathtt{higher{-}harmonics}]. \tag{2.61}$$

In this expression, the first term represents the dependence of the general line-shape, hysteresis and flux trapping with respect to the DC field. The second term contains the information on the modulation effects. The maximum loss S$_{loss}$ in a modulation cycle will be proportional to

$$\frac{(H_{ac} + H_0)^2}{H^*}. \tag{2.62}$$

Since this method will be applied in the experiment, consequent to lock-in detection, the derivative of the loss will be

$$\frac{dS}{dH} = \frac{2(H_{ac} + H_0)}{H^*}. \tag{2.63}$$

If the modulation amplitude H_{ac} increases starting from a small value until H^* , we expect a linear dependence of recoded signal intensity of H_{ac}. For H_{ac} $\geq$H* , there will be a departure from the quadratic dependence of the first harmonic on H_{ac} resulting in the departure of the signal intensity from linearity. However, the field value for which the departure occurs corresponds to H^* , hence

$$H^* = \frac{\pi J_c D}{Total{-}peaks} \tag{2.64}$$

where D is the thin film width and J_c can be calculated using this relation. However, this J_c is only an effective and not the true J_c as shown by Bhat et al., [84], in calculating J_c from the relation

$$\nabla \times H = \frac{4\pi J_c}{C} = \frac{\partial H_D}{\partial z}\frac{\partial H_z}{\partial D}. \qquad (2.65)$$

For thin film geometry, the term $\frac{\partial H_D}{\partial z}$ i.e the gradient of the radial field along the axial direction z is the dominate one rather than the term $\frac{\partial H_z}{\partial D}$ used for calculating the J_{eff} by this factor. Hence, J_{eff} obtained from the transport current method and J_c determined from the non-resonant RF absorption technique [66].

2.17 Distinction Between Weak Link and Bulk Responses

One of the characteristic features of the high-Tc superconductors is the hierarchy of weak links they contain. These weak links are comprised mainly of the grain boundaries in dense powder and compact sintered pellets. It is possible that due to the very short coherence length characterizing these materials, point defects, oxygen vacancies and even the insulating layers in between the conducting planes can act, in certain respects, like weak links. Since the lower critical Hc_1 of weak links is of orders of magnitude smaller than ($\sim 0.1Oe$) that of the bulk, the magnetic field penetration is more facile into the junctions than into the bulk material. The critical current through the junctions then becomes dependent on the field according to well-known diffraction relation $\mathrm{J}_c = J_c(0)[sin(\frac{H}{H_0})/\frac{H}{H_0}]$, where the symbols have their conventional meanings(junction current , Jc), and thus lead to the observed field dependence absorption [6]. This model has been proposed and successful adapted to explain the low field absorption behaviour by researchers [6, 80]. However, it is also possible when size of the junction d is such that d> λ_L (where λ_L is the London penetration depth) fluxons are nucleated within the weak links and their viscous motion will results in dissipation. This model was proposed by Portis et al., [4] to explain the low field absorption in pellets sample, to be discussed.

2.18 Modulated and Non-modulated Low-magnetic Field Microwave Absorption

Since superconducting state microwave response of granular superconductors seems to be a common feature due to Josephson coupling between the grains, it can be detected at the various frequencies and by the various types of microwave detecting setups. A few results which have been published were obtained by using of Q-band ESR spectrometers operating at about 20 GHz [81], 23 GHz [16], 35 GHz [82], and by special spectrometer with frequency variable within the range 1-38 GHz [79]. Several groups have reported the low field signal (LFS) study using NMR spectrometers operating in MHz frequency range [83]. However, most studies published have been done by means of conventional X-band ESR spectrometers operating at about 9-10 GHz using magnetic field modulation. The absorption can be detected both in very low magnetic field and high magnetic field. Since a magnetic field Hext at the sample loaded into the spectrometer cavity comprises three components, $\mathrm{H}_{ext}(t) = \mathrm{H(t)} + \mathrm{H}_{mod} sin(_{mod}t) + H_{mw} cos(_{mw}t)$ where H(t) is a scanning magnetic field of a spectrometer d.c. magnet, Hmod is a modulation field amplitude changing with frequency ω_{mod} ~10-100 kHz, and H_{mw} is a magnetic component of microwave field changing with frequency ω_{mw} ~10 GHz, the final picture depends rather strongly on what kind of detecting scheme is used in the low-magnetic field microwave absorption experiment [88].

References

[1] R.M. Kadam,B.N. Wani,M.D. Sastry and U.R.K. Rao, *Physica* . C, 246-262, (1995).

[2] K.W. Blazey, K.A. Muller, J.G. Bednorz, W. Berlinger, G. Amoretti, E. A. Buluggiu, and F.C. Matacotta, *Phys. Rev.* B 36, 7241 (1987).

[3] S.V. Bhat, P. Ganguly and C.N.R. Rao, *Pramana J. Phys.* 28, L425 (1987).

[4] A.M. Portis, K.W. Blazey, K.A. Muller and J.G. Bednorz, *Euro. Phys.* Lett 5, 467 (1988).

[5] A. Dulcic, B. Leontic, M. Peric and B. Rakvin, *Euro. Phys.* Lett 4, 1403 (1987).

[6] A. Dulcic, R.H. Crepeau, J.H. Freed, L.H. Schneemeyean and J.V. Waszezak, *Phys. Rev.* B 42, 2155 (1990).

[7] A. Dulcic, R.H. Crepeau and J.H. Freed, *Phys. Rev.* B 39, 4249 (1989).

[8] E.J. Pakulis and G.V. Chandershekar, *Phys. Rev.* B 39, 808 (1989).

[9] K. Sugawara, N. Arai, A. Kouzuki, S. Ichimura, H. Naoi, K. Hotta and H. Hirose, *Inter.J.Modern Physics.* B 14, No.16, 1633 (2000).

[10] G.K. Padam, S.N. Ekbote,M.R. Tripathi, G.P. Srivastava and B.K. Das, *Physica.* C 315, 45 (1999).

[11] R.M. Kadam, M.D. Sastry, Z. Hassain, C. Mazumdar, R. Nagarajan, L.C. Gupta, C. Godart and R. Vijayaraghvan, *Physica.* C 232, 359 (1994).

[12] R.M. Kadam,B.N. Wani, M.D. Sastryand and U.R.K. Rao, *Physica.* C, 246-262 (1995).

[13] J.T. Suss,W. Berlinger,A.M. Portis,K.A. Muller,B. Jeanneret and P. Martinoli, *Solid State Commun.* 71, 929 (1989).

[14] V. Kataev, N. Knauf, B. Buchner and D. Wohlleben, *Physica.* C 184, 165 (1991).

[15] J.M. Baranowsky, W.Z. Lilientel, W.F. Yan and E.R. Weber, *Phys. Rev.* Lett 66, 3079 (1991).

[16] K. Moorjani, J. Bohandy, B.F. Kim and F.J. Adrian, *Solid State Commun.* 74, 497 (1990).

[17] P. Bele, H. Brunner, D. Schweitzer and H.J. Keller, *Solid State Commun.* 92, 189 (1994).

[18] J.P. Joshi, , S. Sarangi, A.K. Sood, D. Pal, and S.V. Bhat and J. Parman, *Phys.* 58, 361 (2002).

[19] N.Y. Panarina, Y.I. Talanov, T.S. Shaposhnikova, N.R. Beysengulov, G. Vavilona, E. Behr, A. Kondrat, C. Hess, N. Leps, S. Wurmehl, R. Klinger, V. Kataev and B. Bchner, *Phys. Rev.* B 81, 224-509 (2010).

[20] N. Pascher, J. Deisenhofer, H.A. Krug von Nidda, M. Hemmida, H. Jeevan,S. P. Gegenwart and A. Loid, *Phy. Rev.* B 82, 054-525 (2010).

[21] C. Kittel, Solid State Physics J.Wiley, USA. (2005).

[22] M. Ashcroft, Solid State Physics (Cornell University, USA. (1976).

[23] M. Cyrot, *Rep. Prog. Phys.* 36, 103 (1973).

[24] D. Ahmad, T.K. Song, I.S. Park, G.C. Kim, Z.A. Ren and Y.C. Kim, *Mod. Phys. Lett.* B 25, 1939 (2011).

[25] S.V. Sharma, T.K. Nath and A.K. Majumdar, *Physica.* C 290, 229-238 (1997).

[26] K. Fossheim and A. Sudbo, Superconductivity Physics and Applications Wiley, Chichester West Sussex, England.(2004).

[27] U. Welp, K. Kadowaki and R. Kleiner, *Nat.Photonics.* 7, 702 (2013).

[28] A. Mourachkine, Room Temperature Superconductivity CISP, Chippenham, England.(2004).

[29] N. Plakida, High-Temperature Cuprate Superconductors Experiment, Theory, and Applications springer, Dubna Moscow Region, Russia.(2010).

[30] P.J.W. Moll, X. Zhu, P. Cheng, H.H. Wen and B. Batlogg, *Nat. Phys.* DOI:10.1038/NPHYS3034.(2014).

[31] G. A. Alvarez, I. Iguchi, X.L. Wang, S.X. Dou and Q.W. Yao, *J. Appl. Phys.* 99, 08M514 (2006).

[32] K. N. Srivastava, Superconductivity, Theoretical and experimental aspect, USA, (1996)

[33] C. C. Tsuei and J. R. Kirtley, *Rev.Mod.Phys.* 72, 969 (2000).

[34] B. B. Jin , T. Dahm, A. I. Gubin, E.M. Choi, H.J. Kim, S.I. Lee, W.N. Kang and N. Klein, *Phys. Rev. Lett.* 91, 127006 (2003).

[35] D. Cunnane, C. Zhuang, K. Chen, X.X. Xi, J. Yong and T.R. Lemberger, *Appl. Phys. Lett.* 102, 072603 (2013).

[36] M. M. Hossain Absolute Value of The Magnetic Penetration Depth and field Profile in the Meissner State of Exotic Superconductor $YBaCu_3O_{6+x}$ and $Ba(CO_{0.072}Fe_{0.926})2As_2$ (Phd Thesis), University of British Colombia (2012). (accessed on 12 march 2017)

[37] J. Kim, N. Haberkom, S.Z. Lin, L. Civale, E. Nazaretski, B.H. Moeckly, C.S. Yung, J.D. Thompson and W. Movshovich, *Phys. Rev.* B 86, 024501 (2012).

[38] L. Ji, M.S. Rzchowski and M. Tinkham, *Phys. Rev.* B. 42, 4838 (1990).

[39] S.X. Dou, S. Soltanian, J. Horvat, X.L. Wang, S.H. Zhou, M. Lonescu and H.K. Liu, *Appl. Phys.* Lett. 81, 3419 (2002).

[40] N.Y. Panarina, Y.I. Talanov, T.S. Shaposhnikova, N.R. Beysengulov and E. Vavilova, *Phys. Rev.* B 81, 224509 (2010).

[41] J. Hanisch, K. Iida , F. Kurth, E. Reich, C. Tarantini, J. Jaroszynski, T. Forster, G. Fuchs, R. Huhne, V. Grinenko, L. Schultz, and B. Holzapfe, *Scientific Reports.* vol 5, 17363 (2015).

[42] Y. Talanov, N. Beisengulov, G. Kornilov, T. Shaposhnikova, E. Vavilova, C. Nacke, S. Wurmehl, N. Panarina, C. Hess, V. Kataev and B. Buchner, *Supercond. Sci. Technol.* 26, 045015 (2013).

[43] L. Fang, Y. Jia, V. Mishra, C. Chaparro, V. K. Vlasko-Vlasov, A. E. Koshelev, U. Welp, G. W. Crabtree, S. Zhu, N. D. Zhigadlo, S. Katrych, J. KarpinskiW, K. Kwok, *Nature Communications.* vol 4, 2655 (2013).

[44] V. V. Srinivasu, Non resonant RF and microwave absorption studies (Phd Thesis), Indian Institute of Science, India. (1994).

[45] D. B. Jan, J. Y. Coulter, M.E. Hawley, L.N. Bulaevskii, M.P. Maley and Q.X. Jia, *Appl. Phys. Lett.* 82. 5 (2003).

[46] M.W. Coffey and J.R. Clem, *Phys. Rev. Lett.* 67, 386 (1991).

[47] L. Ji, M.S. Rzchowski, N. Anand and M. Tinkham, *Phys. Rev.* B 47, 470 (1993).

[48] P. Muller A.V. Ustinov, The Physics of Superconductors: Introduction to Fundamentals and Applications Springer, Germany. (1997).

[49] A. Franz, A. Wallraff and A.V. Ustinov,*J. Appl. Phys.* 89, 471 (2001).

[50] B. Andrzejewski, B. Cryzak, L. Szczesniak and J. Stankowski, *Appl. Magn. Reson.* 8, 35 (1995).

[51] J. C. Gallop and W.J. Radcliffe, *Supercond. Sci. Technol.* 4, 568 (1991).

[52] C.J. Wu and Y.L. Chen, *Prog. Electromagn. Res.* 111, 433 (2011).

[53] A.H. Aly and W. Sabra, *Physica.* C 495, 126 (2013).

[54] M.R. Tripathy and G.P. Srivastava, *IEEE Trans. Magn.* 35, 4079 (1999).

[55] V.V. Srinivasu, B. Thomas, M.S. Hegde and S.V. Bhat, *J. Appl. Phys.* 75, 4131 (1994).

[56] A. Dulcic, B. Rakvin and M. Perik, *Europhys. Lett.* 10, 593 (1989).

[57] A. Rastogi, Y.S. Sudershan, S.V. Bhat, A.K. Grover, Y. Yamaguchi, K. Oka and Y. Nishihara, *Phys. Rev.* B 53, 9366 (1996).

[58] J.T. Masiakowski, P. Micky and K. Larry, *J. Phys. Chem.* 95, 1393 (1991).

[59] V. V. Srinivasu, S.V. Bhat and N. Kumar, *J. Supercond. Nov. Magn.* 14, 41 (2001).

[60] V.V. Srinivasu, *J. Supercond. Nov. Magn.* 23, 305 (2010).

[61] K.W. Blazey, A.M. Portis, K.A. Muller and F.H Holtzberg, *Europhys. Lett.* 6, 457 (1988).

[62] K.W. Blazey, A.M. Portis, K.A. Muller, J.G. Bednorz and F.H. Holtzberg, *Physica.* C 56, 153-155 (1988).

[63] F. J. Owens, *Physica.* C 171, 25 (1990).

[64] V.V. Srinivasu, R. Pinto and M.D. Sastry, *Appl. Supercond.* 4, 195 (1996).

[65] S.V. Bhat, V.V. Srinivasu and N. Kumar, *Phys.* Rev 44, 10121 (1991).

[66] V.V. Srinivasu, S.V. Bhat and N. Kumar, *Solid state Commun.* 89, 375 (1994).

[67] A.K. Pradhan, S.B. Roy, P. Chaddah, C. Chen and B.M. Wanklyn, *Phys. Rev.* B 52, 6215 (1995).

[68] G.K. Padam, N.K. Arora and S.N. Ekbote, *Mat. Chem and Phys.* 123, 752 (2010).

[69] A. Rastogi, V.V. Srinivasu, M.S. Hedge and S.V. Bhat, *Physica.* C 234, 229 (1994).

[70] M. Puri, R. Durny and L. Kevan, *Physica.* C 190, 210 (1992).

[71] S.V. Bhat, A. Rastagi, N. Kumar, R. Nagarajan and C.N.R. Rao, *Physica.* C 219, 87 (1994).

[72] F.V. Kusmartsev, *Phys. Rev. Lett.* 69, 2268 (1992).

[73] W. Braunish, N. Knauf, V. Kataev, S. Neuhausen, A. Grutz, A. Kock, B. Roden, D. Khomskii and D. Wohlleben,*Phys. Rev.* Lett 68, 1908 (1992).

[74] S.P. Chockalingam, S. Sarangi, S.V. Bhat, K. Oka and Y. Nishihara, *J. Phys. Condens. Matter.* 21, 045704 (2009).

[75] S. Sarangi, S.P. Chockalingam and S.V. Bhat, *J. Appl. Phys.* 98, 073906 (2005).

[76] D. Shaltiel, H.A.K. Nidda, A. Loidl, B. Rosenstein, B.Y. Shapiro, I. Shapiro, T. Tamegai and B. Bogoslavsky, *Phys. Rev.* B 77, 014508 (2008).

[77] A. Dulcic, R.H. Crepeau and F. Freed, *Phys. Rev.* B 38, 5002 (1988).

[78] Y. Maniwa, A. Grupp, F. Hentsch and M. Mehring, *Physica.* C 156, 755 (1988).

[79] Owens F J, *Phys.* Lett A 151, 349 (1990).

[80] N.Y. Panarina, Y.I. Talanov, T.S. Shaposhnikova, N.R. Beysengulov and E. Vavilova, *Phys. Rev.* B 81, 224509 (2010).

[81] V. Selvamanickam, D. W. Hazelton, L. Motowidlo, F. Krahula., J. Hoehm, M. S. Walker, P. Haldar, *J. Min. Met and Mat. Soc.* 50, 27-30 (1998).

[82] T.J. Haugan, P.N. Barnes, R. Wheeler, F. Meisenkothen, and M.D. Sumption, *Nature.* 430, 867-870 (2004).

[83] B. Maiorov, S.A. Baily, H. Zhou, O. Ugurlu, J.A. Kennison, P.C. Dowden, T.G. Holesinger, S.R. Foltynm and L. Civale, *Natur. Mat.* 8, 398-404 (2009).

[84] P. Mele, K . Matsumoto, T. Horide, O. Miura, A. Ichinose, M. Mukaida, Y. Yoshida and S. Horii, *Supercond. Sci. Technol.* 19, 44-50 (2006).

[85] Y. Zhang, J. Jiang, C.W. Bark, J.D. Weiss, A. Polyanskii, C. T. Nelson, C. Tarantini and S. Lee, *Appl. Phys.* Lett 98, 042509 (2011).

[86] T. Katase, H. Hiramatsu, T. Kamiya, and H. Hosono, *Appl. Phys.* Express 3, 063101 (2010).

[87] R. Marcon, R. Fastampa, M. Giura, and C. Matacota, *Phys. Rev.* B 39, 2796 (1989).

[88] D. Braithwaite, G. Lapertot, W. Knafo, I. Sheikin, *J of the Phy. Soc. of Japan.* Vol 79, No. 5, 15 (2010).

[89] Y.Y Luo, Y.C Wu, X.M Xiong., Q.Y Li, W Gawalek, Z.H He, *J. Supercond.* 13 (4) 575-581 (2000).

3 CHAPTER THREE

3.1 High-Tc Superconductors

Oxides are the most abundant inorganic materials on Earth. The perovskite and related oxides represent a very large group of compounds that display the most diverse physical properties. High temperature superconductors (HTSC) just happen to be a small group of these materials. This high temperature superconductivity was discovered in 1986 by Bednorz and Muller in $La_{2-x}Ba_xCuO_4$ cuprate at Tc = 35 K. However, contrary to all expectations, it still awaits an explanation that has a consensus in general. This situation is due to a number of basic experimental facts which are rather unusual but on which a consensus has grown since the discovery [1]. The following is a list of these facts:

- An unusual phase diagram. The two important points are that the undoped material is a Mott insulator and a strange high temperature metallic phase appears.
- The superconducting cuprates are very high-Kappa materials due to an extremely small coherence length compared to low-temperature materials and a large penetration depth.
- Most experiments tend to point that contrary to conventional materials, cuprates are d-wave superconductors.
- Many properties of the superconducting state remain unclear as far as the explanation is concerned, such as the scattering by impurities.

The physical properties in the normal state of the high temperature superconductors are very complex such that there is no theory available yet to explain them in a consistent way. Deeper understanding of the strongly correlated system may be necessary in order to find a consistent theory for high temperature superconductivity [1].

3.2 Processing of High-T_c Superconductor

It is known that T_c and H_c values of a superconductor are generally intrinsic properties of a given material on superconductivity in HTSC. On the other hand, J_c and λ values can be thought as a function of sample microstructure. In addition, these values can vary by several orders of magnitude owing to various processing techniques [2].

For electrical applications of HTSC, a high-J_c at large magnetic fields is desirable. Although high critical current densities are achieved in bulk, thin films and wires, several processing-related problems need to be addressed. These are:

- grain boundaries,
- metallurgical defects,
- flux pinning mechanism, and
- flux creep.

Grain boundaries are interfacial regions between adjacent grains. They could contain impurity phases, normally conducting or insulating, extending beyond the coherence length of electrons in these superconductors. These boundaries create Josephson junctions, so that the critical currents of which are much lower than in a homogenous superconductor. Because of this reason they are called as weak links. The grain boundaries affect the bulk critical current density and hence they are particularly a problem in polycrystalline bulk superconductors. Also they contribute to surface resistance of a superconductor. If Jc needs to be improved, processing of HTSC materials should minimize the grain-boundary effects and also enhance the flux pinning sites in the superconductors. To improve the critical currents of grain boundaries, a small percentage of nickel nanomanetic can be added into HTSC materials. In addition this, texturing of a bulk superconductor to align grains along ab-planes reduces the detrimental effects of grain boundaries. It has been observed that the critical current density across the grain boundaries depends on the misorientation angle of the two grains. However, the elimination of high-angle grain boundaries in HTSC materials has been a difficult impediment to overcome. Recent developments in YBCO-coated conductors show promise in reducing the presence of high-angle grain boundaries. By the introduction of the controlled amounts of defects, such as coexisting normal secondary phases by alloying, or by neutron or proton irradiation to define normal regions along the particle trajectory that give rise to higher critical densities and higher critical magnetic fields, enhancement of flux pinning and suppression of flux creeping have been achieved [1,2]. Bulk superconductors with large volume fraction of superconductivity are being routinely synthesized in YBCO, Tl, and Bi based HTSC materials. Improved powder synthesis, understanding of reaction chemistry, and phase diagrams have led to increased phase purity and improved flux pinning. The two widely used processing methods for bulk HTSC are solid-state reaction and melt-texturing. Also, sol-gel synthesis, simple wet-chemical methods, combustion synthesis and microwave synthesis are the other synthesis procedures that are commonly employed.

3.3 Processing of Bulk Superconductors

For the choice of bulk superconductors for different applications such as magnets,[3] current leads and superconductor magnetic energy storage systems, there are three important process considerations:

- growth of large-area, single-phase bulk conductors,
- ease of introducing strong flux pinning centers in the bulk, to enhance the critical currents, and
- long-term stability and aging under ambient conditions.

When it is compared with various other bulk superconductors, it is realized that YBCO is the most plausible for electrical applications because of the crystal structure and ease of synthesizing single-phase specimens. Although introduction of flux pinning centers to enhance J_c has not been demonstrated in Bi, Tl, and Hg superconductors, this case has been demonstrated in YBCO. Further more, melt processing growth of YBCO superconductors provides grain-alignment resulting in JC as high as 10^5 A/cm^2 at self field and 77 K [3]. The performance of bulk materials has been significantly improved in the case of YBCO by the melt powder / melt growth (MPMG) processing. Tl including superconductors are attractive since their Tc are as high as 125 K, Jc in bulk greater than $10^5 A/cm^2$ at 77 K and zero-field [4]have been achieved. The magnetic field dependence of J_c is comparable to the best YBCO superconductors. The toxicity of Tl is the disadvantage of thallates, which needs very careful handling and processing. The volatility of Tl gives rise to its losses during high temperature synthesis. Volatility of mercury compounds creates unique problems in the synthesis of Hg-based HTSC. In the production of bulk superconductors, all processing must be done in a sealed enviroment because HgO decomposes around 500^oC. The Bi compounds are not attractive for bulk conductors primarily, too, due to the polycrystalline nature of the grains and weak flux pinning. Melt-texturing of Bi compounds is not as simple as the YBCO compounds. Generally it is thought that the Bi compounds are attractive for wire applications due to their micaceous morphology.

3.4 Problem of Preparing Nanoparticles

The preparation of nano-crystalline (α-silicon carbide) for studying the sintering mechanism is also a very difficult problem. The properly distributed nanocrystalline particles within the very narrow range by grinding necessitates a proper understanding of the process of grinding of silicon carbide. At the initial stage, large cracks in original particles propagate, generating smaller particles with very fine cracks. Thus, the probability of particles having cracks progressively decreases with grinding leading to the generation of newer stronger particles. Hence, continuously higher and higher fracture stress is required to grind the particle. During the grinding, it becomes progressively difficult to obtain further reduction in particle size in nanocrystalline region [5]. In the nanocrystalline region, the nanoparticles develop the tendency to agglomerate and the physical equilibrium between the aggregates and fragmentation is established, resulting in a decrease in storing of stress energy. Consequently, it results in an increased stress for initiating fracture and the generation of nanoparticles. There are two principal factors which need to be controlled to obtain nanoparticles :

- Ratio of the weight of the metal balls of grinding media to the total weight of the particles to be processed by the grinding route.

- Another factor of importance is the total time of grinding, which also needs to be controlled in order to optimize the process of grinding to obtain nanoparticles [5, 6]

3.5 Structural Ordering of Ferrites

The preference of certain metal cations to octahedral B or tetrahedral A coordination in FCC oxygen lattice is dictated by the crystal field theory. The particular preference of an ion for octahedral or tetrahedral coordination decreases in the following order : Cr^{3+}>Mn^{3+} >Ni^{2+} >Cu^{2+} > Al^{3+} > Co^{2+} > Mg^{2+} > Ti^{3+} > Fe^{2+} > Fe^{3+} > Mn^{2+} > Zn^{2+}. Although our knowledge of magnetic properties and magnetic materials have grown with time, the secrets of the extensive class of ferrites are sill largely hidden[7]. Due to the above order, certain conclusions can be made as follows :

- Most of the spinels which contain aluminum are normal, except for those of nickel and copper.
- The proximity of the Fe^{2+} and Fe^{3+} ions indicates that they can easily interchange their positions between the A and B sites.
- Nickel, cobalt, copper, and magnesium ferrites are predominantly inverse, i.e., divalent ions prefer octahedral coordination, but in certain instances, these ions occupy normal positions as in mixed spinels.
- Zinc spinel is a normal spinel.
- Some sort of structural disorders have been detected in spinels, e.g., a shift of oxygen and the metal cations in the item B sites can create local permanent dipoles in ferrites, which could interact spontaneously in the anti-parallel orientation [8].

3.6 Ferromagnetic Materials

Ferromagnetic materials exhibit a wide variety of behaviors when subjected to AC magnetic fields, ranging from domain wall relaxation (DWR), to giant magnetoimpedance (GMI), to ferromagnetic resonance (FMR). While DWR is limited to low frequencies where domain walls are able to follow the frequency of the excitation field (usually lower than 1 MHz [8]), FMR phenomena must satisfy an exact equation (the Larmor equation, usually for frequencies in the GHz range [9]). GMI has shown to extend on an extremely wide frequency range [10]. On the other hand, in other studies, microwave absorption centered at zero magnetic field has been observed in a wide variety of materials. For high temperature superconductors the appearance of this absorption has been widely accepted as a signature of the transition to the superconductive state [10]. This signal reflects the dissipative dynamics of fluxons. For ferrites, this low-field absorption signal is due to microwave absorption processes closely related to the low-field magnetization of the sample [9]. For semiconductors this signal is due to magnetoresistive effects that are responsible for most of the magnetic field dependence of the microwave absorption [11]. For manganites the appearance of the microwave absorption centered at zero magnetic field is used to indicate the onset of the ferromagnetic phase and provides a sensitive detector of ferromagnetism [8]. Recently, the microwave response near zero magnetic field was observed in doped silicate glasses [9].

3.7 Sample Preparation and Material Synthesis

In this section we will describe various methods of sample preparion and again the techniques used to synthesize those materials starting from solid-state reaction and melt-texturing. sol-gel synthesis, simple wet-chemical methods, combustion synthesis and microwave synthesis are the other synthesis procedures that are commonly employed.

3.8 Processing YBCO Bulk Superconductor

Despite the impressive progress in high temperature superconductors, researchers have soon realized that there are many tough problems which must be solved before the commercialization of ceramic superconductors is possible. The complexities of the problems dampened almost all enthusiasm of the study on the bulk materials, at least by the physicists, who have now turned their research activities to pellets, powder and thin films.

According to Gallagher and others as mentioned from [12], $\mathrm{YBa_2Cu_3}O_x$ will go from non-superconducting to superconducting and to non-superconducting again as oxygen is removed or added to the structure. This phenomenon is associated with the orthorhombic↔ tetragonal, and when $x > 7.1$ they also are non-superconducting. The best superconductors, which must be orthorhombic, were found with $x = 6.98$, with x being a function of both temperature and oxygen partial pressure.

3.8.1 Conventional Solid State Reaction Method

The simple, economic, and hence the most widely used method for the processing of bulk HTSC material is the solid-state reaction method, or calcination. It is also known as the conventional method. In this method, first carbonates, or oxides of Ba, Ca, Cu, and Y as starting materials, are mixed and grounded to the desired size and heat-treated in an alumina crucible at temperatures as high as 950 ^{o}C for 24 h. After cooling to room temperature, the reacted sample is finely grounded and mixed again, and heat-treated for an additional 24 h. This step is repeated for the homogeneity of the sample. Following these steps, the samples are pelletized in desired shapes using a hydraulic press at a typical pressure of 1500 Pa. Then the pellets are placed in a crucible made out of alumina, gold, or platinum and introduced into a furnace preheated to 900 ^{o}C, and sintered typically in air for 24 h. To give rise to the growth of the orthorhombic superconducting phase, oxygen is introduced into the furnace at around 500 ^{o}C, during the slow cooling of the samples to room temperature. Unintentional phases such as $\mathrm{BaCuO_2}$, CuO and possibly some contamination from the heat treatment process may be present in samples. In the spite of this disadvantage, this technique is very time effective. The conventional method has these kinds of limitations, but also it has an advantage to attain a Tc of 90 K and current densities of 10^4 A/cm^2 at zero field at 77 K [14, 15]. In such samples, the polycrystalline nature of grains results in poor field dependence of J_c, which decreases by three orders of magnitude in a magnetic field of 0.1 T.

3.8.2 Texturing of YBCO 123 Superconductors

Bulk melt-textured HTSC materials allow novel applications, such as magnetic bearings and magnetic shields. Flywheel demonstrators have already been produced on a trial basis. Bulk superconducting materials for rotating machines with high current loads require J_c values as large as possible. The melt-texturing techniques are the most suitable for enhancement of J_c. Using mechanical, magnetic and meltgrowth techniques, texturing of YBCO can be achieved. The mechanical and magnetic means yield only a marginal improvement in superconducting properties, mainly owing to the presence of large-angle grain boundaries, whereas melt growth techniques reduce the large-angle grain boundaries and improve the critical current. A series of process-modifications such as melt texture growth (MTG), quench and melt-growth (QMG) [1], melt powder melt growth (MPMG) [16], seed melt growth [1], and liquid phase removal methods [17] are developed for the nondirectional solidification. In such techniques, with improved connectivity between grains, large YBCO crystals can be grown stacked along the c-axis. Also, during the melt processing, directional solidification is possible by providing the right thermal gradient. Directional solidification methods align the grains along the ab-planes, the direction of current flow, thus improving the current-carrying capability. Seed melt growth and liquid phase removal methods can also be used to align the grains along a desired orientations. A directionally oriented single crystal Sm123 or Nd123 is used as a seed material to grow YBCO, oriented along the same preferred direction in the seeded melt growth technique. The melt texture growth of YBCO 123 involves melting the YBCO above its peritectic temperature, approximately 1010 ^{0}C, in air. When heated above this temperature, the 123 compound undergoes incongruent melting to form a solid and a liquid phase according to the following reactions; $YBa_2Cu_3O_x$, 1010 ^0C < T < 1300 ^oC Y_2BaCuO_5, (211 / green phase) + Liquid phase Y_2BaCuO_5 (green phase)+ Liquid phase 1300 ^oC < T < 1500 ^oC , Y_2O_3 + Liquid Large oriented domains of 123 phase with 211 (green phase) inclusions are formed on subsequent slow cooling. The grains which grow preferentially along ab planes are stacked along the c-direction, and are coupled by low-angle grain boundaries, in these samples. This microstructure is in contrast to small randomly oriented polycrystalline grains obtained by solid-state reaction. The presence of faceted growth interfaces where the 211 volume fraction and particle size decrease abruptly upon being included into the growing 123 grains is showed by quenching studies performed on MTG samples [18]. The 211 phase appears to provide Y into the growing phase of 123. For smaller sizes of the 211 precipitates, and homogenous distribution of the precipitates, the MPMG process is the most widely used melt growth process designed. In this technique, the reaction of solid Y_2O_3 with a liquid phase to form the 211 phase is involved [1]. By taking the powder and crushing and remixing the melt quenched samples, the nonuniform distribution is handled. This powder is pressed into a pellet and subjected to the melt growth. Since the 211 phase grows into coarse grains, the samples should not be held above the peritectic temperature for extended periods. After a short time above the peritectic temperature, it is cooled to just below the peritectic temperature and then slowly cooled in flowing oxygen to room temperature.

In determining the grain size and nature of the grain boundaries, the hold time and cooling rate have a strong influence on the microstructure of the samples in the melt growth techniques. The hold time determines the amount of liquid phase formed for the peritectic recombination. The cooling rate determines the time available for the recombination [1].

3.8.3 Sol-gel Method

Another processing method for bulk Y123 is known as sol-gel synthesis method that involves the chemical and physical processes such as hydrolysis, polymerization, gelation, evaporation and densification and hence, it is a wet chemical multi-step process. This alternate synthetic method forms a precursor to the ceramic mixed metal oxide. The precipitate ideally consists of an intimate (atomic level) mixture of metal hydroxides, such as $Ba(OH)_2$, $Y(OH)_3$ and $Cu(OH)_2$. Since this process uses solution chemistry and results in a gel-like product, it is often called a sol-gel process [19]. This intermediate precursor solid also contains some organic ligands around the metals, such as oxalates or citrates, that serve to keep the metals in solution and help them precipitate together. Hydrated metal nitrates are utilized in a sol-gel route to produce a precursor to $YBa_2Cu_3O_7$, $Y(NO_3)_3 \;\; 6H_2O + 2Ba(NO_3)_2 + 3Cu(NO_3)_2 \;\; 2.5\ H_2O \rightarrow Y(OH)_{3-x} + 2Ba(OH)_{2-y} + 3Cu(OH)_{2-z}$ + (x + y + z)/2 oxalate The oxalate (2 2 4 C O-) ligands will be burned off and the hydroxyl groups will be dehydrated by heating the gel product to high temperatures ($\sim 1000^oC$) in air. With careful attention to temperatures and oxygen content, the product after ligand burn off should consist of a well-mixed set of metal oxide powders, similar to the following equation and it will be converted to $YBa_2Cu_3O_7$ by further high temperature heating [20].

$1/2\ Y_2(CO_3)_3 + 2BaCO_3 + 3Cu\ CO_3 \rightarrow Y_2O_3 + 2BaO + 3CuO \;\; YBa_2Cu_3O_7 - 8CO_2 + 1/2\ O_2$

The complexity of the method is due to its requirements such as the pH, temperature, volume and concentration. The main advantages of this method are better homogenity, higher purity, lower processing temperatures, more uniform phase distribution, smaller grain size, and better morphological control, than obtainable in the conventional ceramic method.

3.8.4 Microwave Processing Method

In this method, to generate thermal energy rapidly, the interaction of the electromagnetic waves (of frequency 2.45 GHz, used in domestic ovens), with a susceptible material which constitutes the starting material is used [20]. CuO is known to be the suscepter material, among the starting materials used for YBCO 123. The main advantages of this technique are:

- reduced reaction time,
- reduced reaction temperature, and
- reduced overall cost.

The reaction time is only a few minutes.The main drawbacks of the technique are:

- post-synthesis quenching,
- uncontrolled heating,
- low availability of microwave-suscepter starting material,
- difficulty with accurate measurement of reaction time.

Generally, a post-annealing in oxygen atmosphere is necessary for obtaining YBCO 123 with good superconducting properties.

Processing of HTSC Thin Films

There are two diffirent procedures: in-situ and ex-situ processes that are used to deposit thin films of HTSC materials on a wide variety of substrates. For both processes, the high-vacuum deposition systems are required. The samples are deposited and processed inside a vacuum chamber and may not require any post processing outside the chamber in in-situ processing technique. On the other hand, ex-situ processing method requires post processing outside the chamber. To obtain superconducting samples, additional heat-treatment is necessary in case of the substrates are not heated during the deposition process that will yield an amorphous material. Generally the in-situ process is preferred [20] due to high uniformity. The thin films come with good control over the growth process. An in-situ deposition process usually uses a deposition system and allows growth of multilayers with precise thickness control, essential for some applications. A drawback of the method is that, it is not suitable for deposition on large area substrates. The ex-situ procedure is simpler and easier to optimize. Good quality HTSC thin films with ex-situ post processing can be obtained. This processing method, is less expensive compared to in-situ processing and it is suitable for growing thick or coated films of superconductors.

3.8.5 Physical and Chemical Deposition Methods

Physical or chemical deposition methods can be used for the deposition of HTSC thin films. The physical deposition techniques include some form of high-energy ion or electron bombardment of the target to release the material for deposition onto substrates. This deposition method includes the techniques such as sputtering, electron beam evaporation and pulsed laser ablation or pulsed laser deposition (PLD).

On the other hand, chemical deposition methods involves chemical vapors reacting at the surface of heated substrates to form a thin film of desired composition. They include techniques such as metal organic decomposition (MOD) and metal organic chemical vapor deposition (MOCVD) [21]. Both of the methods can be tailored for in-situ or ex-situ processing. The sputtering and pulsed laser depositions are the most popular methods used, especially for the in-situ process.

3.9 Influence of Dopants

Information about the chemical requirements for high temperature superconductivity have been provided by the large number of studies all over the world. It is also critically important to have information about the effects of dopants for processing. For many purposes, dopants maybe introduced into high temperature material and they may be substitutional or additional. The studies on various substitutions in oxide superconducting systems have proven to be of great importance [22]. The effects of dopants and impurities depend on their valence, ionic radius, substitutional sites, electronic configuration and solubility. Among the cuprate superconductors, YBCO is one of the most widely studied compound, because of the simplicity of synthesis by solid state reaction, the wide availability of starting materials and the non-toxity of the material compared to the other high temperature superconductors such as Tl and Hg-based oxides. Addition of other elements to YBCO is performed for two reasons:

- To vary the properties and hence provide more information on the possible mechanisms of superconductivity, and
- To improve the physical characteristics such as density, grain texture and ductility.

In the first case, chemical substitution is involved, whereas the second requires that the YBCO ceramic and the impurity metal are seperate and form a composite. Various studies on substitution of different metals (Li, Al, Fe, Co, Ni, Zn,...etc) frequently at copper sites have been reported. To improve the physical characteristics of YBCO, transition metals are widely used.

3.10 Effect of Nickel Dopant

Nickel usually substitutes at the Cu site. It is introduced by mixing NiO with BCO. Reported solubility limits for $YBa_2Cu_{1-x}Ni_xO$, range from x=0.04 to 0.20. Although the orthorhombicity decreases, the symmetry remains orthorhombic. Furthermore, it is reported that the oxygen content remains constant or increases slightly. T_c decreases with x increasing. The exact variation depends on preparation conditions; in some reports the decrease is slow whereas in others a fast initial decrease is seen. High pressure oxygen annealing does not affect the Tc. Ni substitutes exclusively at the Cu(2) site but this may depend on heat treatment; it is found that the ratio d = [proportion of Ni at Cu(1)] / [proportion of Ni at Cu(2)] is small for high annealing temperatures, but increases with decreasing annealing temperatures [13]. The normal state resistivity increases with increasing x. The resistivity temperature coefficient changes sign at $x\sim$ 0.083 as thermopower is sensitive to Ni content resulting to the cuprate underdoped and the thermopower become negetive.

3.10.1 Experimental Preparion of YBCO Powders by Solid State Route

$YBa_2Cu_3O_{7-x}$ powders were synthesized by mixing Y_2O_3 (99.99 %, Sigma Aldrich), $BaCO_3$ (99 %, Sigma-Aldrich) and CuO (98 % Sigma-Aldrich) in a stoichiometric ratio of 1:2:3. Proportional powders were ball-milled in a polyethylene jar with zirconia ball for 24 h and dried. The mixed powders calcined in an opened alumina crucible at different temperatures i.e. 800, 850, 900 and 950 ^{o}C for 12 h under normal air atmosphere. After the calcination process, the powders were reground and sieved for homogeneous distribution [16].

3.10.2 Nano-nickel Powders

Nano nickel powders were commercially obtained from Sigma- Aldrich Company.

3.10.3 Material Incorporation

Well characterized nano Ni particles (50 nm) (0.5 to 3 % wt) were mixed with the high-T_c cuprate superconducting YBCO powders in a controlled way and then pelletized into thick pellets. Nano nickel particles being magnetic destroys the superconducting order locally and thus act as a pinning center. Further, the size of the chosen nickel particles were rounghly 3 order smaller than the micron size grain bounderies of the YBCO. Hence, we avoided any heat treatment after mixing so that the added nickel only got into the grain boundaries. This means that we were able to tailor the grain boundary pinning by nano nickel. That first reduced the J_c of the grain boundary junctions and as the concetration was increased, the J_c increased.

Methodological Assumptions

It was assumed that the nano Ni particles only went into the grains boundaries of YBCO and not into the grains thorough grinding of many cycles. This would give a very uniform Ni dispersion in YBCO powder.

Concept Clarification

Nano Ni particle are used as pinning centers in a YBCO superconductor. The YBCO superconductor is highly granular and has a hierarchy of weaklinks including grain boundaries. As the nano Ni particles are thoroughly dispersed in the YBCO powders by grinding only and as no heat treatment was done, it is believed that the nano Ni only enter the grain boundaries of the YBCO powders when pelletized. These nano Ni particles can destroy superconductivity locally in the grain bounderies and act as strong pinning centers. However, in a dilute disperion, nano Ni being magnetic can also reduce the grain boundary of Josephson junction critical current density which should actually reduce the levitation efficiency. However, as the concetration of nano Ni is increased progressively at some stage, pinning effects should dominate and levitation efficiency should increase.

References

[1] M. Murakami , A. Goyal, W. Wong-Ng, J. *Driscoll, Processing of High Temperature Superconductors* ISBN: 978-1-118-40595-6 Apr (2012).

[2] H.W. Weber and G.W. Crabtree, A.V. Narlikar, ed., *Studies of High Temperature Superconductor*, Nova Science Publishers, New York 9:37 .12 (1992).

[3] S. Jin and J. Min, *Met and Mat. Society*. Vol 43, 3, 712 (1991).

[4] J. B. Torrance, Y. Tokura, 'l A. I. Nazzal, A. Bezinge, T. C. Huang, and S. S. P. Parkin, *Phy. Rev.* lett 61, No. 9, 7 (1988).

[5] A. K. Bandyopadhyay, R. Jabra and J. Phalippou, *J. Mater. Sci.* 8, 1464 (1989).

[6] G. Sinha, K. Adhikary and S. Chaudhuri, *Proc. Natl. Conf. on Nano-Science and technology, J. U. Kolkata (India)*, January, (2005).

[7] G. Wrinkler, *Crystallography, Chemistry and Technology of Ferrites in Magnetic Properties of Materials*, J. Smit, Ed., p. 20, McGraw-Hill, London, UK, (1971).

[8] J. Liu, H. He, X. Jin, Z. Hao, and Z.Hu, *Materials Research Bulletin*. vol 36, no 13-14, 23572363 (2001).

[9] M. Pardavi-Horvath, *J. of Mag. and Mag. Materials*. vol 215, 171183, (2000).

[10] N. Mo, Y. Y. Song, and C. E. Patton, *J. of Appl. Phys.* vol 97, no. 9, 19 (2005).

[11] J. Giri, P. Pradhan, T. Sriharsha, and D. Bahadur, *J. of Appl. Phys.* vol 97, no. 10, 13 (2005).

[12] G. W. Cave, C. L. Raston and J. L. Scott,*Chem. Commun.* 2159. (2001). G. Rothenberg, A. P. Downie, C.L Raston, J. L Scott,*J. Am. Chem. Soc.* 123, 8701 (2001).

[13] D. Braga, F.Grepioni and C. Angew, *Chem. Int. Ed.* 43, 4002 (2004).

[14] S. Jin, T. H. Tiefel, R. C. Sherwood, M. E. Davis, R. B. van Dover, G. W. Kammlott, R. A. Fastnacht, and H. D. Keith, *Appl. Phys.* Lett 52, 2074 (1988).

[15] Z. Lian, Z. Pingxiang, J. Ping, W. Keguang, W. Jingrong and W. Xlaozu, *Supercond. Sci. Technol.* 3, 4-92 (1990).

[16] T. Troczynski and Q. Yang, *U.S. Pat.* No. 6, 284-682 (2001).

[17] T. Olding, M. Sayer and D. Barrow, *Thin. Solid. Films.* 398-399, 581-586 (2001)

[18] J. G. P. Binner and I. A. H. Al-Dawery, *Supercond. Sci. Technol.* 11, 449 (1998).

[19] A. W. Czanderna, C. J. Powell, T. E. Madey, D. M. Hercules, J. T. YatesJr, *Specimen Handling, Preparation, and Treatments in Surface Characterization (Physical and Chemical Methods for Thin-Film Deposition and Epitaxial Growth)* pp 239-293 book series (MOSC, vol 4)

[20] A. H. Salama, M. E. Hofy, Y. S. Rammah and M. Elkhatib, *Adv. Nat. Sci. Nanosci. Nanotechnol.* 7, 015011 (2016).

[21] P. Prayoonphokkharat, S. Jiansirisomboon, A.Watcharapasorn, *J. micro.* Soc 5 (1-2), 63-66 (2012).

[22] P. Wei and Z. Qing Qi , *Physica.* C 183, 32-38 (1991).

4 CHAPTER FOUR

4.1 Measurements and Data Collection

Sample characterisation requires powerful tools and techniques which can guarantee unambiguous and results that are easy to interpret. We have employed SEM, FTIR, XRD, PPMS/VSM and NRMA to probe Ni-YBCO powder sample. XRD was used to characterize crystal structre of the sample. The SEM and FTIR have been used to investigate the microstructure and topography. PPMS/VSM was used to invetigate the magnetic properties whereas NRMA has been used to investigate electromagnetic response. In this chapter, we discuss the working principles of each of the piece of equipment and techniques employed.

4.2 Scanning Electron Microscopy (SEM)

SEM is a pertinent tool for characterising the microstructure of a sample because it affords an extremely better resolution compared to the optical microscope. It basically consists of two main components namely: the electron console and the electron column [1]. The electron console houses adjustable knobs and switches which are responsible in regulating and adjusting accelerating voltage, magnification, filament current , contrast and brightness. The sole purpose of an electron column is to generate, focus and scan the electron beam on the specimen [2]. The electrons are produced by thermionic emission where a filament made of a thin tungsten wire is heated to a temperature of about 2800 K and then flown to an anode by applying a positive accelarating voltage (1 to 30 kV) [2]. Electron gun can also be of lantanum hexaboride (LaB_6), field emission or Schottky-emission [3]. When the electron beam interacts with the specimen, several signal types such as secondary electrons, backscattered electrons, x-ray, Auger electrons and cathadoluminescence are realised. It is the secondary electrons and backscattered electrons which are often used for SEM image generation. Secondary electrons (SE) have energies of less than 50 eV and are formed by inelastic interactions when electron beam impinges electric field of a specimen while backscattered electrons are formed through elastic interactions which occur between electron beam and the nucleus of the specimen [3].

To create a SEM image, scanning/rastering of the sample surface is done using electron beam which emanate from the electron gun (see Figure 15).

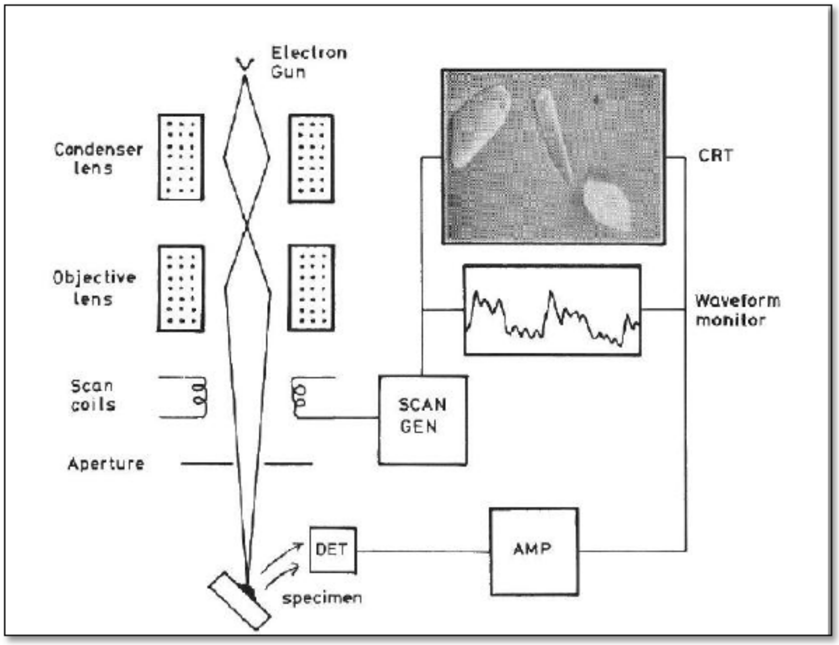

Figure 15: A schematic block diagram of SEM [4]

More importantly, each position or point in the sample surface will uniquely emit electrons which are sensed by electron detector. Subsequently, by using a synchronized cathode ray oscilloscope (CRT) or a computer, the morphology of the sample can be observed [4].

In this work, Ni-YBCO powder sample was mounted on an aluminium stub using a carbon tape and then observed under JEOL JSM-7500F (Figure 16) field-emission scanning electron microscope (FE-SEM).

Figure 16: A picture of SEM used in this work, JEOL JSM-7500F.

4.3 Non-Resonant Microwave Absorption Technique (NRMA)

Non-resonant radio frequency/microwave absorption (NRMA) or magnetically modulated microwave absorption (MMMA) technique is a highly sensitive, contactless and non-destructive technique used for detection and characterisation of superconductivity even in a sample containing iota traces of the superconducting phase [5,6]. The absorption comes from a contribution of three magnetic fields namely: the sweep magnetic field, microwave magnetic field and modulation of external field. This technique is related to important fundamental superconducting parameters and manifestations such as critical current density through which critical field H* and penetration depth λ are determined [7, 8], irreversibility line [9], vortex dynamics state [10] and anomalous hysteresis [11] among many more. Besides, it can be used to distinguish between weak link superconductivity and bulk superconductivity [12]. The aforementioned physical and technical relevance of this technique justifies why it is a common means of characterising superconducting materials hence its use in this study.

The technique was discovered by Bhat et al., as mentioned from [13] during an attempt to study the EPR of Cu^{2+} in ceramic sample of $YBa_2Cu_3O_{7x}$ in which a non-resonant microwave line shape signal centered around zero magnetic field (see Figure 17) was observed. The signal was reported by many authors afterwards [14-18].

The signal has been found to have the following fascinating characteristics namely:

- It occurs below the transition temperature T_c i.e in the superconducting state [13],
- It is very sensitive to temperature variation, magnetic field modulation amplitude and microwave power [19],
- It has different characteristics depending on the nature of the sample whether a single crystal, polycrystalline or thin films [20, 21], and
- It depends on sample surface area, shape and particle size [22].

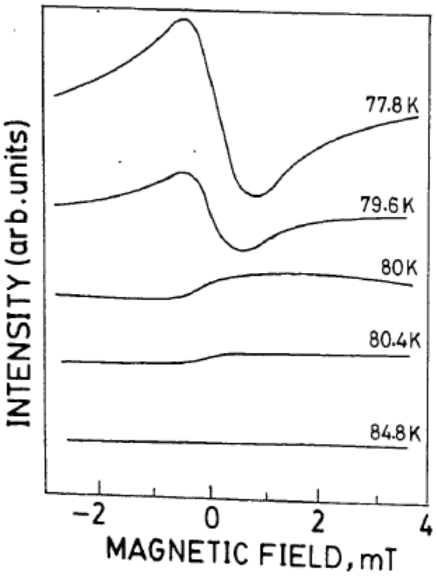

Figure 17: Line shape of YBCO superconductor sample [23].

The method involves the use of an electron paramagnetic resonance (EPR) spectrometer to record the 'non-resonant' response of the superconductors to electromagnetic radiation as a function of temperature and magnetic field. It is of essence to note that an EPR spectrometer was initially designed to measure the microwave absorption due to magnetic dipolar transition which occurs if the energy difference between two spin levels of the compound, subjected to a variable DC field is equal to the microwave frequency [23]. This is explained in the electron spin resonance spectroscopy section.

In this work, EPR was used purely as a sensitive microwave device. Figure 18, shows a block diagram illustrating how microwave measurements are obtained in an ESR spectrometer. The klystron (monochromatic source) produces microwaves of 200 mW. Then the microwave radiation transferred to an attenuator by means of a rectangular, hollow wave guide. Since microwave source cannot be varied easily, its power level is changed to avoid saturation [24, 25].The attenuator is capable of reducing the microwave power of 200 mW by a factor between 1 and 10^6 hence the power reaching the sample at the cavity is precisely controlled. The circulator then receives the attenuated radiations via the wave guide and forces it into the resonator/cavity. It uniquely directs all the microwaves coming from the attenuator to the cavity and those from the cavity to the detector.

The work of the iris shown on the magnetic system part is to tune amount of radiation reflected back out of the cavity. The reflected radiation from the cavity is channelled to the detector diode which converts the microwave power to an electric current. At the detector diode, some radiation may get reflected back to the circulator where they are directed to the wedge and converted into heat [24, 25].

To ensure that the detector works at a constant current, the reference arm supplies it with extra microwave power. There is also a phase shifter to ensure that the reference arm microwaves are in phase with the reflected signal microwaves when the two signals combine at the detector diode [24]. The computer is used for two reasons namely: for data acquisitions and to excute commands in an EPR spectrometer.

In addition to the above components of EPR, the cryostat is compulsory for low temperature measurements. The cryostat neccessitates the temperature of the sample to be swept between 3.8 K and 300 K. In this work, a superconducting sample to be measured is put inside a quartz tube and located in the cavity at a maximum of the magnetic component of microwave field perpendicular to external stationary magnetic field. The cavity is located between the poles of a magnet. The external field is modulated at 100 kHz frequency and lock-in-detection is applied. With appropriate modulation amplitude, the detected signal gives a derivative of the microwave power dissipated in the cavity.

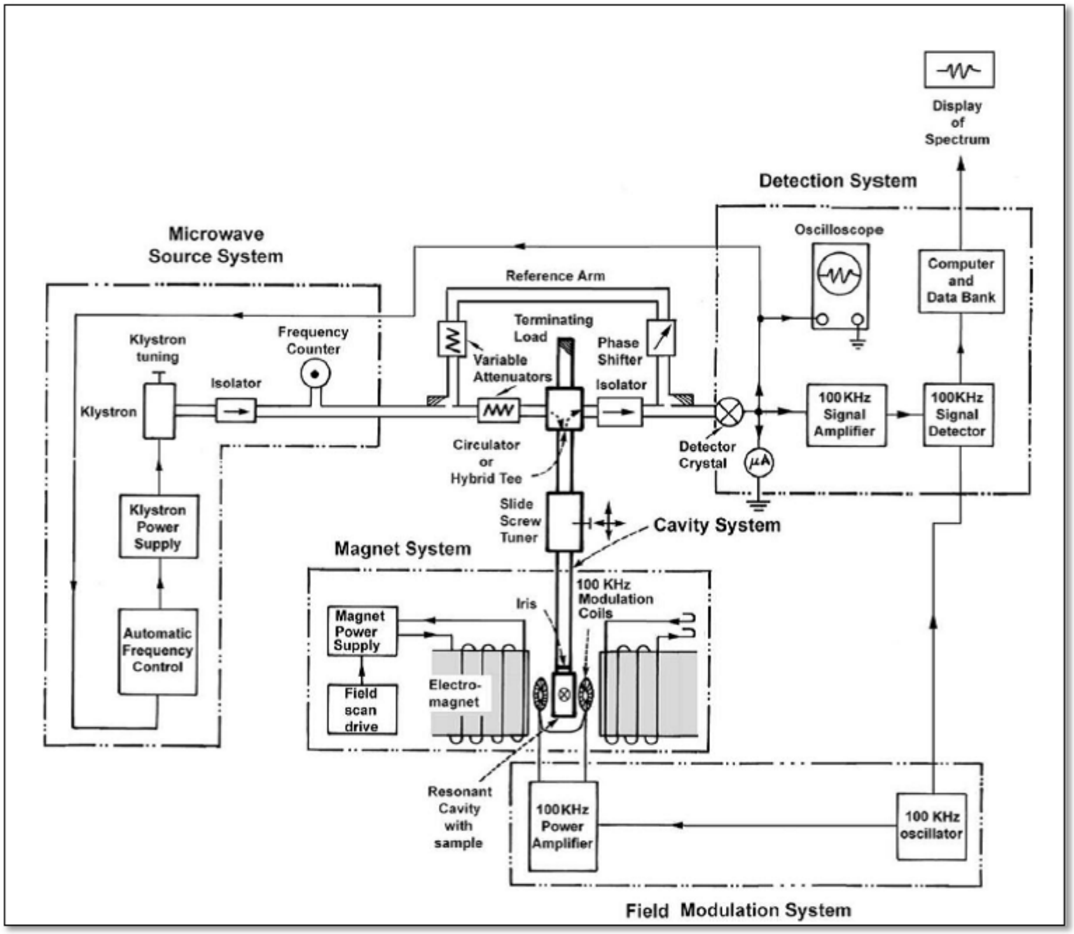

Figure 18: A schematic block diagram of EPR spectrometer [26].

In this thesis, we have used a Bruker EXM spectrometer (Figure 19) equipped with an Oxford ESR 910 continuous flow cryostat operating at microwave frequency of 9.45 GHz to investigate electromagnetic radiation response of Ni-YBCO powder superconductor. We report that indeed NRMA well resolved lineshape was obtained. Effects of change of temperature, field modulation amplitude and microwave power on NRMA lineshape have been investigated and presented in chapter five.

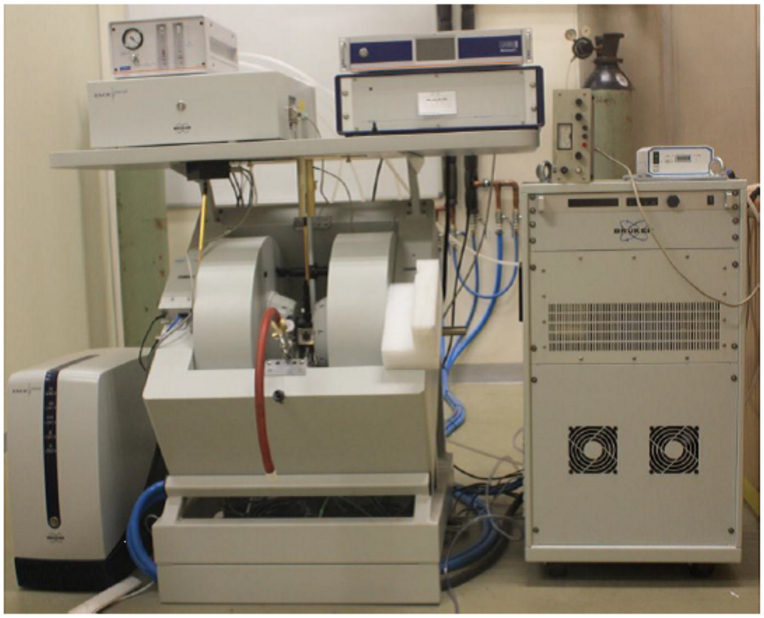

Figure 19: A picture of EPR used in this work, Bruker EXM spectrometer.

4.4 X-Ray Diffraction (XRD) Measurements

A typical powder XRD instrument consist of four main components which are X-ray source, specimen stage, receiving optics and X-ray detector as shown in Figure 20. The source and detector with its associated optics lie on the circumference of focussing circle and the sample stage at the centre of the circle as shown in Figure 21, and the picture of XRD is shown in Figure 22. The angle between the plane of the specimen and the X-ray source is θ (Bragg's angle) and the angle between the projection of X-rays and the detector is 2θ. For the XRD analysis, fine powder samples can be mounted on the sample holder and the powder which is assumed to consist of randomly oriented crystallites [27]. When a beam of X-ray is incident on the sample, X-rays are scattered by each atom in the sample. If the scattered beams are in phase, these interfere constructively and one gets the intensity maximum at that particular angle. The atomic planes from where the X-rays are scattered are referred to as reflecting planes.

After recording the X-ray diffraction pattern, the first step involves the indexing of XRD peaks. The indexing means assigning the correct Miller indices to each peak of the

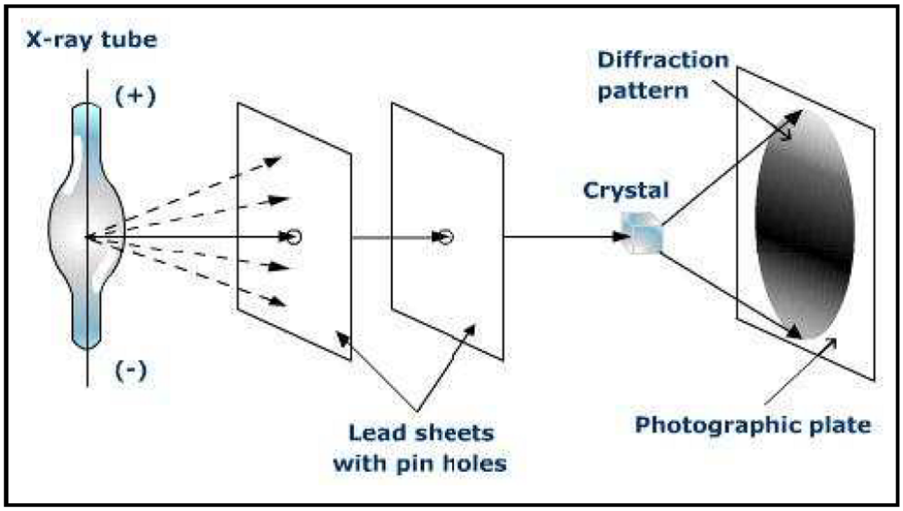

Figure 20: Schematic of the X-ray diffraction by a crystal [27].

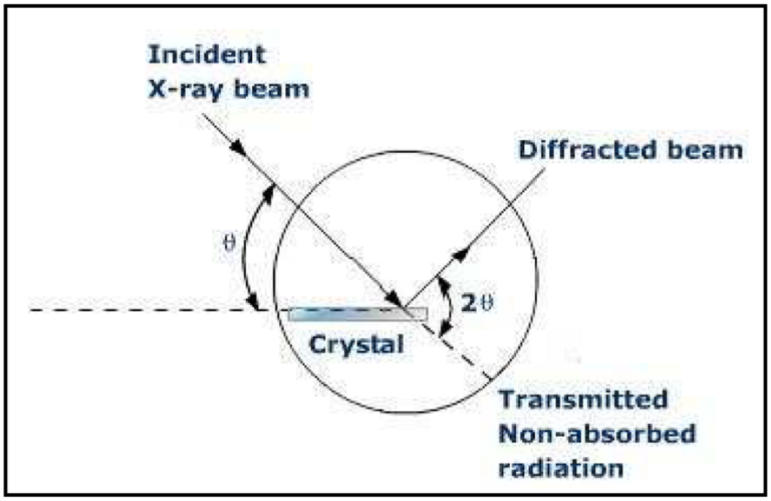

Figure 21: A schematic representation of X-ray diffraction [28].

diffraction pattern [28].

There are three main methods for indexing of X-ray diffraction pattern:

- Comparing the measured XRD pattern with the standard database (JCPDS-cards)
- Analytical methods
- Graphical methods.

X-ray diffraction (XRD) is used to check the monophasic nature of the samples. XRD is the most essential technique to investigate the structural aspects of the material. It helps to identify the presence of different phases, including the impurities and unreacted components in a given material. Such information provides a very useful guideline towards modification of synthesis procedures [29]. Analysis of XRD data gives the unit cell parameters of the system. In the present study, X-ray diffraction was extensively used to investigate the course of the reaction during the synthesis of the samples and to change the heat treatment procedures accordingly.

Figure 22: A picture of typical XRD instrument.

4.4.1 Important Parameters from XRD Data

Analysis of XRD data provides some very useful information about the important parameters of the sample [27]. Some of them are discussed below.

- Unit cell volume

  X-ray diffraction provides us the lattice cell parameters of crystal unit cell and therefore its volume.

- Volume of a cubic unit cell,

$$V = a^3 \tag{4.1}$$

(where a=b=c)

- volume of a tetragonal unit cell,

$$V = a^2 c \tag{4.2}$$

(where $a = b$) and

- Volume of a hexagonal unit cell,

$$\mathtt{V} = \sqrt{3}/2a^2c \tag{4.3}$$

where a, b, and c are the unit cell dimensions called unit cell or lattice parameters.

- X-ray density:

X-ray density=Weight of the atoms in unit cell/volume of unit cell

- Porosity: By comparing X-ray density to that of macroscopic density of a pressed and sintered pellet one can calculate the percent porosity in the compact. Porosity can be evaluated by using the following equation [28],

$$\mathtt{P} = (1 - \mathtt{d}/\rho) \times 100\% \tag{4.4}$$

where, d is the bulk density of the material can be calculated by mass/volume of the samples in pellet form or by Archimedes principle.

- Particle size: When the particle size of the individual crystal is less than 100 Å^3, the term particle size is used. Crystals of this size range cause broadening of the Bragg peak, the extent of the broadening is given by

$$\mathtt{B} = 0.89\lambda/\beta\cos\theta \tag{4.5}$$

where, B = broadening of the diffraction line (Bragg peak) measured at full width at half of its maximum intensity (FWHM) (in radian), λ=wavelength of target and β=diameter of the crystal particle

4.5 Fourier Transform Infrared Spectroscopy (FTIR)

Infrared spectroscopy is non destructive technique for material analysis and has been used in the laboratory for over seventy years. Infrared absorption spectroscopy is the study of interaction of infrared radiation with matter as a function of photon frequency [29,30]. Fourier Transform Infrared Spectroscopy (FTIR) provides specific information about the vibration and rotation of the chemical bonding and molecular structures, making it useful for analyzing organic materials and certain inorganic materials. An infrared spectrum represents a fingerprint of a sample with absorption peaks which correspond to the frequencies of vibrations between the bonds of the atoms making up the material. Because each different material is a unique combination of atoms, no two compounds produce the exact same infrared spectrum. Therefore, infrared spectroscopy can result in a positive identification (qualitative analysis) of every different kind of material [29]. In addition, the size of the peaks in the spectrum is a direct indication of the amount of material present. With modern software algorithms, infrared spectroscopy is an excellent tool for quantitative analysis.

The IR region is commonly divided into three smaller areas: near-IR (400-10 cm^{-1}), mid-IR (4000-400 cm^{-1}), and far-IR (14000-4000 cm^{-1}). Infrared photons have enough energy to cause groups of atoms to vibrate with respect to the bonds that connect them. Like electronic transitions, these vibrational transitions correspond to distinct energies, and molecules absorb infrared radiation only at certain wavelengths and frequencies. Chemical bonds vibrate at characteristic frequencies,and when exposed to infrared radiation, they absorb the radiation at frequencies that match their vibration modes. Measuring the radiation abs frequency produces a spectrum that can be used to identify functional groups and compounds. Some impurities produce their own characteristic bands in infrared region. Spectral measurements of these bands are used to determine concetration of the impurities and their bonding with the host materials. Identification of the measured interferogram signal can not be interpreted directly hence, a means of decoding the individual frequencies is required. This can be accomplished via a well-known mathematical technique called the transformation performed by the computer which then presents the user with the desired spectral information for analysis.

4.5.1 Sample Analysis Process

There are three basic spectrometer components in an FTIR system: a radiation source, an interferometer, and a detector.

Interferometer divides radiant beams, generates an optical path difference between the beams, and then recombines them in order to produce repetitive interference signals measured as a function of optical path difference by a detector [31]. As its name implies, the interferometer produces interference signals, which contain infrared spectral information generated after passing through a sample. The most commonly used interferometer is a Michelson interferometer. It consists of three active components: a moving mirror, a fixed mirror, and a beam splitter (Figure 23).

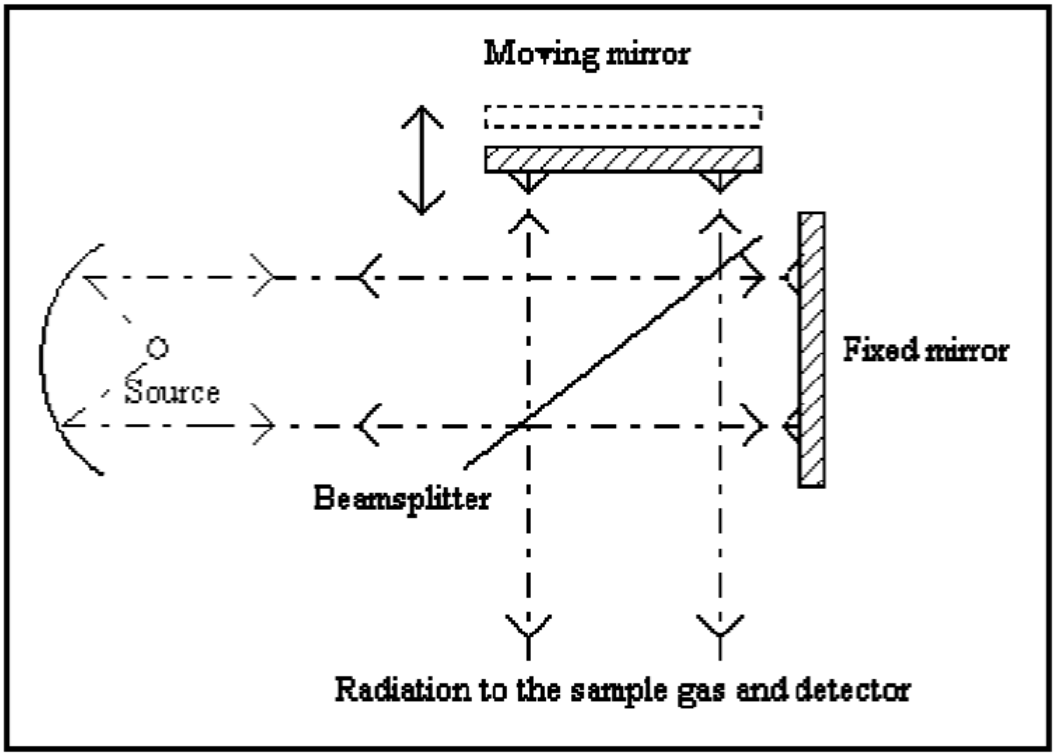

Figure 23: Michelson interferometer [30].

The two mirrors are perpendicular to each other. The beam splitter is a semi-reflecting device and is often made by depositing a thin film of germanium onto a flat KBr substrate. Radiation from the broadband IR source is collimated and directed into the interferometer, and impinges on the beam splitter.

4.5.2 Sample Preparation

IR spectra can be measured using liquid, solid, or gaseous samples that are placed in the beam of infrared light. A drop of a liquid can be placed as a thin film between two salt plates made of NaCl or KBr, which are transparent to infrared light at most important frequencies. A solid can be ground with KBr and pressed into a disk that is placed in the light beam. Alternatively, a solid sample can be ground into a pasty mull with paraffin oil [4]. As with a liquid, the mull is placed between two salt plates. Solids can also be dissolved in common solvents such as CH_2Cl_2, CCl_4, or CS_2 that do not have absorptions in the areas of interest. Gases are placed in a longer cell with polished salt windows. These gas cells often contain mirrors that reflect the beam through the cell several times for stronger absorption.

4.5.3 Working of an FTIR Spectrometer

The basic instrument design is quite simple. Figure 24 (a) illustrates the schematic diagram and Figure 24 (b) a typical FTIR spectrometer

The normal instrumental functions are as follows:

- The Source: Infrared energy is emitted from a glowing black-body source. This beam passes through an aperture which controls the amount of energy presented to the sample (and, ultimately, to the detector).
- The Interferometer: The beam enters the interferometer where the spectral encoding takes place. The resulting interferogram signal then exits the interferometer.
- The Sample: The beam enters the sample compartment where it is transmitted

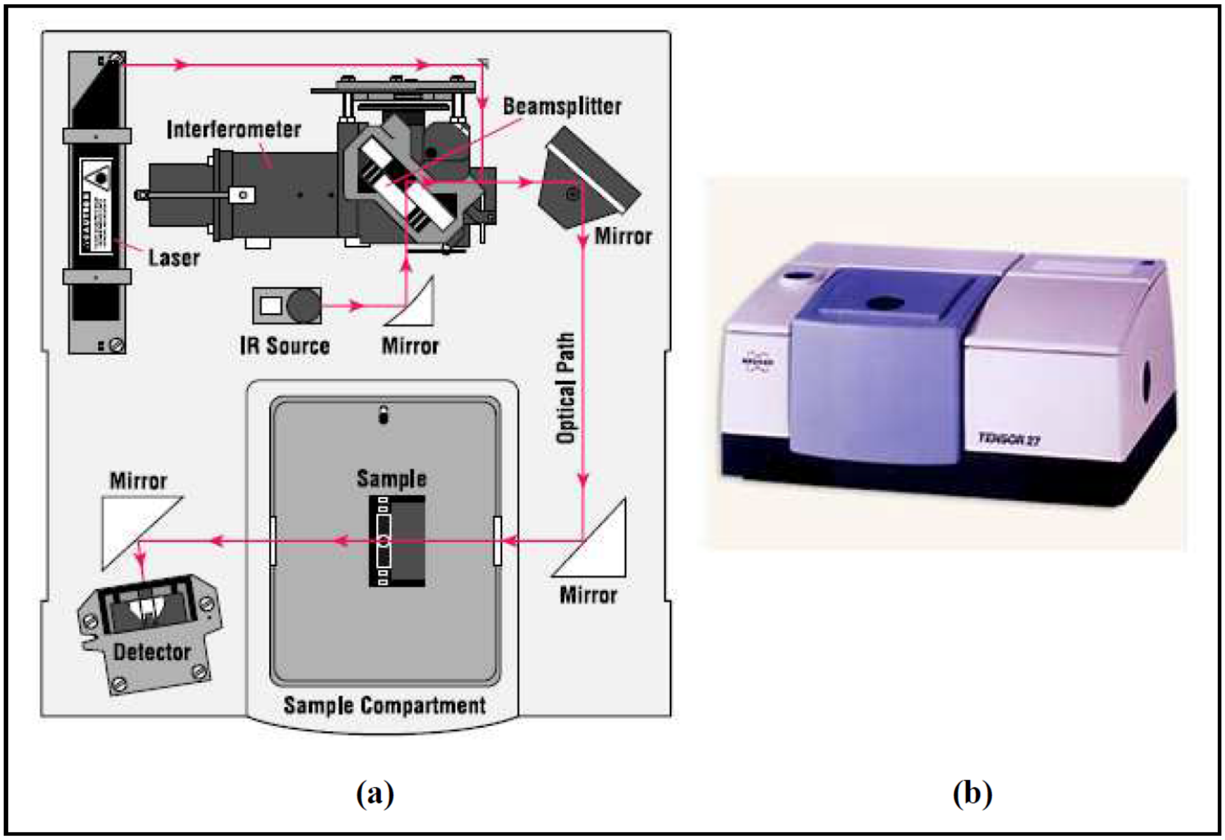

Figure 24: (a) Schematic diagram of FTIR and (b) FTIR instrument [31].

through or reflected off the surface of the sample, depending on the type of analysis being accomplished. This is where specific frequencies of energy, which are uniquely characteristic of the sample, are absorbed.

- The Detector: The beam finally passes into the detector for final measurement. The detectors used are specially designed to measure the special interferogram signal.
- The Computer: The measured signal is digitized and sent to the computer where the Fourier transformation takes place. The final infrared spectrum is then presented to the user for interpretation and any further manipulation.

4.6 Vibrating Sample Magnetometer (VSM)

Vibrating Sample Magnetometry (VSM) is a measurement technique which is used to determine the magnetic moment of a sample with very high precision [32].

4.6.1 Measurement Principle

VSM is based on Faraday's law which states that an electromagnetic force is generated in a coil when there is a change in flux through the coil [33]. In the measurement setup, a magnetic sample is moving in the proximity of two pickup coils as indicated in Figure 25.

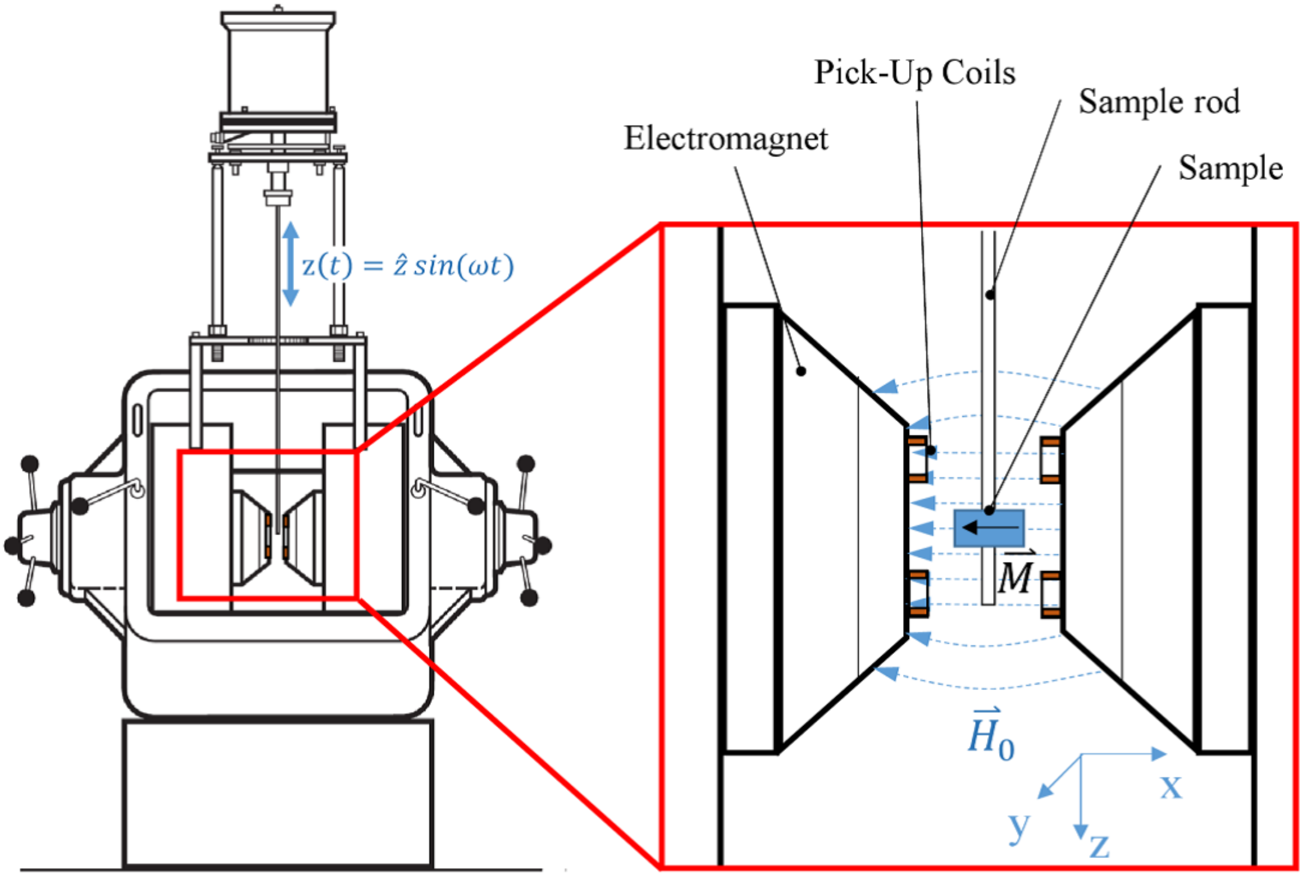

Figure 25: Schematic representation of a VSM [32].

The oscillator provides a sinusoidal signal that is translated by the transducer assembly into a vertical vibration. The sample which is fixed to the sample rod vibrates with a given frequency and amplitude (60 to 80 Hz and 1 mm, respectively). It is centered between the two pole pieces of an electromagnet that generates a magnetic field $\vec{H}_0$ of high homogeneity. Field strengths in the range of 10^6 A/m are commonly possible with laboratory VSM systems. Stationary pickup coils are mounted on the poles of the electromagnet [32]. Their symmetry center coincides with the magnetic center of the static sample. Hence, the change in magnetic flux originating from the vertical movement of the magnetized sample induces a voltage

$$\mathtt{U_{ind}} = -\delta\Phi/\delta\mathtt{t} \tag{4.6}$$

where Φ is the magnetic flux. For n_c pickup coils with a flat surface A and n_ω windings, equation 4.6 gives

$$\mathtt{U_{ind}} = \sum_{\mathtt{n_c}} \sum_{\mathtt{n}_\omega} \int_{\mathtt{A}} (\delta\mathtt{B}/\delta\mathtt{t})\mathtt{dA} \tag{4.7}$$

When we bring the sample into the homogeneous field $\vec{H}$ along the x axis, it will be magnetized along the direction of the field, resulting in a magnetic moment $\vec{m}$ of the sample. Then, the sample will be moved periodically relative to the pickup coils.

4.6.2 Hysteresis

With a VSM, the magnetic moment of a sample as a function of the external magnetic field strength can be measured. Figure 26, shows (schematically) a typical result of such a measurement.The demagnetized sample $\vec{m} = \vec{0}$ is firstly magnetized to saturation in an applied field.

Indicated are the two commonly used parameters initial permeability μ_i, and maximum permeability μ_{max} , defined in terms of a ratio of magnetic flux to field strength B/H. Permeability is not the slope of the virgin curve itself, but the slope of a line between the origin and a particular point on the curve (e.g. the upper inflection point before saturation for μ_{max}).

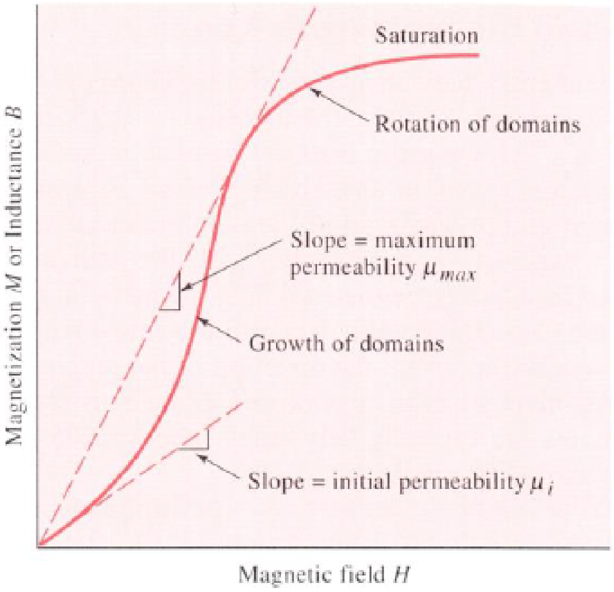

Figure 26: VSM Virgin curve [35].

Increasing and decreasing the external field from the demagnetized state to positive saturation to negative saturation and back gives a ferromagnetic hysteresis loop, which is shown in Figure 27.

Here, the predominant, underlying mechanisms for each region are indicated [34]. The region of highest permeability is governed by domain wall motion whereas magnetization rotation occurs rather at higher magnetic fields. When the applied field is reduced to zero the remanent magnetization M_r remains. A magnetic field of opposite direction called coercivity field H_c is needed to macroscopically demagnetize the sample.

Thus, the hysteresis loop contains important information about the magnetic properties of the sample. Characteristic quantities include the saturation magnetization M_s, the remanent magnetization M_r, the coercivity field H_c, permeability μ and the dissipated energy that is necessary to magnetize the sample in the opposite direction [34]. The dissipated energy can be calculated from the area that is included by the hysteresis loop.

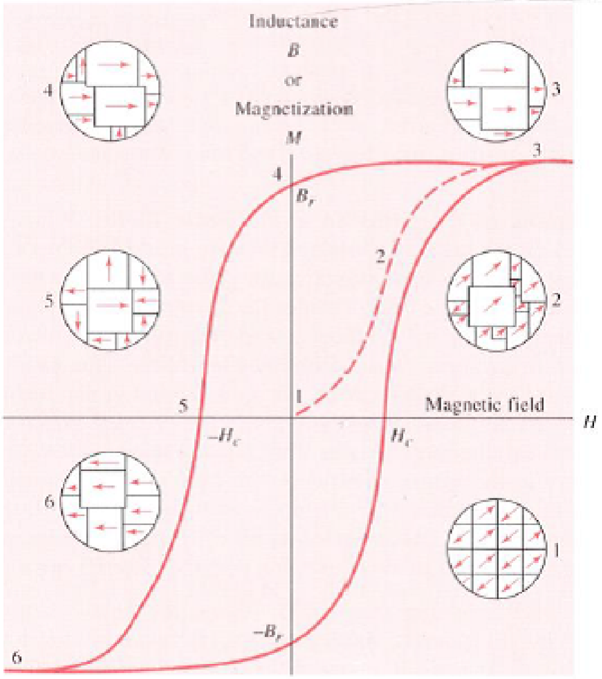

Figure 27: Hysteresis loop of a ferromagnetic material [35].

References

[1] H. Schatten, J. B. Pawley, *Biological Low-Voltage Scanning Electron Microscopy, Springer*, 61 (2007).

[2] G. I. Goldstein, D. E. Newbury, P. Echlin, D. C. Joy, C. Fiori, E. Lifshin,*Scanning electron microscopy and x-ray microanalysis, New York: Plenum Press*, (1981).

[3] T. E. Everhart, R. F. M. Thornley, *J. of Scient. Instrum.* 37, 246 (1960).

[4] V. V. Srinivasu, B. Thomas, M.S. Hegde and S.V. Bhat, *J. Appl. Phys.* 75, 4131 (1994).

[5] M. Stalder, G. Stefanicki, M. Warden, A.M. Portis and F. Waldner, *Physica* C 659, 153-155 (1988).

[6] V. V. Srinivasu, B. Thomas, B. Vasanthacharya, M.S. Hedge and S.V. Bhat, *Solid state Commun.* 79, 713 (1991).

[7] N. Y. Panarina, Y.I. Talanov, T.S. Shaposhnikova, N.R. Beysengulov and E. Vavilova,*Phys. Rev.* B 81, 224509 (2010).

[8] K. I. Itoh, A. Hashizume, H. Kohmoto, M. Matsuo, T. Endo and M. Mukaida, *Physica.* C 477, 357- 360 (2001).

[9] G. K. Padam, N.K. Arora and S.N. Ekbote, *Mat. Chem. and Phys.* 123, 752 (2010).

[10] S. V. Bhat and A. Bull, *Mater. Sci.* 17, 1271 (1994).

[11] S. V. Bhat, P. Panguly and C.N.R. Rao,*Pramana J. Phys.* 28, 425 (1987).

[12] R. Dunny, J. Hautala, S. Ducharme, B. Lee, O.G. Symko, P.C. Taylor, D.J. Zheng and J.A. Xu, *Phys. Rev.* B 36, 2361 (1987).

[13] J. Stankowski, P.K. Kahol, N.S. Dalal and J.S. Moodera, *Phys. Rev.* B 36, 7126 (1987).

[14] K. Khachaturyan, E.R. Weber, P. Tejedor, A.M. Stacy and A.M. Portis, *Phys. Rev.* B 36, 8309 (1987).

[15] C. Rettori, D. Davidov, I. Belaish and I. Felner, *Phys. Rev.* B 36, 4028 (1987).

[16] M.D. Sasty, A.G.I. Dalvo, Y. Babu, R.M. Kadam, J.V. Yakhmi and R.M. Lyer, *Nature.* 330, 49-51 (1987).

[17] M. Bonvalot, M. Puri and L. Kevan, *J. Chem. Soc. Faraday. Trans.* 88, 2387 (1992).

[18] B. Czyzak, *Supercond. Sci. Technol.* 9 , 149 (1996).

[19] L. Ji, M.S. Rzchowski, N. Anand and M. Tinkham, *Phys. Rev.* B 47, 470 (1993).

[20] M. Puri, J.T. Masiakowski, S. Marrelli, J. Bear and L. Kevan, *J. Phys. Chem.* 94, 6094 (1990).

[21] D. Shantlel, H.A.K. Nidda, B.Y. Shapiro, B. Bogoslavsky, B. Rosenstein, I. Shapiro and Tamegei, *Physica.* C 470, 1937 (2010).

[22] R.E. Gareth, B.S. David, S. Eaton, T. Ralpha and Weber *Quantitative EPR, Springer, New York, USA*, (2010).

[23] http://www.auburn.edu/ duinedu/epr/2-pracaspects.pdf, Practical aspects (accessed on 30 January 2016).

[24] J. Weil and J. Bolton, *Electron Paramagnetic Resonance, 2nd ed., J. Wiley, USA*, (2007).

[25] R. P. W. Scott, *Thermal Analysis Book 5.*

[26] J. Smith, H. P. J. Wijn, Ferrites, Philips, Eindhoven, (1959).

[27] J. I. Goldstein, H. Yakowitz, *Practical Scanning Electron Microscopy, Plenum Press*,(1977).

[28] D. R. Lide, ed., *CRC Handbook of Chemistry and Physics*, 75th ed., Boca Raton,FL: CRC Press, 9-79, (1994).

[29] R. M. Silverstein, G. C. Bassler, T. C. Morrill, *Spectrometric Identification of Organic Compounds*, 4th ed., New York: Wiley, 166.(1981).

[30] *IUPAC Compendium of Chemical Terminology*, 2nd Edition, (1997).

[31] M. E. Brown, *Introduction to Thermal Analysis: Techniques and Applications, Springer*,(2001).

[32] Lake Shore Cryotronics, Inc. Users Manual 7300 Series VSM System. http://www.lakeshore.com/ObsoleteAndResearchDocs/7300 Manual.pdf, 2001.

[33] G. J. Bowden, *Detection Coil System for Vibrating Sample Magnetometers 1972: CSIRO Division of Applied Physics, National Standards Laboratory, University Grounds, Chippendale, NSW, Australia*, 2008.

[34] B.D. Cullity, C.D. Graham, *Introduction to Magnetic Materials. John Wiley & Sons, New Jersey*, 2009.

[35] D. R. Askeland, *The Science and Engineering of Materials. International Thomson Publishing*, 3rd ed., 1994.

5 CHAPTER FIVE

5.1 Non-resonant Microwave Absorption in Nanonickel added YBCO Powders: Observation of Multiple Phase Reversals.

5.1.1 Introduction

Since the discovery of the Non-resonant Microwave and RF Absorption (NRMA) in high-T_c superconductors [1-6], this phenomenon has turned into a powerful experimental tool to study superconducting materials. NRMA has been used to assess the quality of YBCO thin films [7], understand the granularity and effective medium effects [8], anisotropy effects in single crystals of Bi-2212 [9], hysteretic and non-hysteretic Josephson junctions [10], boundary and shielding effects in superconductors [11], evaluation of structure and lineshapes in Iron Pnictide superconductors [12], Surface barrier effects [13], to detect superconducting phases [14], study of small size superconducting samples down to nano scale [15], Paramagnetic Meissneer effect (PME) [16]. The loss mechanisms essentially narrow down to (1) microwave driven fluxon loss [7,17], which increases with increasing field and (2) suppression of currents in weaklinks and then breaking of weaklinks, increasing the normal fraction and thereby giving a loss that increases with increasing field [18]. In both cases one would have a minimum of absorption at zero field and then increases with increase of field. In the case of NRMA, the DC field dependent absorption is modulated by a small modulating AC field which then leads to a derivative of absorption (signal proportional to dP/dH, where P is the power absorbed and H is the magnetic field). The zero crossing of derivative absorption either should correspond to the minimum or maximum of absorption. To identify whether the zero crossing of derivative absorption is a minimum or maximum, we compare the phase of the signal with that of the ESR signal. In a resonant absorption signal, the absorption is maximum at the resonant field and then decreases off resonance field. Therefore when the NRMA signal is opposite in phase with the regular resonant absorption signal, then the NRMA signal zero crossing corresponds to the minimum of the absorption and is known as normal NRMA. When the NRMA signal is in phase with the ESR signal, then the zero crossing of NRMA signal corresponds to a maximum of absorption and is known as anomalous NRMA. However in granular superconductors and YBCO powders (where interparticle weaklinks dominate) there are intriguing reports of the observation of a cross over from normal to anomalous NRMA either as a function of temperature [8] or as a function of RF power in YBCO powders [10]. This cross over is also known as phase reversal of NRMA signal as compared with the standard resonance signal. Such 'phase reversal' is usually associated with granularity and the nature of weaklinks [9, 10]. Particularly the powder sample of superconducting materials is very interesting as there are particle-particle weaklinks. One can then tune these inter particle weaklinks by adding ferromagnetic nanoparticles into superconducting powders such that one may get several of such inter particle weaklinks turned into π-junctions. As the critical current dependence on applied field is different from normal junctions, then one would expect that this would reflect in the NRMA as well.

We then carefully prepared nano nickel particles added (a nominal 2 wt%)YBCO superconducting powders and did a systematic study of NRMA in these powders. As these powders are expected to have both normal and -junctions due to YBCO-nano nickel-YBCO inter particle weaklinks, and effectively 0- JJs [19] one would expect 'phase reversal' of NRMA as functions of temperature and microwave power. In this context we did observe multiple 'phase reversals' as functions of temperature, and microwave power which we report here.

5.1.2 Experimental

YBCO powders were prepared by solid state route. Nanonickel powders were commercially obtained from Sigma-Aldrich company. For this study a nominal 2%wt of nanonickel powders were added into YBCO powders and thoroughly mixed using a mortar and pessel with several grinding cycles to obtain uniform distribution of nanonickel in the YBCO powder matrix. These nanonickel added YBCO powders which we name it Ni-YBCO from here onwards were then used for our NRMA studies. NRMA studies were carried out with Bruker ESR spectrometer with Oxford instruments low temperature facility.

For these experiments the microwave frequency was fixed at 9.3 GHz. DC magnetic fields were varied between -1500 to 1500 Oe back and forth. We studied NRMA in the Ni-YBCO powder system with varying temperature, microwave power and modulation field as shown in the data represented in figures discussed in results section. All experiments were conducted in zero field under cyrogenic conditions.

5.1.3 Results and Discussion

Figure 28, shows NRMA in the Ni-YBCO powders measured at various temperatures with 100 mW microwave power and 5 G modulation amplitudes. Inset shows the ESR signal in the normal state. ESR signal is a phase reference to the NRMA signals. For the resonant signal, absorption is always maximum at resonance field and decreases as the field is swept away from the resonance field. Therefore if the NRMA signal is in/out of phase with ESR signal, then accordingly has maximum/minimum of absorption at zero field.

Significantly one can notice multiple phase reversals at 20 K, 60 K and again at 70 K with a structure appearing at 40 K and 50 K. These observed features do sustain at different modulation amplitudes namely 7 G and 10 G. When microwave power was increased to 158.5 mW the phase reversal temperature shifted to 30 K from 20 K with structure remaining at 40 K and the multiple phase reversals that were observed at 60 K and 70 K did not appear at this power. All these features are shown in figure 29.

Further increasing of microwave power to 316 mW led to no phase reversal at any temperature but the structure remained as it was at 40 K.

For comparison we show the NRMA signals for the pure YBCO powders in Figure 30. Thus the experimental data shows that in the nanonickel added YBCO powders (Ni-YBCO) one can observe multiple phase reversals of NRMA signals, which we report for the first time and which depend on microwave power and temperature strongly. Such a phase reversal of NRMA in pure YBCO powders was reported earlier [10] and was interpreted as a cross over from hysteretic to non-hysteretic Josephson junctions. But

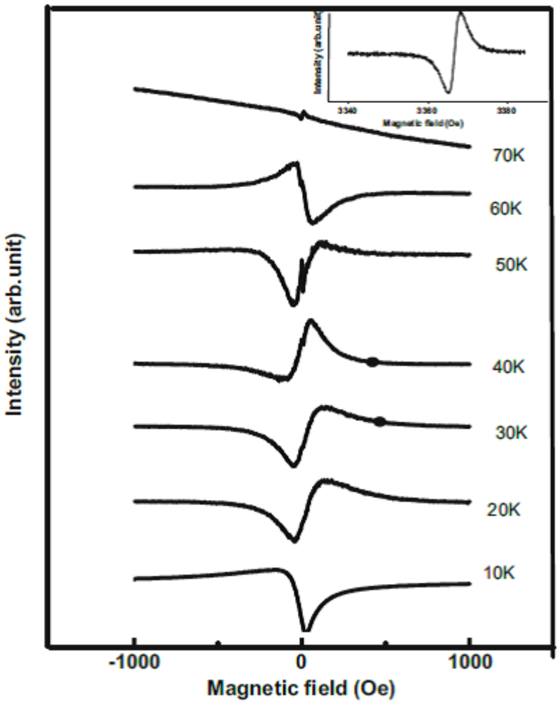

Figure 28: NRMA in the Ni-YBCO powder measured at various temperatures with 100 mW and 5 G modulation amplitude. One can notice multiple phase reversal at 20 K, 60 K, and 70 K. Inset shows the ESR signal in the normal state which enables to compare the phases of resonant signal with that of the NRMA signals.

that was a single phase reversal that occurs as a function of microwave power.

In the nanonickel added YBCO powder system the phase reversal occurs multiple times at different temperatures and that it is strongly dependent on microwave power. Nano nickel particles in between two YBCO particles acts as a ferromagnetic barrier and should lead to π-JJs. However , it must be noted that only 2 wt% nano nickel was added into the YBCO powder. Which means not all inter particle weaklinks would have a nano nickel particle in between two YBCO particles and therefore there would be several normal 0-JJs. Hence, the Ni-YBCO powder system was essentially a mixture of π-JJs and 0-JJs, which may effectively lead to 0-π-JJs due to clusters and loops formed by YBCO-Ni-YBCO-YBCO kind of interparticle connections as shown in the Figure 31. And as in such a case one will have group of junctions whose critical current have minimum at zero field and group of junctions which have maximum at zero field, which give mixed NRMA response

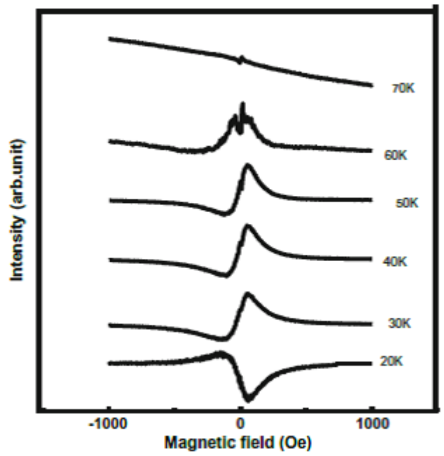

Figure 29: NRMA in the Ni-YBCO powder measured at various temperatures with 158.5 mW and 5G modulation amplitude. Shift of phase reversal temperature from 20 K to 30 K and disappearance of multiple phase reversals to be noted.

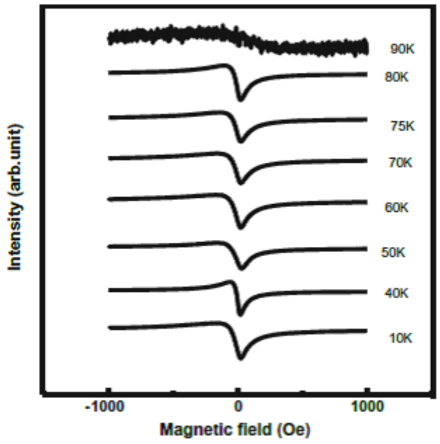

Figure 30: NRMA signals from YBCO powder without nano nickel addition, and absence of phase reversal to be noted. Also one can see that the T_c to be around 90 K as the NRMA signal becomes very weak.

that shall now strongly depend on temperature and microwave power. Thus there can be multiple phase reversals as functions of temperature and microwave power and structure in NRMA signals. As microwave power is increased, there can be shifts in temperature of phase reversals and also possibly as microwave power either can bring coherence among JJs in a group of junctions [9] and or it can break some of the weaker junctions leading to group of junctions with narrower spread in their coupling energy. This scenario thus can lead to the elimination of multiple phase reversal that occurred in low microwave power regime.

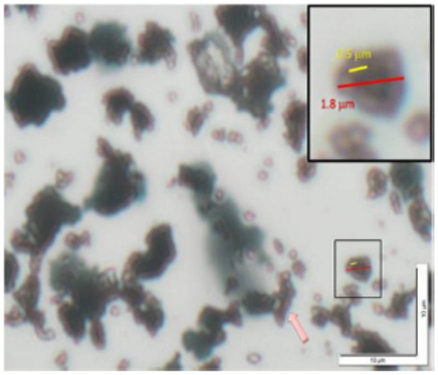

Figure 31: Optical micrograph of 2% Ni-YBCO powder. One can notice clusters of YBCO-Ni-YBCO-YBCO inter particle connected loops as shown by arrow in the picture. Inset shows typical YBCO particle size of the order of microns and the nickel particle agglomerates of submicron size.

Another interesting feature that observed was a very linear dependence of NRMA signal (which is a field derivative of absorption) just below Tc at 70 K, as shown in figure 28. In principle one can express NRMA signal intensity as I(H) $\sim [\delta P/\delta H]H_{mod}$ [14]. Here I(H) is the NRMA signal intensity which depends on the applied field H. $\delta P/\delta H$ is the derivative of microwave power absorption with respect to the applied field $H.H_{mod}$ is the modulation field amplitude.

The fact that the measured I(H) at 70 K in Figure 29, and explicitly shown in Figure 32, is linear except for a very narrow signal very close to zero field, indicates that the linear portion of the NRMA signal when integrated is parabolic or having H^2 dependence. Such a H^2 dependence of microwave power absorption can be due to pair breaking as pair breaking depends in H^2. Such pair breaking effects can dominate near T_c thermodynamically.

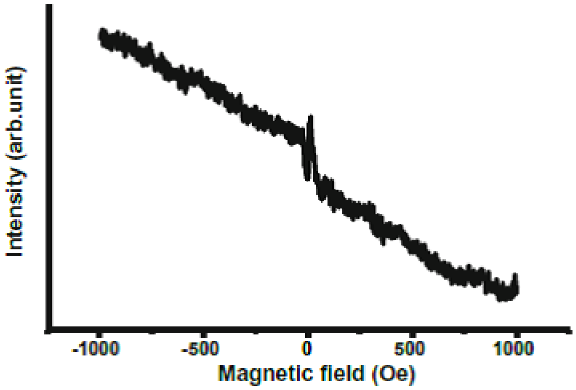

Figure 32: Zoomed NRMA in the Ni-YBCO powder measured at 70 K with 100 mW and 5 G modulation amplitude.

References

[1] S.V. Bhat, P. Ganguly, T.V. Ramakrishnan, C.N.R. Rao, *J. Phys.* C 20, L559 (1987).

[2] K.W. Blazey, K.A. Muller, J.G. Bednorz, W. Berlinger, G. Amoretti, E. Buluggiu, A. Vera, F.C. Matacotta, *Phys. Rev.* B 36, 7241 (1987).

[3] K. Kachaturyan, E.R. Weber, P. Tejedor, A.M. Stacy, A.M. Portis, *Phys. Rev.* B 36, 8309 (1987).

[4] C. Rettori, D. Davidov, I. Blelaish, I. Feluer, *Phys. Rev.* B 36, 4028 (1987).

[5] R. Durny, J. Hautala, S. Ducharme, B. Lee, O.G. Symko, P.C. Taylor, D.J. Zhang, J.A. Xu, *Phys. Rev.* B 36, 2361 (1987).

[6] J. Stankowski, P.K. Kahol, N.S. Dalal, J.S. Moodera, *Phys. Rev.* B 36, 7126 (1987).

[7] V.V. Srinivasu, B. Thomas, M.S. Hegde, S.V. Bhat, *J. Appl.Phys.* 75, 4131 (1994).

[8] S.V. Bhat, V.V. Srinivasu, N. Kumar, *Phys. Rev.* B 44, 10121 (1991).

[9] V.V. Srinivasu, K.I. Itoh, A. Hashizume, V. Sreedevi, H. Kohmoto, T. Endo, R. Ricardo da Silva, Y. Kopelevich, S. Moehlecke, T. Masui, K. Hayashi, *J. Supercond. Incorp. Nov. Magn.* 14, 41 (2001).

[10] V.V. Srinivasu, S.V. Bhat, N. Kumar, *Solid State Commun.* 89, 375 (1994).

[11] V.V. Srinivasu, R. Pinto, M.D. Sastry, *Appl. Supercond.* 4, 195 (1996).

[12] R.B. Onyancha, J. Shimoyama, S.J. Singh, H. Ogino, V.V. Srinivasu, *J. Supercond. Nov. Magn.* Vol 28, 10, 2927-2934 (2015).

[13] A. Rastogi, V.V. Srinivasu, M.S. Hegde, S.V. Bhat, *Phys.* C, Vol 234, issues 3-4, 229-231 (1994).

[14] I.I. Khairullin, P.K. Khabibullaev, V. Yu, A.A. Sokolov, T.R. Zakhidov, *J. of Phys.* 23 , 1107 1126 (1999).

[15] D. Shaltiel, H.A. Krug von Nidda, *Nanosci. and Nanotechnol. Lett*, Vol 3, 575-578(4) (2011).

[16] W. Braunisch, N. Knauf, V. Kataev, S. Neuhausen, A. Grtz, A. Kock, B. Roden, D. Khomskii and D. Wohlleben, *Phys. Rev. Lett* 68, 1908 (1992).

[17] A.M. Portis, K.W. Blazey, K.A. Muller and J.G. Bednorz, *Euro.Phys.* Lett 5, 467 (1988).

[18] A. Dulcic, B. Rakvin and M. Pozek *Euro. Phys. Lett* 10, 593 (1989).

[19] M. Weides, M. Kemmler, H. Kohlstedt, R. Waser, D. Koelle, R. Kleiner, *Phys. Rev. Lett* 97 (24), 247001 (2006).

6 CHAPTER SIX

6.1 Non-resonant Microwave Absorption Signals in Nanonickel added YBCO Superconducting powders: Distinctive Observation

6.1.1 Introduction

Ever since the discovery of the Non-resonant microwave/RF absorption (NRMA) in the high-T_c Superconductors (HTSC) [1] and followed by others [2-6], NRMA has evolved into a powerful spectroscopic tool to probe the superconductivity properties in HTSC, such as granularity, critical current density and fluxon viscosity coefficient, etc. [7-14]. NRMA spectra in anisotropic superconductors, such as Bi2212 and Bi2223 powders, single crystals and films, showed new and complex features [15-21] as compared to very simple lineshapes in $YBa_2Cu_3O_{7-x}$ [9]. For example, NRMA when measured in a configuration with the applied field perpendicular to the Bi2212 crystal ab-plane, shows a narrow low field peak followed by a broad shoulder like peak extending to high fields [16-18]. These new features in the NRMA lineshapes of the Bi2212 single crystals have assumed significance, as they are interpreted in terms of the intrinsic Josephson effect by Rastogi et al., [18], AC magnetic field shaking of Josephson vortices [18]. Two crucial experimental observations have to be noted from Ref. [18]. The second peak in the NRMA spectra of Bi2212 single crystal occurs only in a temperature window of 2-3 K, at the so-called 'magic temperature' near Tc, and it occurs only when the DC applied field is perpendicular to the crystal ab-plane [18]. The second peak is absent when the DC field is applied parallel to ab-plane. However, a more careful and systematic measurements by Srinivasu et al., [19] showed that: (1) there is an evolution of the second peak with microwave power and (2) the second peak occurs even in the field configuration where the applied DC field is parallel to the crystal ab-plane but with the microwave magnetic field perpendicular to the ab-plane, at appropriate microwave powers. Which means the second peak in the NRMA spectra of Bi2212 single crystal depends on the mutual orientation of the applied DC field, microwave magnetic field and the crystal ab-plane, and actually evolves as a function of microwave power. Thus one can see that the second peak in NRMA spectra of Bi-2212 crystals has great significance and may be talking new physics.

Hence, the hysteresis in NRMA signal is very useful to study vortex dynamics pinning as well as for understanding NRMA mechanisms [17,20]. In this thesis we report on the NRMA high quality Ni-YBCO powder and we confirm an existence of a structure (broad and narrow peaks). We noted that narrow peak persists up to the temperature of 75 K which is close to superconductivity transaction temperature of 90 K [22]. The absence of cross over from normal to anoumalous absorptions in these materials depicts presence of hysteretic type of Josephson junction within the microwave power employed. This disappear to the microwave power variation studies reported on Ni-YBCO where a phase reversal at 158 mW was observed and discussed on the basic of Josephson junction changing from hysterestic nature.

6.1.2 Experiment

Sample preparation procedure were reported somewhere [22]. For this study a nominal of 3%wt of nano nickel powders were added into YBCO powders and thoroughly mixed using a mortar and pressed with several grinding cycles to obtain uniform distribution of nano nickel in the YBCO powder matrix. These nano nickel added YBCO powders which we designation Ni-YBCO from here onwards are then used for our NRMA studies. NRMA studies were carried out with Bruker ESR spectrometer with Oxford instruments low temperature facility. For these experiments the microwave frequency was fixed at 9.3 GHz. DC fields were varied between -1500 to 1500 Oe back and forth. We studied NRMA in the Ni-YBCO powder system with varying temperature, microwave power and modulation field. All experiments were conducted in zero field cryogenic condition.

6.1.3 Results and Discusion

In characterizing the sample, we have used XRD, SEM and FTIR which review the sample size. The XRD patterns revealed that the main phase was YBCO with peaks of Ni marked, in Figure 33. Revealed that the orthorhombic structure of YBCO was preserved even with the existence of nickel nanoparticles.

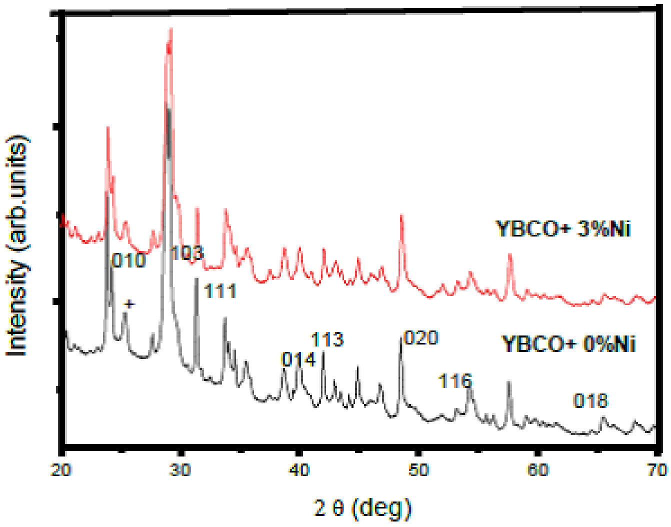

Figure 33: Powder X-ray diffraction of YBCO and Ni-YBCO sample.

A micrograph of the Ni-YBCO powder as synthesized is shown in Figure 34. Voids can be seen which separate grain conglomerates. Additions of 3 wt% of nickel nanoparticles which is located at the grain boundaries are repairing the grain structure by connecting each grain together.

Nanonickel particle in between two YBCO particles act as a ferromagnetic barrier and lead to π JJs [22]. This Ni-YBCO powder system is a mixture of π JJs and 0 JJs, which may effectively lead to 0-π JJs due to clusters and loops formed by YBCO-Ni-YBCO-YBCO kind of inter-particle connections as reported by Nemangwele et. al., [22]. As microwave power is increased, there can be a shift in temperature of phase reversal and also possibly microwave power either can bring coherence among JJs in a group of junctions [17] or it can break some of the weaker junctions, leading to a group of junctions with narrower spread in their coupling energy. Thus this can lead to the elimination of

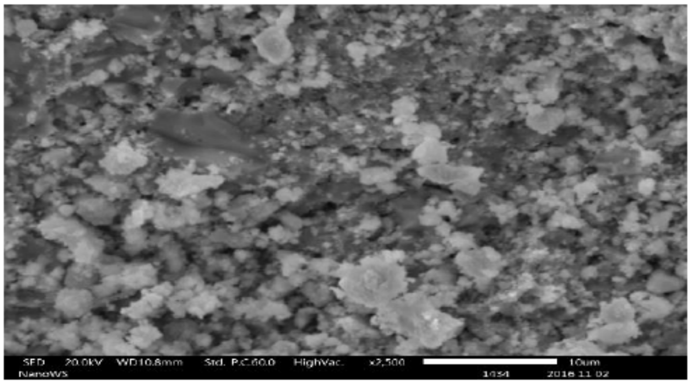

Figure 34: SEM image of Ni-YBCO at high magnification.

multiple face reversals that occurred in low microwave power regime. The defects and grain boundaries at Ni-YBCO reveal that the material is highly granular. These weaklink usually result in the formation of current blocking paths, which render global current density orders of magnitude smaller than local current density [1].

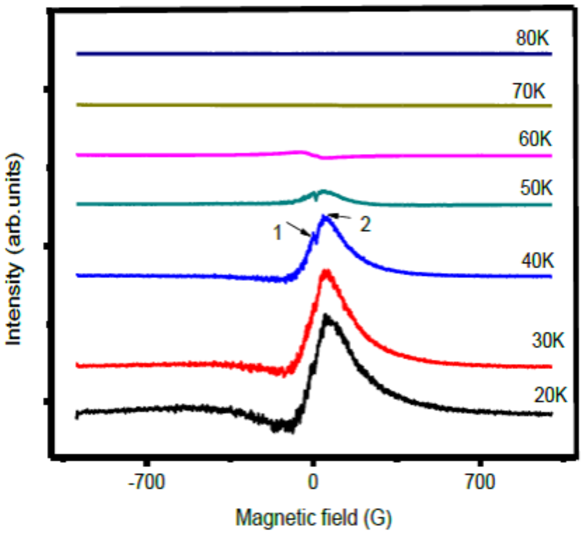

Figure 35: Non-resonant microwave absorption derivetive of Ni-YBCO recorded at different temperatures with microwave power of 158.5 mW.

Measurements were carried out with temperature variation (from 4.2 K to T$_c$, modulation field and microwave power variation. Figure 35, shows NRMA derivative signal evolving as a function of temperature with all measurements recorded at microwave power of 158.5 mW and field modulation of 5 G. Hence, signal intensity decreases with increase in temperature up to 75 k and vanishes at 80 K. It may also be observed that the line shapes are seen to be quite different in this case. The presence of two peaks in the system is very interesting as it shows that these peaks (1 and 2 in Figure 35) constitute a common feature of YBCO material. Figure 36, show the NMRA hysteresis for Ni-YBCO recorded at different temperatures with microwave power of 158.5 mW.

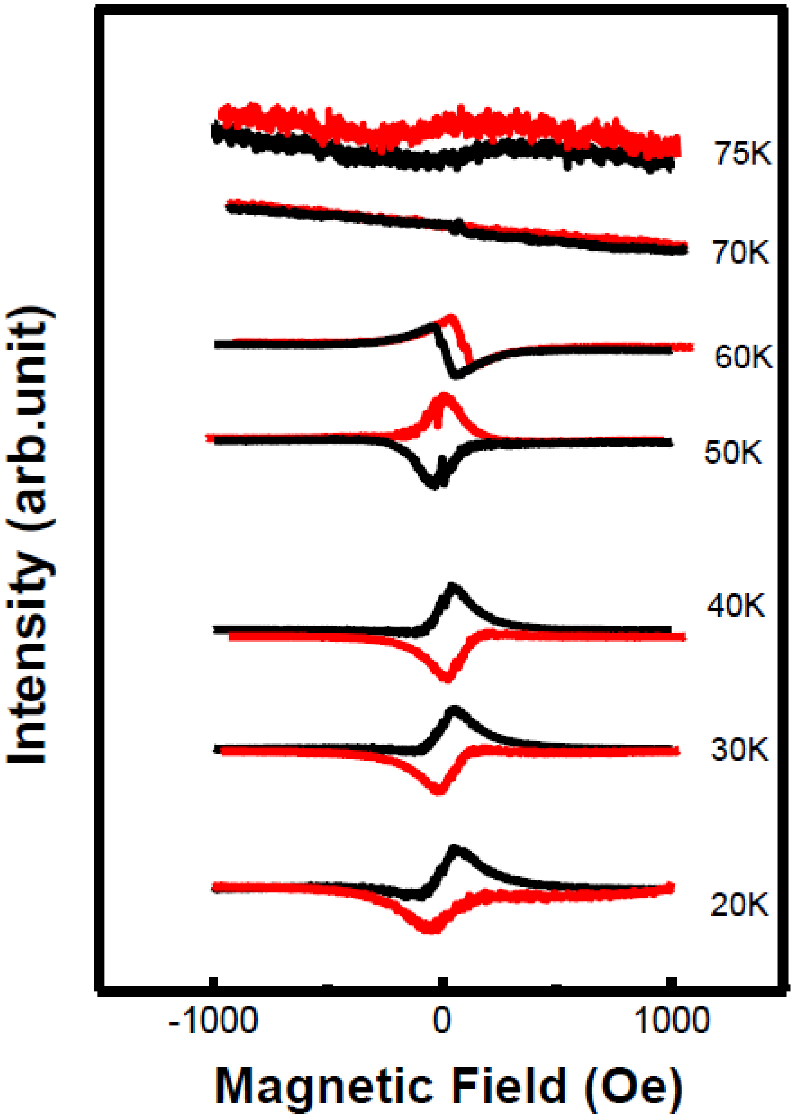

Figure 36: NMRA hysteresis Ni-YBCO recorded at different temperatures with microwave power of 158.5 mW.

The results emphasize that the high permeability ferromagnet acts as a magnetic short-circuit for magnetic flux density, since it creates a low reluctance path [23]. When the assembly is subjected to an external magnetic field, the penetration of the magnetic flux inside the superconductor is delayed in the vicinity of the ferromagnet. The region above the ferromagnet in the trapped field configuration is shielded from the flux trapped inside the superconductor. Moreover, the flux lines that were closed through the superconductor are now closed through the ferromagnet, which leads to a decrease in the bend of the return flux lines inside the superconductor [24]. In addition, the flux lines are perpendicular to the median plane of the superconductor in the absence of the ferromagnet whereas they are perpendicular to the ferromagnet /superconductor interface in the presence of the ferromagnet. Therefore, adding the ferromagnet can be assimilated to doubling the height of the superconductor as expected in the limiting case of a semi-infinite ferromagnet of infinite permeability where the effect of the ferromagnet can be replaced by an image of the superconductor [25].The doubled height corresponds to an increase of the effective aspect ratio of the sample and a reduction of the edge effect of a finite length sample. To explain the NRMA signal intensity evolution with temperature further, we consider the method proposed by Bhat et al., [1]. As evidence, the granularity of a ceramic sample denotes that superconducting grains are weakly connected. Therefore, as the temperature is lowered from T$_c$ many superconducting grains became coupled, resulting in an increase in the shielding Meissner effect. This happens as a consequence of increasing superconducting domains within the grains and strong coupling in the intergranular Josephson junction. Bhat et al., [1] assume that at a given temperature (T) and applied magnetic field (H), a volume fraction x of the sample is superconducting. Equation (6.1) gives RF voltage (signal) as the volume fraction x is changed with respect to T and H.

$$V/V_0 = \alpha(1-3x) + 1/\alpha(1-3x)/(1-3/2x)^2 \tag{6.1}$$

where $V_0 = I_0/K^2\omega C_P$, $\alpha = 4\pi a^2\omega\mu_0\sigma N, \sigma$ is conductivity, a is sample dimensions, ω is frequency, μ_0 is permeability and C_p is capacitance. We noted from Figure 36, that the NRMA signal intensity decreases with an increase in temperature. Following this model, we can argue that as temperature is increased from 20 K, the critical current is reduced gradually and fluxons penetrate the sample. This results in decoupling of superconducting grains and the superconducting fraction x is reduced. Hence, there will be reduction in signal intensity V/V_0 as temperature is increased. Following Bhat et. al., [26] a transition from normal to anomalous absorption happens as the structure and line shape evolved as a function of temperature. However, the transition does not occur in our work as a function of temperature. This could be because of the possibility of π junctions in the sample. The presence of π junction may as well invigorate thoughts that the peak 1 observed in our study is a result of the Wohlleben effect [21]. Hence the Wohlleben effect has the characteristics which include intragrain π contacts and an anomalous microwave absorption corresponding to a maximum at H=0 and it occurs at temperature below T$_c$. Srinivasu at el., [27] argued that the peak appears as a result of induced phase coherence by microwave power and this coherence is later destroyed by the applied magnetic field. This possibility cannot explain our finding as the measurements were done with varying temperature and the peak registered below T$_c$.

References

[1] S.V. Bhat, P. Ganguly, T.V. Ramakrishnan, C.N.R. Rao,*J. Phys.* C 20, L559 (1987).

[2] K.W. Blazey, K.A. Muller, J.G. Bednorz, W. Berlinger, G. Amoretti, E. Buluggiu, A. Vera, F.C Matacotta, *Phys. Rev.* B 36, 7241 (1987).

[3] K. Kachaturyan, E.R. Weber, P. Tejedor, A.M. Stacy, A.M. Portis, *Phys. Rev.* B 36, 8309 (1987).

[4] C. Rettori, D. Davidov, I. Blelaish, I. Feluer, *Phys. Rev.* B 36, 4028 (1987).

[5] R. Durny, J. Hautala, S. Ducharme, B. Lee, O.G. Symko, P.C. Taylor, D.J. Zhang, J.A. , Xu, *Phys. Rev.* B 36, 2361 (1987).

[6] J. Stankowski, P.K. Kahol, N.S. Dalal, J.S. Moodera, *Phys. Rev.* B 36, 7126 (1987).

[7] S.V. Bhat, V.V. Srinivasu, N. Kumar,*Phys. Rev.* B 44, 10121 (1991).

[8] V.V. Srinivasu, S.V. Bhat, N. Kumar, *Solid State Commun.* 89, 375 (1994).

[9] V.V. Srinivasu, B. Thomas, M.S. Hegde, S.V. Bhat, *J. Appl. Phys.* 75, 4131 (1994).

[10] V.V. Srinivasu, V. Sreedevi, A. Hashizume, H. Kohmoto, S. Moehlecke, R. Ricardo da Silva, Y. Kopelevich, T. Endo, *Physica.* C 362, 285 (2001).

[11] V.V. Srinivasu, R. Pinto, M.D. Sastry, *Appl. Supercond.* 4, 195 (1996).

[12] V.V. Srinivasu, B. Thomas, N.Y. Vasanthacharya, M.S. Hegde, S.V. Bhat, *Solid State Commun.* 79, 713 (1991).

[13] V. Likodimos & M. Pissas, *Phys. Rev.* B 65, 172507 (2002).

[14] A. Rouco, X. Obradors, J. Britico, M. Tovar, S. Piol, J. Fontcuberta, M.T. Causa, *Physica.* C 2027, 235240 (1994).

[15] J.T. Masiakowski, M. Puri, L. Kevan, *J. Phys. Chem.* 95, 1393 (1991). T. Shaposhnikova, Y.U. Talanov, Y.U. Vashakidze, *Physica.* C 385, 383 (2003).

[16] T. Shaposhnikova, Y.U. Talanov, S. Tsarevskii, *Physica.* C 451, 90 (2007). A. Rastogi, Y.S. Sudershan, S.V. Bhat, A. K. Grover, Y. Yamaguchi, K. Oka, Y. Nishihara, *Phys. Rev.* B 53, 9366 (1996).

[17] V.V. Srinivasu, K.I. Itoh, A. Hashizume, V. Sreedevi, H. Kohmoto, T. Endo, R. Ricardo da Silva, Y. Kopelevich, S. Moehlecke, T. Masui, K. Hayashi, *J. Supercond. Incorp. Nov. Magn.* 14, 41 (2001).

[18] A. Rastogi, V.V. Srinivasu, M.S. Hegde, S.V. Bhat, *Phys.* C, Vol 234, issues 3-4, 229-231 (1994).

[19] O. K. C. Tsui, N. P. Ong, and J. B. Peterson, *Phys. Rev.* Lett 76, 819 (1996).

[20] Y. Matsuda, M. B. Gaifullin, K. Kumagai, M. Kosugi, and K. Hirata, *Phys. Rev.* Lett 78, 1972 (1997).

[21] R.B. Onyancha, J. Shimoyama, S.J. Singh, H. Ogino, and V.V. Srinivasu, *J. Supercond Nov Magn.* Vol 28, 10, 2927-2934 (2015).

[22] F. Nemangwele, V. Sankaran, B.K. Roal, J.Das, and V.V. Srinivasu, *J. Supercond. Nov Magn.* vol. 29, 11, 1557-1939 (2016).

[23] N. Del-Valle, S. Agramunt-Puig, C. Navau, A. Sanchez, *J. Appl. Phys.* 111, 013921 (2012).

[24] Y. Mawatari, *Phys. Rev.* B 77, 104505 (2008).

[25] A. Sanchez, N. Del-Valle, C. Navau, D.-X. Chen, *Appl. Phys.* Lett 97, 072504 (2010).

[26] S.V Bhat, V.V Srinivasu, N. Kumar, *Phys. Rev.* B 44, 10121 (1991).

[27] V.V. Srinivasu, *J Supercond. Nov. Magn.* 23, 305-308 (2010).

7 CHAPTER SEVEN

7.1 Magnetic Proximity Effect in Ni-YBCO Superconductor

7.1.1 Introduction

While ferromagnetism is associated with the parallel alignment of the electronic spins in a system, the Cooper-pairs forming the condensate of conventional superconductors consist of electrons with opposite spins. These opposing ordering schemes of the electronic spins make of superconductivity and ferromagnetism two antagonistic phenomena and give rise to the question about their interaction when located in close proximity. The interplay of the competing superconducting and ferromagnetic order parameters is thus a fascinating topic that has been extensively premeditated theoretically and experimentally [1-3].

In recent years significant progress has been made with thin-film hetero-structures from conventional superconductors and elemental or alloy ferromagnets where effects such as domain wall superconductivity [4], critical temperature oscillations with the thickness of the ferromagnetic layer in superconductor/ferromagnet/superconductor junctions [5] and a long-range proximity effect of a spin-triplet superconducting state through composite ferromagnetic layers with a non-collinear magnetic order [6], were predicted theoretically and confirmed experimentally [7-11]. These developments have inspired concepts for new kinds of spintronic devices and applications in information technology [12, 13].

The discovery of the cuprate high-temperature superconductors by Bednorz and Muller in 1986 marked a breaking point in the history of superconductivity [14]. With critical temperatures as high as 130 K [15], the scientific community was challenged not only to explain the mechanism of superconductivity in these recognised family of superconductors but also to clear the way to new devices and applications. Incorporation of magnetic or nonmagnetic metals such as Mg^{2+},Mn^{2+}, Ni^{2+} , La^{3+} , Nd^{3+} etc. give rise to migration of cations between the aforementioned lattice sites and directly influences the physical properties of the product [10,12], consequently, a material with tailored property suitable for various applications is produced. It has been reported that doping nickel into YBCO superconductor greatly enhanced the material's electromagnetic properties [13]. Study have shown that alloys of Co-Ni-Fe are magnetostrictive and are widely applied as magnetoresistance sensors as well as thin film head for high density magnetic recording [14]. Manganese (Mn) substitution on the other hand has also been studied [15,16].

Recent improvements in film deposition techniques, enable the layer by layer controlled epitaxial growth of multilayers and superlattices with very sharp interfaces [22, 29]. Experiments on this kind of oxide superconductor/ ferromagnet heterostructures revealed effects such as a change in the superconducting critical temperature, T_c, related to the presence and thickness of the ferromagnetic layers, and vice-versa [17, 23], a superconductivity-related giant magneto-resistance in ferromagnet/ superconductor/ferromagnet trilayers [25], the enhancement of T_c by an external magnetic field [26, 27] and even a superconductivity-induced modulation of the magnetic moment in the ferromagnetic layers [28]. These observations provided encouraging evidence for a substantial interaction between the superconducting and ferromagnetic order parameters in these cuprate/manganite multilayer systems. They also showed that not only is the superconducting but also the magnetic properties of these oxide heterostructures are extremely versatile and need to be thoroughly investigated.

On the other hand, the observation of the multiple face reversal in Ni-YBCO [24] revived the interest on the versatile magnetic properties of these systems. Given the similar type of material Ni-YBCO superconductors and their potential for high-temperature applications, the study of the interaction between the superconducting and ferromagnetic order parameters was soon extended to these systems.

7.1.2 Experimental

The experimetal procedure has been reported elsewhere [24]. For this study a nominal of 0,5 1,2 2, and 3 %wt of nano nickel powders were added into YBCO powders and thoroughly mixed using a mortar and pressed with several grinding cycles to obtain uniform distribution of nano nickel in the YBCO powder matrix. The particle size was determined and reported elsewhere [24] and granularity revealed from SEM micrographs. The crystalline structure of resultant nano particles was determined with the help of X-ray diffraction measurements(XRD) using Rigaku D/Max-IIIC with Cu-K radiation in the $2\theta range of 20-70^o$. FTIR spectra in the range 4000-200 cm^{-1} were recorded in order to investigate the nature of the chemical bonds formed (see Figure 38). The surface morphology of the composites was analysed with JEOL, JSM7001F Scanning Electron Microscopy (SEM). Magnetic measurements were performed by using a vibrating sample magnetometer (VSM) of LDJ Electronics Inc., Model 96000. The sample was measured between 715 kOe at room temperature (25 ^{o}C).

7.1.3 Results and Discussion

In characterizing the sample, we have use XRD, SEM and TEM which reveal the sample size. The X-ray diffraction powdered patterns for Ni-YBCO (0.5, 1.2, 2, and 3 %wt) are presented in Figure 37, with peaks of Ni marked.

A micrograph of the Ni-YBCO powder as synthesized is shown in Figure 40. Voids can be seen which separate grain conglomerates. This image of high magnification revealing stripe-like grains with clear grain boundaries. It is important to note that these defects and grain boundaries reveal that the material is highly granular. These weaklinks result in the formation of current blocking paths hence rendering global current density orders of magnitude smaller than local current density. The detection limit and largest error of determination for the elements present were 0.2 and 29.5 % respectively as from Figure 39. The scan area micro-analysis was 2.0 $\times$2.0 $\times$ 10μ m.

In Figure 41, we show the magnetization and hysteresis loops for high field and low field sweeps at 50 K which is well below Tc. Figure 42, shows the enlargement of Figure 41, at the region around the origin where the weaklinks are supposed to be very strong. In such a situation, the nano nickel in the weaklinks acts as flux pinning agent. As expected for very low doping or low nano nickel addition ($\sim$ 0.5 and 1.2 wt%) we do not see much effect. However, when the nano nickel addition is increased to 2% and 3% we see a significant change in the magnetization and the associated hysteresis, indicating flux pinning.

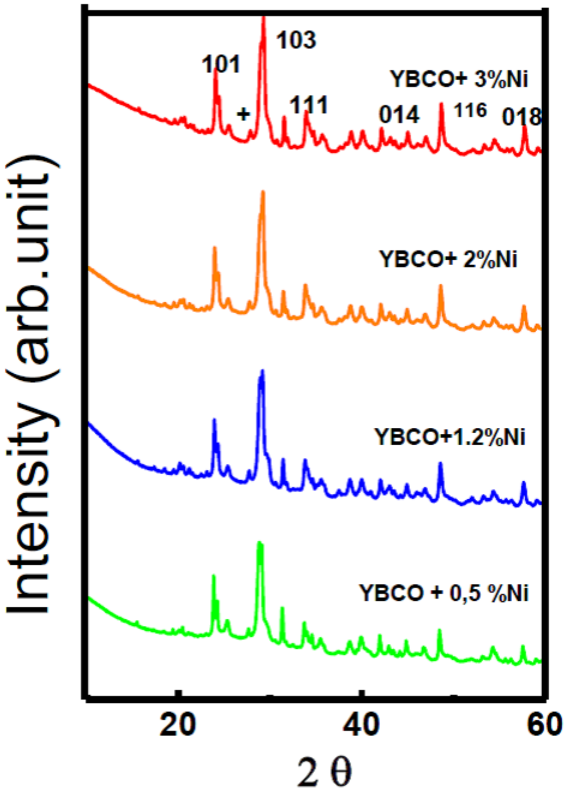

Figure 37: The X-ray diffraction powdered patterns for Ni-YBCO (0.5, 1.2, 2, and 3 %wt).

As we focused on the microwave absorption in the low field, we have actually performed magnetization hysteresis loop measurements in the field scan range of -100 to +100 Oe and we see a strong effect of nano nickel wt%. The hysteresis loop size in this field sweep range is very small or negligible, for 0.5 wt% nano nickel addition but as the wt% increases to 3%, we observed large hysteresis in this low field scan range. Thus our measurements of magnetization also supports our original idea of nano nickel acting as flux pinning agent in the weaklinks and the fact that it has great influence on the microwave absorption at low fields.

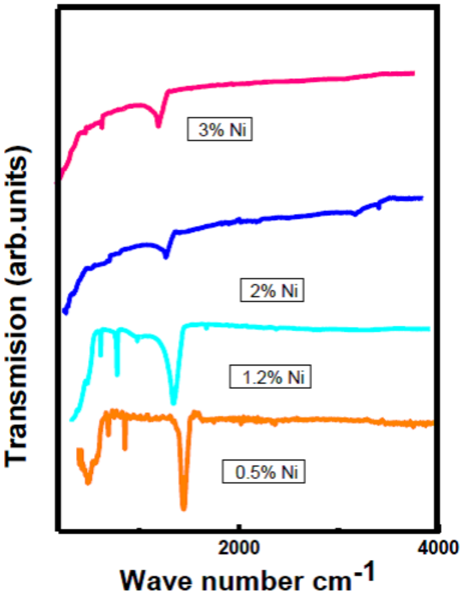

Figure 38: FTIR spectra in the range 4000-200 cm^{-1} to facilitate the investigation of the nature of the chemical bonds.

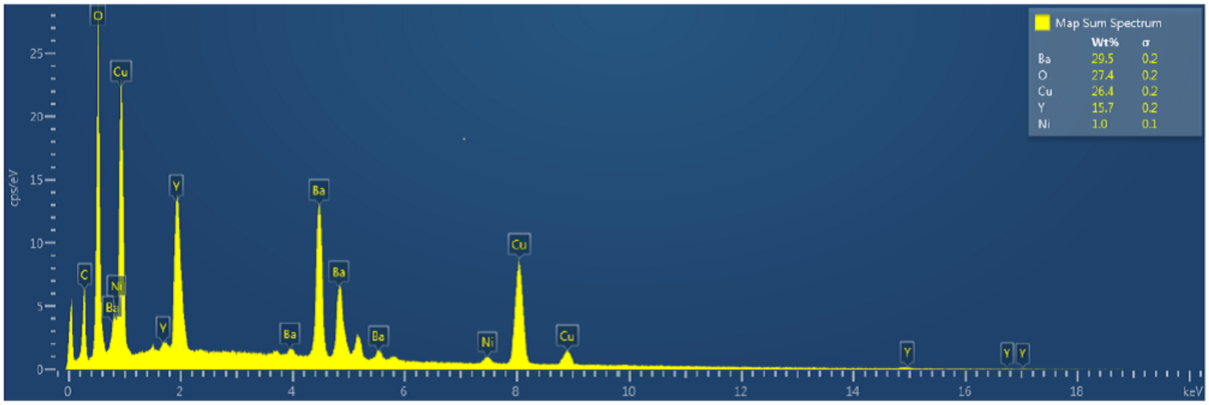

Figure 39: EDX spectra and elemental maps of Ni-YBCO.

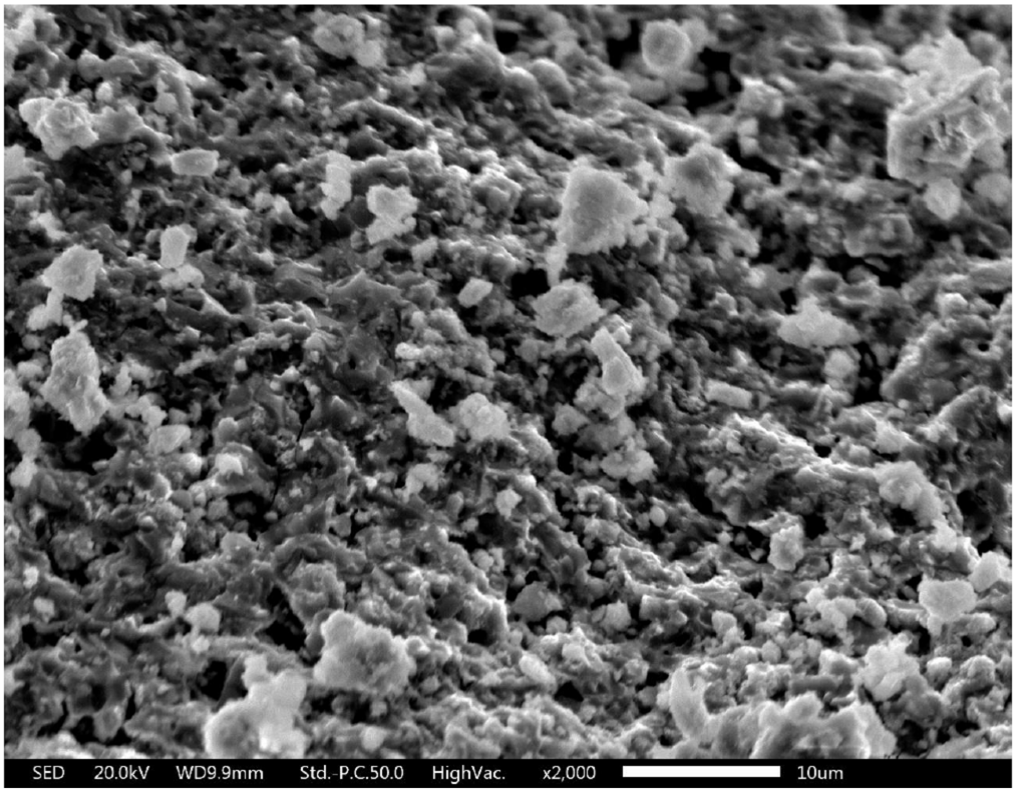

Figure 40: The SEM micrographs of Ni-YBCO.

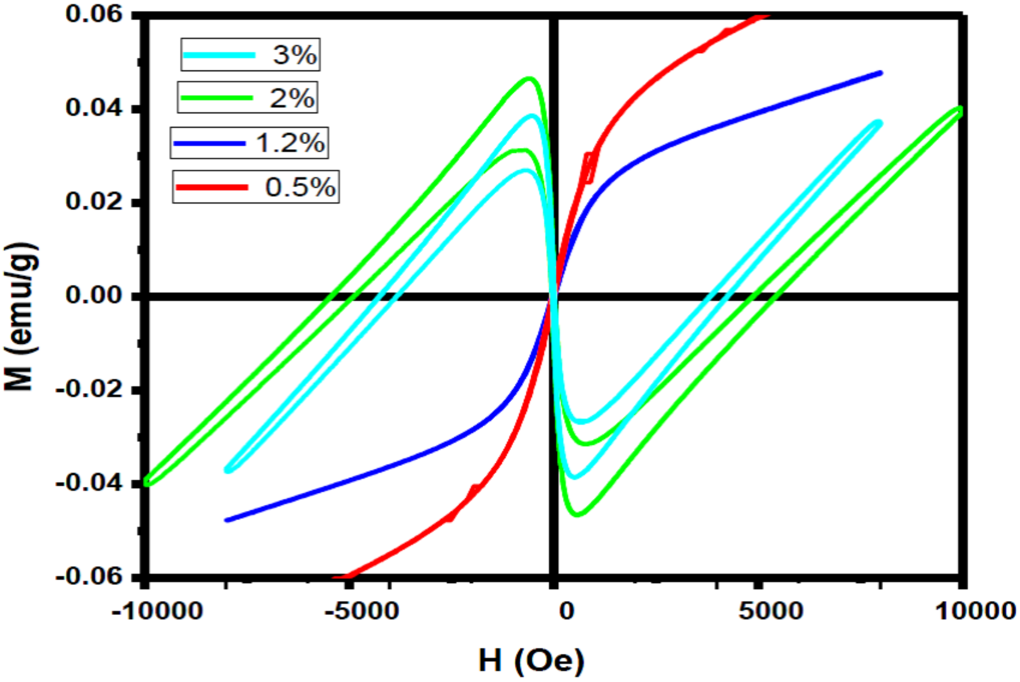

Figure 41: Magnetic hysteresis loops of the Ni-YBCO at 50 K.

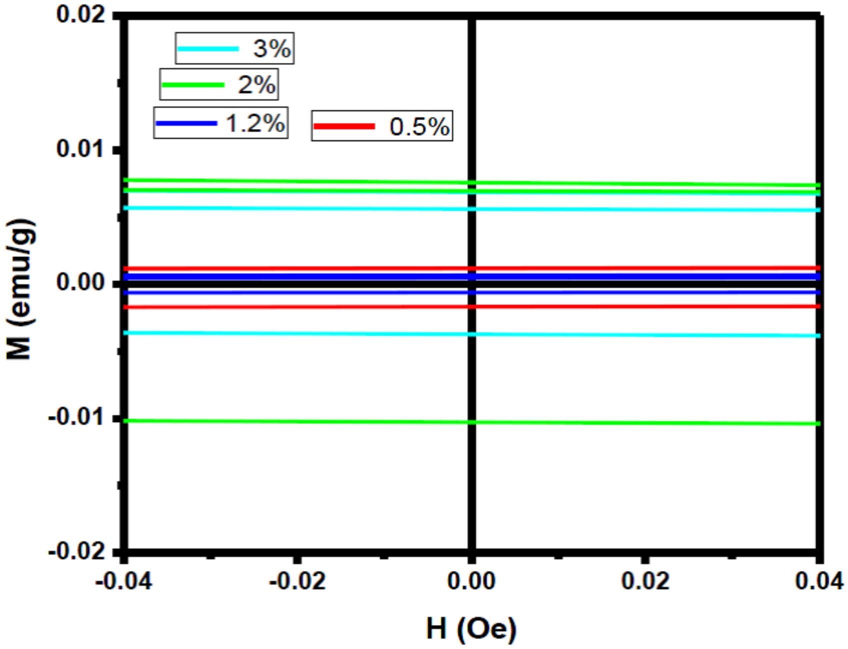

Figure 42: Magnetic hysteresis loops of the Ni-YBCO at 50 K enlarged region around the origin.

References

[1] L. Bulaevskii, A. Buzdin, M. Kuli and S. Panjukov. *Adv. Phys*. 34, 175 (1985).

[2] A. I. Buzdin, *Rev. Mod. Phys*. 77, 935 (2005).

[3] F. S. Bergeret, A. F. Volkov and K. B. Efetov, *Rev. Mod. Phys*. 77, 1321 (2005).

[4] A. I. Buzdin and A. S. Melnikov, *Phys. Rev*. B 67, 020503 (2003).

[5] J. Kehrle, V. Zdravkov, G. Obermeier, J. Garcia-Garcia, A. Ullrich, C. Muller,R. Morari, A. Sidorenko, S. Horn, L. Tagirov and R. Tidecks. *Ann. Phys*. 524, 37 (2012).

[6] A. F. Volkov, F. S. Bergeret and K. B. Efetov, *Phys. Rev*. Lett 90, 117006 (2003).

[7] T. Kontos, M. Aprili, J. Lesueur, F. Genet, B. Stephanidis and R. Boursier, *Phys. Rev*. Lett 89, 137007 (2002).

[8] Y. Blum, A. Tsukernik, M. Karpovski and A. Palevski, *Phys. Rev*. Lett 89, 187004 (2002).

[9] T. S. Khaire, M. A. Khasawneh, W. P. Pratt and N. O. Birge, *Phys. Rev*. Lett 104, 137002 (2010).

[10] J. W. A. Robinson, J. D. S. Witt and M. G. Blamire, *Science*. 329, 59 (2010).

[11] Z. Yang, M. Lange, A. Volodin, R. Szymczak and V. V. Moshchalkov, *Nat. Mater*. 3, 793 (2004).

[12] M. Eschrig, *Phys. Today*. 64, 43 (2011).

[13] N. G. Pugach and A. I. Buzdin, *Appl. Phys*. Lett 101, 242602 (2012).

[14] J. G. Bednorz and K. A. Muller, *Phys. B: Condens*. Matt 64, 189 (1986).

[15] A. Schilling, M. Cantoni, J. D. Guo and H. R. Ott, *Nature*. 363, 56 (1993).

[16] Y. Tokura and Y. Tomioka, *J. Magn*. Matt 200, 1 (1999).

[17] E. Dagotto, T. Hotta and A. Moreo, *Phys*. Rep 344, 1 (2001).

[18] P. Przyslupski, S. Kolesnik, E. Dynowska, T. Skoskiewicz and M. Sawicki, *IEEE T.Appl. Supercon.* 7, 2192 (1997).

[19] A. Goldman, P. Kraus, K. Nikolaev, V. Vasko, A. Bhattacharya and W. Cooley, *J. Supercond.* 14, 283 (2001).

[20] H.U. Habermeier, G. Cristiani, R. Kremer, O. Lebedev and G. van Tendeloo, *Physica.* C 298, 364-365 (2001).

[21] Z. Sefrioui, D. Arias, V. Pena, J. E. Villegas, M. Varela, P. Prieto, C. Leon, J. L. Martinez and J. Santamaria, *Phys. Rev.* B 67, 214511 (2003).

[22] T. Holden, H.-U. Habermeier, G. Cristiani, A. Golnik, A. Boris, A. Pimenov, J. Humlcek, O. I. Lebedev, G. Van Tendeloo, B. Keimer and C. Bernhard, *Phys. Rev.* B 69, 064505 (2004).

[23] R. Werner, C. Raisch, A. Ruosi, B. A. Davidson, P. Nagel, M. Merz, S. Schuppler, M. Glaser, J. Fujii, T. Chasse, R. Kleiner and D. Koelle, *Phys. Rev.* B 82, 224509 (2010).

[24] F. Nemangwele, V. Sankaran, B.K. Roal, J.Das, and V.V. Srinivasu, *J. Supercond. Nov. Magn.* vol 29, 11, 1557-1939 (2016).

[25] V. K. Malik, I. Marozau, S. Das, B. Doggett, D. K. Satapathy, M. A. Uribe-Laverde, N. Biskup, M. Varela, C. W. Schneider, C. Marcelot, J. Stahn and C. Bernhard, *Phys.Rev.* B 85, 054514 (2012).

[26] V. Pena, Z. Sefrioui, D. Arias, C. Leon, J. Santamaria, J. L.Martinez, S. G. E. te Velthuis and A. Hoffmann, *Phys. Rev.* Lett. 94, 057002 (2005).

[27] N. M. Nemes, M. Garca Hernandez, S. G. E. te Velthuis, A. Hoffmann, C. Visani, J. Garcia-Barriocanal, V. Pena, D. Arias, Z. Sefrioui, C. Leon and J. Santamar, *Phys. Rev.* B 78, 094515 (2008).

[28] K. Dybko, K. Werner-Malento, M. Sawicki and P. Przyslupski, *Euro. Phys.* Lett 85, 57010 (2009).

[29] J. Hoppler, J. Stahn, C. Niedermayer, V. K. Malik, H. Bouyanfif, A. J. Drew, M. Rossle, A. Buzdin, G. Cristiani, H.U. Habermeier, B. Keimer and C. Bernhard, *Nat. Mater.* 8, 315 (2009).

8 CHAPTER EIGHT

8.1 Conclusion

This section contains a brief summary of the results obtained in this thesis and of the outlook of these results. The results and outlooks have already been discussed thoroughly in the section from chapter 1 upto chapter 7, and this chapter is only intended as a summing up. In addition to the above a new subject is discussed in the outlook, since it has not been treated earlier.The magnetic properties of YBCO and Ni nanoparticles have been thoroughly investigated by means of a variety of complementary experimental techniques. The use of different techniques allows verification and validation of the results of the individual techniques.

In conclusion, we have intentionally added nano nickel particles with a nominal of 0.5, 1.2, 2 and 3 % wt into YBCO powders. With this dilute mixture of nano nickel particles, one should have groups of normal 0-JJ s and π -JJ s due to YBCO-nickel-YBCO interparticle weaklinks as nickel is ferromagnetic. These mixtures can thus lead to 0-π -JJ s and which turn results into multiple phase reversals in the NRMA spectra which was experimentally observed for the first time in our laboratory. We also showed that these multiple phase reversals then depend on microwave power and temperature. We argued that microwave power induced coherence among some groups of JJ s and breaking of some of the weaker JJ s can then lead to the disappearance of multiple phase reversals at higher microwave power levels. Further we also reported role of pair breaking effects that should give a linear field dependence of the derivative microwave absorption signal, which is the NRMA signal. This pair breaking effect dominates at temperature close to Tc which is expected thermodynamically

The presence of two peaks (peak 1 and 2) in the micro size construction type junction of Ni-YBCO sample, results in high permeability ferromagnet which acts as a magnetic short circuit for magnetic flux density and creates low reluctance path. A transition from normal to anomalous does not occur in our work, because of the possibility of π junction in the sample.

On the microwave absorption in the low field, we have actually performed magnetization hysteresis loop measurements in the field scan range of -100 to +100 and we see a strong effect of nano nickel % wt. The hysteresis loop size in this field sweep range is very small or negligible, for 0.5 % wt nano nickel addition but as the % wt increases to 3%, we observed large hysteresis in this low field scan range. Thus our measurements of magnetization also supports our original idea of nano nickel acting as flux pinning agent in the weaklinks and the fact that it has great influence on the microwave absorption at low fields.